Estimation of Water Transparency from Remote Sensing Data Based on A New Underwater Visibility Theory

January 2020

Jiang Dalin

Estimation of Water Transparency from Remote Sensing Data Based on A New Underwater Visibility Theory

A Dissertation Submitted to

the Graduate School of Life and Environmental Sciences,

the University of Tsukuba

in Partial Fulfillment of the Requirements

for the Degree of Doctor of Philosophy

(Doctoral Program in Integrative Environment and Biomass Sciences)

Jiang Dalin

Abstract

The water transparency, is a direct record of water optics and an important indicator of water quality. It is measured by the Secchi disk depth(Z_{SD}) and has been a routine measurement in field survey of aquatic environments since the 1860s. Over a century later, the remote sensing technique has also been widely used for retrieving the Z_{SD} values because of the technique's large area coverage and rapid data acquisition.

Lee et al. (2015) proposed a new theory for underwater visibility. Based on this new theory, Lee et al. (2015) also developed a semi-analytical algorithm for retrieving the Z_{SD} from remote sensing data (termed as Lee15 hereafter). Generally, there are three requirements for accurately estimating Z_{SD} when the Lee15 algorithm is used: (1) accurate measurements of remote sensing reflectance (R_{rs}); (2) accurate estimations of diffuse attenuation coefficient of downwelling irradiance (K_d); and (3) the proper values of K_T/K_d ratios (K_T is the diffuse attenuation coefficient of upwelling radiance).

However, challenges are still remained for each requirement. They are: (1)the widely used above-water approach for measuring R_{rs} suffers from the residual reflected skylight (Δ) effect, which will influence the accuracy of *in situ* R_{rs}; (2) the sixth version of quasi-analytical algorithm (QAA_v6) used for estimating absorption and backscattering coefficients (a and b_b) often failed in turbid inland waters, and thus reduced the estimation accuracy of K_d; and (3) the K_T/K_d ratio has been reported to be varied in a wide range. Therefore, the errors in R_{rs}, K_d and K_T/K_d ratios will be

finally propagated to the estimations of the Z_{SD}.

To address the above challenges, first, I proposed a new simple method, which only required the *in situ* R_{rs} spectrum itself as input, to further remove the Δ effects in the *in situ* R_{rs} measurements. The performance of the proposed method was evaluated using both simulation data and *in situ* R_{rs} spectra measured using a radiance sensor with a black tube (Δ-free *in situ* R_{rs}). The results showed that the proposed method outperformed other existing methods and can be applied to various types of waters. In addition, the proposed method can improve the quality of R_{rs} spectra collected under various sky conditions (e.g., clear, scattered clouds and overcast). Second, I proposed a hybrid quasi-analytical algorithm (QAA_hybrid) instead of the QAA_v6 for retrieving more accurate a and b_b even in turbid inland waters. Third, I proposed a new algorithm to estimate a dynamic K_T/K_d ratio instead of using the fixed ratio in the original algorithm. The results obtained from *in situ* R_{rs} showed that the improved Z_{SD} estimation algorithm gave more accurate Z_{SD} estimations, with the root mean square error (RMSE) reduced from 2 m to 1.7 m, mean absolute percentage error (MAPE) reduced from 54 % to 35 % (N=472, Z_{SD} ranges from 0.2 m to 45 m).

The improved Z_{SD} estimation algorithm was applied to the 2003–2012 MERIS images for six Japanese lakes (i.e. Lakes Mashu, Kussharo, Inawashiro, Kasumigaura, Suwa and Biwa). The results obtained from 66 matchups demonstrated that the improved Z_{SD} algorithm estimated Z_{SD} values from MERIS data with the RMSE of 2 m and the MAPE of 38%, even though some overestimations were still observed in Lake Biwa due mainly to the imperfect atmospheric correction for satellite images. The satellite-derived long-term Z_{SD} trends agreed well with that

derived from the *in situ* long-term Z_{SD}. The results indicate that the improved Z_{SD} algorithm has good potential in monitoring Z_{SD} from remote sensing data.

Acknowledgements

I would like first to acknowledge my supervisor, Prof. Matsushita Bunkei, for giving me the chance to study in remote sensing of water environment. He is kind, patient and well-read, the door of his office is always open for me whenever I have a question. I cannot forget the enjoyable days during the field survey, the pleasant time when discuss with him, and the exciting feeling after finding a solution for the problem in my research. His continuous support, patient guidance and insightful suggestions provide a great help to this research.

I would like to express my appreciation to the rest of my thesis committee, Prof. Fukushima Takehiko, Prof. Nasahara Kenlo and Prof. Kato Hiroaki, for giving me valuable comments and questions.

Constructive suggestions offered by Prof. Yang Wei have been very helpful in this research. I am also grateful to Mr. Fajar Setiawan, Dr. Kawamura Shimako, Mrs. Suzuki Mika, and Mr. Takegahara with the help of laboratory experiment and field survey, Mr. Rossi Hamzah with the help of programming, and Dr. Pok Sophak, Dr. Vundo Augusto and Mr. Fu Xinyu with the help when I just came to the University of Tsukuba.

I would like to thank those who provide the data and make this research possible: The European Space Agency (ESA) for providing the MERIS satellite images, the contributors of *in situ* data in SeaBASS, Prof. Yuichi Miyabara in Shinshu University for providing the *in situ* data in Lake Suwa, the National Institute for Environmental Studies, Japan (NIES) for providing the *in* *situ* data in Lake Mashu and Lake Kasumigaura, and Shiga Prefecture for providing the *in situ* data in Lake Biwa. I appreciate the Ministry of Education, Culture, Sports, Science and Technology(MEXT), Japan for providing the scholarship.

Finally, I must show my very special gratitude to my parents for their understanding, support and encouragement.

Contents

List of Tables

List of Figures

List of Symbols

$a(\lambda)$ = absorption coefficient, m^{-1}

$a^{*}_{\mathrm{CDOM}}(\lambda)$ = specific absorption coefficient of CDOM, dimensionless

$a^{*}_{\mathrm{ph}}(\lambda)$ = specific absorption coefficient of phytoplankton, m^{2}/mg

$a^{*}_{\mathrm{tr}}(\lambda)$ = specific absorption coefficient of tripton, m^{2}/g

$a_{\mathrm{w}}(\lambda)$ = absorption coefficient of pure water, m^{-1}

$b_{\mathrm{b}}(\lambda)$ = backscattering coefficient, m^{-1}

$b_{\mathrm{bw}}(\lambda)$ = backscattering coefficient of pure water, m^{-1}

$b^{*}_{\mathrm{bph}}(\lambda)$ = specific backscattering coefficient of phytoplankton, m^{2}/mg

$b^{*}_{\mathrm{btr}}(\lambda)$ = specific backscattering coefficient of tripton, m^{2}/g

$b_{\mathrm{bp}}(\lambda)$ = backscattering coefficient of particles, m^{-1}

$c(\mathrm{v})$ = beam attenuation coefficient in visible domain, m^{-1}

C_{CDOM} = absorption coefficient of CDOM at 440 nm, m^{-1}

C_{chl} = concentration of Chl-a, mg/m^{3}

C_{t} = contrast threshold of human eye for detecting a disk, dimensionless

$C_{\mathrm{t}}^{\mathrm{r}}$ = contrast threshold of human eye for detecting a disk in radiance, sr^{-1}

C_{tr} = concentration of tripton, g/m^{3}

$E_{\mathrm{d}}(\lambda)$ = downwelling irradiance, Wm^{-2}nm^{-1}

$K_{\mathrm{d}}(\lambda)$ = diffuse attenuation coefficient of downwelling irradiance, m^{-1}

$K_{\mathrm{d}}(\mathrm{v})$ = diffuse attenuation coefficient of downwelling irradiance in visible domain, m^{-1}

$K_{\mathrm{T}}(\lambda)$ = diffuse attenuation coefficient of upwelling radiance, m^{-1}

$K_{u}^{\mathrm{B}}(\lambda)$ = diffuse attenuation coefficient of upwelling radiance from the water bottom, m^{-1}

$K_{u}^{\mathrm{C}}(\lambda)$ = diffuse attenuation coefficient of upwelling radiance from the water column scattering, m^{-1}

$L_{\mathrm{g}}(\lambda)$ = upwelling radiance from a standard gray board, $Wm^{-2}nm^{-1}sr^{-1}$

$L_{\mathrm{r}}(\lambda)$ = reflected sky radiance, $Wm^{-2}nm^{-1}sr^{-1}$

$L_{\mathrm{s}}(\lambda)$ = radiance of skylight, $Wm^{-2}nm^{-1}sr^{-1}$

$L_{\mathrm{t}}(\lambda)$ = total upwelling radiance from the water surface, $Wm^{-2}nm^{-1}sr^{-1}$

$L_{\mathrm{u}}(\lambda)$ = upwelling underwater radiance just below water surface, $Wm^{-2}nm^{-1}sr^{-1}$

$L_{\mathrm{w}}(\lambda)$ = water-leaving radiance, $Wm^{-2}nm^{-1}sr^{-1}$

N = number of data, dimensionless

n = refractive index of water, dimensionless

R^2 = determination coefficient, dimensionless

R_{t} = submerged disk reflectance, dimensionless

$R_{\mathrm{g}}(\lambda)$ = reflectance of the standard gray board, dimensionless

$R_{\mathrm{rs}}(\lambda)$ = remote sensing reflectance, sr^{-1}

R_{w} = reflectance of water body around the Secchi disk, dimensionless

$r_{\mathrm{rs}}^{\mathrm{dp}}(\lambda)$ = r_{rs} for optically deep waters, sr^{-1}

$r_{\mathrm{rs}}(\lambda)$ = remote sensing reflectance just below the water surface, sr^{-1}

Y = spectral power for backscattering coefficient of particles, dimensionless

Z_{SD} = Secchi disk depth, m

ρ = skylight reflectance, dimensionless

ρ_{B} = bottom reflectance, dimensionless

Δ = residual reflected skylight, sr^{-1}

ϕ = azimuth angle, °

Γ = coupling constant, dimensionless

λ = wavelength, nm

θ = zenith angle, °

List of Abbreviations

BEAM = Basic ERS & Envisat (A) ATSR and Meris toolbox

CDOM = Colored Dissolved Organic Matter

CI = Color Index

Chl-a = Chlorophyll-a

ESA = European Space Agency

FLH = Fluorescence Line Height

G17 = Groetsch et al., 2017

IOCCG = International Ocean Colour Coordinating Group

IOPs = Inherent Optical Properties

K13 = Kutser et al., 2013

L10 = Lee et al., 2010

Lee15 = Lee et al., 2015 (Z_{SD} algorithm)

M99 = Mobley, 1999

MAPE = Mean Absolute Percentage Error

MCI = Maximum Chlorophyll-a Index

MERIS = MEdium Resolution Imaging Spectrometer

MODIS = Moderate Resolution Imaging Spectroradiometer

NIES = National Institute for Environmental Studies, Japan

QA = Quality Assurance score

QAA = Quasi-Analytic Algorithm

R05 = Ruddick et al., 2005

RHW = Relative Height of the Water-absorption-dip-induced-reflectance-peak-at-810 nm

RMSE = Root Mean Square Error

SIOPs = Specific Inherent Optical Properties

SNAP = Sentinel Application Platform

SeaBASS = SeaWiFS Bio-optical Archive and Storage System

SeaDAS = SeaWiFS Data Analysis System

TSS = Total Suspended Solids

VIIRS = Visible Infrared Imaging Radiometer Suite

Chapter I General Introduction

1.1. Water transparency

Water transparency, also termed water clarity in aquatic science, is measured by Secchi disk depth (Z_{SD}, m) in the field. As water transparency is a direct record of water optics and an important indicator of water quality (Wernand et al., 2010), it has been a routine measurement in field survey of aquatic environments using a called Secchi disk since the 1860s (Secchi, 1864).

The measurement of Z_{SD} in a field survey is by lowering down a white or half white and half black disk into the water, the depth when the disk is no more visible is recorded as the Z_{SD} (Figure 1.1). However, measuring Z_{SD} in the field is time-consuming, laborious and costly. The collected Z_{SD} data is limited in temporal and spatial coverages, which may influence the judgement of the trophic status of a water body (Binding et al., 2015; Kim et al., 2015; Stock, 2015; Luis et al., 2019). In addition, some waters in developing countries or remote areas lack of *in situ* Z_{SD} data, possible reasons include financial shortage or physical inaccessibility (Setiawan et al., 2019).

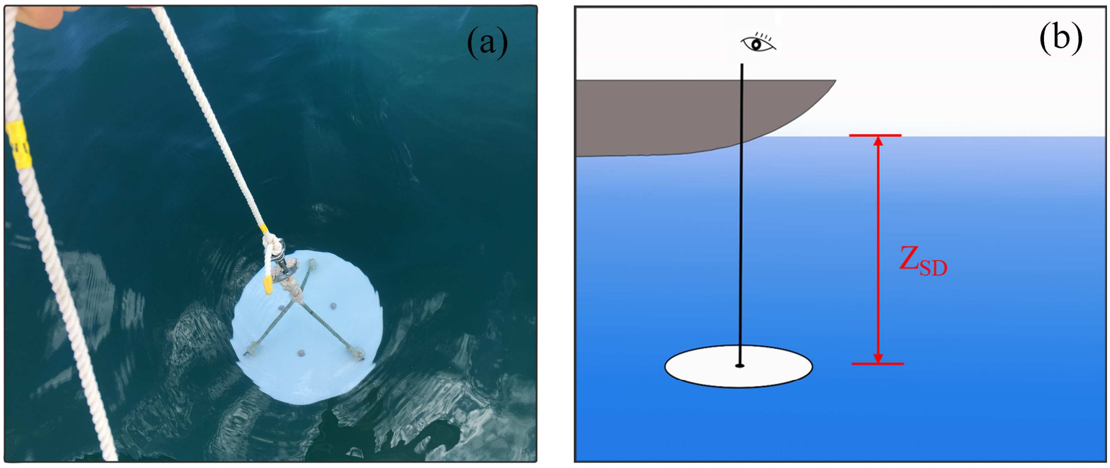

Figure 1.1. (a)Secchi disk and (b) Secchi disk depth measurement in the field.

1.2. Remote sensing of water transparency

With the development of remote sensing technique, retrieving the Z_{SD} values from space has been widely used. Compared with the field survey, remote sensing technique has many advantages, e.g. large area coverage and rapid data acquisition (Yarger and McCauley, 1975; Binding et al., 2015; Shang et al., 2016). Many satellites/sensors have been launched since 1970s, such as Landsat, Moderate Resolution Imaging Spectroradiometer (MODIS), MEdium Resolution Imaging Spectrometer (MERIS), Visible Infrared Imaging Radiometer Suite (VIIRS), Sentinel, and so on. These satellites/sensors provide long-term and various data sources for Z_{SD} monitoring.

Generally, there are two approaches for retrieving the Z_{SD} from remote sensing data: empirical and semi-analytical approaches.

1.2.1. Empirical approach

The empirical approach usually estimates the Z_{SD} by directly carrying out a regression analysis between the remote sensing data and *in situ* Z_{SD} measurements (e.g., Giardino et al., 2001; Kloiber et al., 2002; Kratzer et al., 2003; Chen et al., 2007; Olmanson et al., 2008; Kabbara et al., 2008; Kratzer et al., 2008; Zhao et al., 2011; Olmanson et al., 2016).

However, the algorithm developed based on empirical approach always need recalibration before applying to another water body, this significantly limits its usage specially in waters without *in situ* data.

1.2.2. Semi-analytical approach

The semi-analytical approach retrieves the Z_{SD} based on an underwater visibility theory (Doron et al., 2011; Fukushima et al., 2016, 2018; Alikas and Kratzer, 2017; Rodrigues et al., 2017). Compared to the empirical approach, the semi-analytical approach has two advantages: (1) a clearer mechanism and thus more reliable results; and (2) this approach often does not need *in situ* data for recalibrating the retrieval algorithm. It can thus be considered that the semi-analytical approach would be more useful for monitoring the Z_{SD} in various water bodies, especially for those that lack *in situ* measurements.

Before 2015, semi-analytical algorithms for Z_{SD} retrieval were based mainly on an underwater visibility theory proposed by Duntley (1952) (hereafter referred to as the 'classical theory'). According to the classical theory, when the air-water surface effect is neglected, the Z_{SD} is inversely proportional to the sum of the beam attenuation coefficient (c, m^{-1}) and the diffuse attenuation coefficient of downwelling irradiance (K_{d}, m^{-1}) within the visible domain (Tyler, 1968; Preisendorfer, 1986):

$$Z_{\mathrm{SD}} = \frac{\Gamma}{K_{\mathrm{d}}(\mathrm{v}) + C(\mathrm{v})} \tag{1.1}$$

$$\Gamma = \ln\left(\frac{R_{\mathrm{t}} - R_{\mathrm{w}}}{C_{\mathrm{t}} R_{\mathrm{w}}}\right), \tag{1.2}$$

where $K_{\mathrm{d}}(\mathrm{v})$ is the diffuse attenuation coefficient of downwelling irradiance (m^{-1}) in visible domain, $c(\mathrm{v})$ is the beam attenuation coefficient (m^{-1}) in visible domain, Γ is the coupling constant with a reported range of 5-10 and can also be estimated using Eq. (1.2), which R_{t} is the submerged disk reflectance, R_{w} is the reflectance of water body around the disk, and C_{t} is the threshold of contrast for detecting a disk.

However, Lee et al. (2015a, 2018) pointed out that there are some drawbacks or mistakes in the classical theory, which has been used for more than 60 years. First, the critical assumption, i.e., that the radiance distribution over the target is equal to the radiance distribution over the background, may not be valid for water bodies because a 30-cm Secchi disk cannot be treated as a point at a distance shorter than tens of meters. Second, the use of full visible domain to determine a Z_{SD} value is not appropriate because how far the human eye-brain system is able to see should depend on information from a visible wavelength with maximum transmittance in a water body. Third, the use of relative difference between water and Secchi disk just match the sharpness of an object, which is not the case of using a 30-cm Secchi disk to measure Z_{SD} within tens of meters.

To overcome the above problems, Lee et al. (2015a) proposed a new theory for underwater visibility (hereafter referred to as the 'new theory'). Based on this new theory, Lee et al. (2015a) also developed a semi-analytical algorithm for retrieving the Z_{SD} from remote sensing data (hereafter referred to as the 'Lee15'):

$$Z_{\mathrm{SD}} = \frac{1}{2.5\mathrm{Min}(K_{\mathrm{d}})} \ln\left(\frac{\left|0.14 - R_{\mathrm{rs}}^{\mathrm{PC}}\right|}{C_{\mathrm{t}}^{\mathrm{r}}}\right), \tag{1.3}$$

Where Min(K_{d}) is the minimum diffuse attenuation coefficient of downwelling irradiance (K_{d}) value in the visible domain. $R_{\mathrm{rs}}^{\mathrm{PC}}$ is the corresponding remote sensing reflectance (R_{rs}, sr^{-1}) at the band with the minimum K_{d}, and $C_{\mathrm{t}}^{\mathrm{r}}$ is the contrast threshold for sighting a white disk by eyes (i.e., 0.013 sr^{-1}). The coefficient of 2.5 was obtained under an assumption of $K_{\mathrm{T}} = 1.5K_{\mathrm{d}}$, with K_{T} is the upwelling radiance diffuse attenuation coefficient (m^{-1}).

1.3. The challenges of applying the Lee15 Z_{SD} algorithm

To retrieve accurate Z_{SD} using the Lee15 algorithm, there are three requirements: (1) accurate measurements of R_{rs}; (2) accurate estimations of K_d; and (3) the proper values of K_T/K_d ratios.

1.3.1. The problem of R_{rs}

Remote sensing reflectance (R_{rs}) is defined as the ratio of water-leaving radiance (L_w) and downwelling irradiance (E_d) just above the water surface (Kirk, 2011). It is an important parameter in ocean (water) color remote sensing, which is always required to develop estimation algorithms of water quality parameters and to evaluate the performances of the developed atmospheric correction algorithms (Wang et al., 2009; Guanter et al., 2010; Goyens et al., 2013; Jaelani et al., 2013; Wei et al., 2016; Cao et al., 2018; Jiang et al., 2019).

There are two sources of R_{rs} data, from satellite image and from field survey. Obtaining accurate R_{rs} from satellite images is still challengeable because of the difficult of atmospheric correction (Jaelani et al., 2013; Goyens et al., 2013). Because of easy operation, measuring R_{rs} in the field using the above-water approach is widely used to collect R_{rs} data (Zibordi et al., 2006; Zibordi et al., 2012). However, the L_w cannot be directly measured due to the specular reflections on the water surface caused by diffuse solar irradiance (i.e., surface-reflected radiance), which are picked-up simultaneously by this method. To solve this problem, measuring the radiance of skylight (L_s) has been suggested (as Figure 1.2 showed).

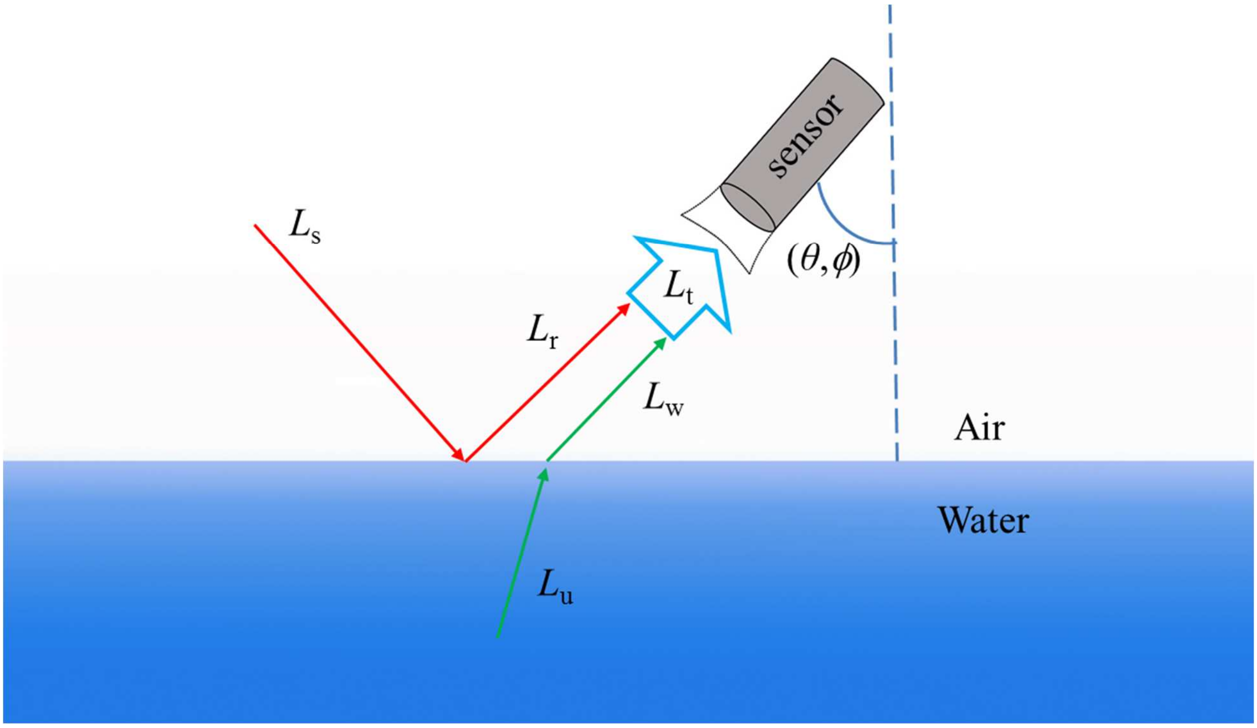

Figure 1.2. Illustration of the R_{rs} measurement using above-water approach in the field.

Finally, R_{rs} is calculated using the following equation (Mobley, 1999):

$$R_{rs}(\lambda) = \left(L_t(\lambda) - \rho L_s(\lambda)\right) / \left(\frac{\pi}{R_g(\lambda)} L_g(\lambda)\right) , \tag{1.4}$$

where $L_t(\lambda)$ is the total upwelling radiance from the water and can be directly measured by a sensor; ρ is the skylight reflectance, which is equal to 0.028 when the wind speed is less than 5 m/s and a sensor zenith angle (θ) of 40° and an azimuth angle (ϕ) of 135° are used; $L_g(\lambda)$ is the upwelling radiance from a standard gray board; and $R_g(\lambda)$ is the reflectance of the gray board. An example of the *in situ* measurement from Lake Senbako, Japan is illustrated in Figure 1.3, with measured L_t, L_s, E_d in Figure 1.3a, and the corresponding calculated R_{rs} in Figure 1.3b.

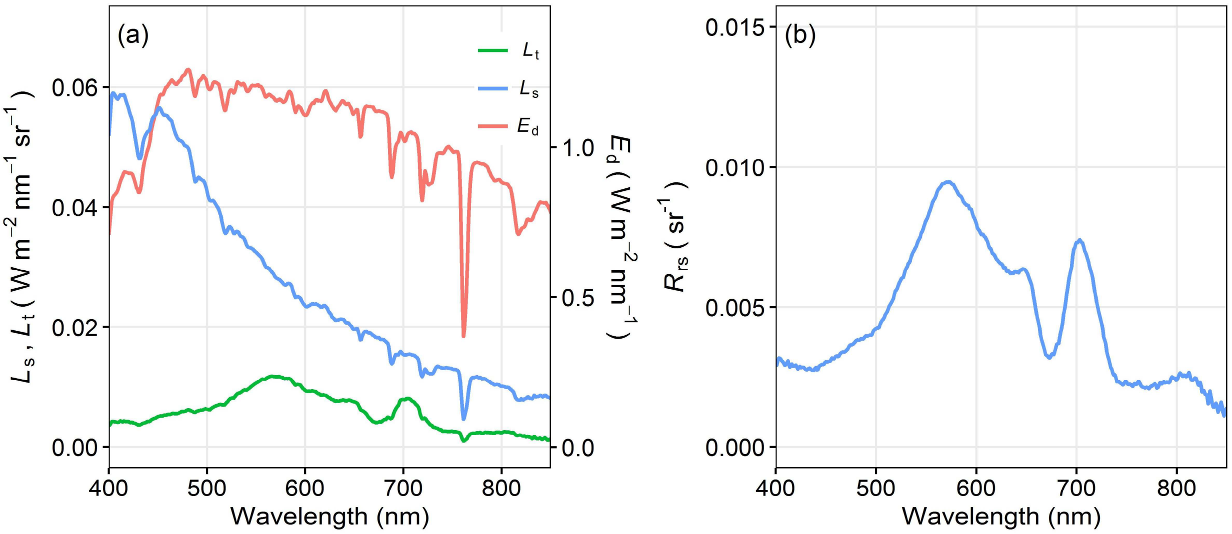

Figure 1.3. An example of *in situ* measurement in Lake Senbako. (a) measured L_t, L_s, E_d, (b) the corresponding R_{rs}.

Recently, researchers have gradually noticed that the use of only Eq. (1.4) cannot completely remove the water surface-reflected radiance (e.g., Ruddick et al., 2005; Lee et al., 2010; Kutser et al., 2013; Groetsch et al., 2017; Bernardo et al., 2018). Their results suggest that further removal of residual reflected skylight (hereafter Δ, sr^{-1}) is necessary to obtain more accurate R_{rs} spectra, i.e.:

$$R_{\mathrm{rs}}(\lambda) = \left(L_{\mathrm{t}}(\lambda) - \rho L_{\mathrm{s}}(\lambda)\right) / \left(\frac{\pi}{R_{\mathrm{g}}(\lambda)} L_{\mathrm{g}}(\lambda)\right) - \Delta \ . \qquad (1.5)$$

Currently, there are three types of approaches for removing residual reflected skylight effects (Δ). The first type involves assuming Δ to be equal to the R_{rs} value at near-infrared (for clear waters) or middle-infrared (for turbid waters) wavelengths because the R_{rs} values at these wavelengths can be assumed to be zero due to the strong absorption of pure water and the weak backscatters of suspended particles (i.e., black water assumption) (e.g., Choi et al., 2012, 2014;

Qiu, 2013; Zhang et al., 2010; Cai et al., 2015; Dierssen et al., 2006; Brewin et al., 2016; Froidefond et al., 2002; Knaeps et al., 2012; Song et al., 2012). However, since the wavelength of the black water assumption will change in different water types, it is difficult to objectively determine an appropriate wavelength.

The second type of approach is estimating $\varDelta$ based on various assumptions (e.g., Ruddick et al., 2005, 2006; Lee et al., 2010; Dev and Shanmugam, 2014). For example, Ruddick et al. (2005, 2006) found that the spectral shape in the near-infrared domain (700–900 nm) is almost invariant, and thus they proposed a similarity spectrum method under the assumption of a fixed ratio of $R_{\mathrm{rs}}(720)$ and $R_{\mathrm{rs}}(780)$ (i.e., $R_{\mathrm{rs}}(720)/R_{\mathrm{rs}}(780)=2.35$). However, as pointed out in Ruddick et al. (2005), the applicability of this method is limited to medium turbid waters with $R_{\mathrm{rs}}(720) \leq 0.0095$ sr^{-1} (corresponding to water-leaving irradiance reflectance of 0.03 in Ruddick et al., 2005). Lee et al. (2010) proposed an optimization method to estimate $\varDelta$. They first simulated the R_{rs} as the magnitude of the absorption coefficient of phytoplankton, gelbstoff and the backscattering coefficient of particles, and then solved for $\varDelta$ by matching the simulated R_{rs} with the *in situ*-measured R_{rs} spectra. However, since the method requires the specific inherent optical properties (SIOPs) of each optical active matter in a water body to generate synthetic R_{rs} spectra, it can be considered that a larger error will occur if the method is applied to a water body with different SIOPs. In addition, the wavelength ranges used for optimization should be changed according to the turbidity of a water body (Lee et al., 2010).

The third type of approach involves directly estimating the surface-reflected radiance rather than estimating Δ (Kutser et al., 2013; Groetsch et al., 2017). Kutser et al. (2013) found that the surface-reflected radiance can be obtained by fitting the spectral ranges of 350–380 nm and 890–900 nm using a power function. However, this finding is only suitable for colored dissolved organic matter (CDOM)-rich waters (Kutser et al., 2013). Groetsch et al. (2017) proposed to apply a three-component reflectance model (3C) to above-water radiometric measurements for estimating surface-reflected radiance. Similar to the method of Lee et al. (2010), the 3C-based method also needs SIOPs to generate synthetic L_t spectra for optimization, and thus has limitations in its application to waters with different SIOPs.

Therefore, developing a new simple method which is applicable for various waters for removing the residual reflected skylight effects in above-water measured spectra is necessary.

1.3.2. The problem of K_d

The diffuse attenuation coefficient of downwelling irradiance (K_d) can be estimated from absorption coefficient (a, m^{-1}) and backscattering coefficient (b_b, m^{-1}) using the following equation (Lee et al., 2005, 2013):

$$K_\mathrm{d}(\lambda) = (1 + 0.005\theta)a(\lambda) + 4.259\left(1 - 0.265\eta_\mathrm{w}(\lambda)\right)\left(1 - 0.52e^{-10.8a(\lambda)}\right)b_\mathrm{b}(\lambda), \quad (1.6)$$

where θ is the solar zenith angle, $\eta_\mathrm{w}(\lambda)$ is the ratio of $b_\mathrm{bw}(\lambda)$ (the backscattering coefficient of pure water, Morel, 1974; Zhang et al., 2009) and $b_\mathrm{b}(\lambda)$. $a(\lambda)$ and $b_\mathrm{b}(\lambda)$ can be estimated from $R_\mathrm{rs}(\lambda)$ using the sixth version of Quasi-analytic algorithm (QAA_v6, Lee et al., 2002; IOCCG, 2014). However, several research groups have reported that the QAA_v6 or its previous version

(QAA_v5) often failed in turbid inland waters (Le et al., 2009; Yang et al., 2013; Huang et al., 2014; Mishra et al., 2014; Watanabe et al., 2016; Wang et al., 2017), which will lead errors in K_d estimations. It is thus necessary to propose a QAA which can retrieve accurate a and b_b in various waters and then used for calculating accurate K_d.

1.3.3. The problem of the K_T/K_d ratio

For the ratio of K_T and K_d, empirically, the constant ratio value of 1.5 was used in the original Lee15 algorithm (i.e., $K_T = 1.5K_d$). However, a wide range of ratios have been reported (0.5–2.0). For example, Philpot (1989) pointed out that the reasonable range for K_T/K_d was from 0.5 to 2. Maritorena et al. (1994) reported that K_T/K_d ranged from 1.02 to 1.66 based on simulations. A K_T/K_d range of 1.4–1.7 can also be estimated when the solar zenith angle $\theta = 0$ degrees according to Lee et al. (1994). It can thus be speculated that using a fixed K_T/K_d value in a Z_{SD} estimation may lead to errors, and more realistic K_T/K_d ratios are needed to further improve the performance of the Lee15 algorithm.

1.4. Research objectives of this study

To enable the Lee15 Z_{SD} algorithm to estimate accurate Z_{SD} values in various water types, the above mentioned three problems (i.e. problems of R_{rs}, K_d, K_T/K_d ratio) should be addressed. Thus, the objectives of this study are to:

(1) develop a new method to remove the residual reflected skylight (Δ) in the above-water

measured R_{rs}, to ensure the accuracy of R_{rs} for various types of waters (chapter II);

(2) integrate different types of QAAs to estimate more accurate a and b_b for both clear and turbid waters, thus to ensure the accuracy of K_d estimations for both clear and turbid waters (chapter III);

(3) propose a new algorithm to calculate more accurate ratio of K_T/K_d, and replace the constant K_T/K_d =1.5 with a dynamic K_T/K_d in the Z_{SD} estimation algorithm (chapter III);

(4) validate the improved Z_{SD} algorithm by using *in situ* spectrum collected from field survey in Japan and downloaded data from SeaBASS database (chapter III);

(5) apply the improved Z_{SD} algorithm to MERIS satellite images over six Japanese Lakes, Lake Mashu, Lake Kussharo, Lake Inawashiro, Lake Kasumigaura, Lake Suwa and Lake Biwa, between 2003 and 2012, to produce the long-term Z_{SD} products and analyze the changing trend of Z_{SD} over these six Japanese Lakes (chapter IV).

Chapter II A Simple and Effective Method for Removing Residual Reflected Skylight in Above-water Remote Sensing Reflectance Measurements

2.1. Introduction

As mentioned in chapter I, remote sensing reflectance (R_{rs}) measured using above-water approach suffers from the problem of residual reflected skylight ($\mathit{\Delta}$). Existing methods for removing the $\mathit{\Delta}$ effects either limited for specific waters (e.g. clear water or CDOM-rich water) or complicated to execute (need SIOPs or optimization method).

In this chapter, the problem of $\mathit{\Delta}$ effects in R_{rs} will be addressed. The detailed objectives are to: (1) develop a new method for removing the $\mathit{\Delta}$ effects in above-water R_{rs} measurements that can overcome the shortcomings in the existing methods; (2) evaluate the performance of the proposed method by comparing it with four existing methods using both simulated and *in situ* collected data.

2.2. Methods

2.2.1. Data collection

2.2.1.1. *In situ* data collection

In situ R_{rs} spectra and corresponding Secchi disk depth (Z_{SD}) data were collected from field surveys in 21 Japanese inland waters during 2009 and 2019 and the SeaWiFS Bio-optical Archive and Storage System (SeaBASS) database.

The 21 Japanese inland waters include 20 lakes and 1 bay (Tokyo Bay; Figure 2.1a), with Z_{SD} values ranging from 0.3 m to 16.4 m, chlorophyll-a (Chl-a) concentrations ranging from 0.5 mg/m^3 to 187.7 mg/m^3, and total suspended solids (TSS) concentrations ranging from 0.4 g/m^3 to 73.7 g/m^3 (Table 2.1). For each site, the radiance of the skylight (L_s), the radiance from a standard board (L_g), and the total upwelling radiance from the water (L_t) were measured using a FieldSpec® HandHeld spectroradiometer (ASD Inc., Boulder, CO) with a sensor zenith angle (θ) of 40° and an azimuth angle (ϕ) of 135°. The R_{rs} was then calculated using Eq. (1.4) with the skylight reflectance ρ =0.028 (when the wind speed was < 5 m/s, Mobley, 1999). Z_{SD} was measured by lowering a 30 cm diameter white disk into the water until the disk was no longer visible. I kept all R_{rs} spectra collected under different sky conditions (i.e., clear, scattered clouds, and overcast). These sky conditions were distinguished using the method of Groetsch et al. (2017). In total, 305 pairs of *in situ* R_{rs} spectra and corresponding Z_{SD} values were obtained from Japanese inland waters.

Moreover, three experiments were carried out in two Japanese lakes (Lake Kasumigaura with Z_{SD}=0.8 m on March 12, 2019 and Lake Chuzenji with Z_{SD}=9.7 m on June 4, 2019) and one Indonesian lake (Lake Tamblingan with Z_{SD}=2.1 m on March 20, 2019). Except for *in situ* R_{rs} spectra measured using the above-water approach, three Δ-free R_{rs} spectra were also measured using RAMSES spectroradiometer (TriOS, Rastede, Germany). Since a black tube (5 cm) was installed in front of the downward radiance sensor and kept just below water surface, L_w was directly measured without Δ effects (Lee et al., 2010; Kutser et al., 2013). At the same time, E_d

just above the water surface was measured using an upward irradiance sensor. All R_{rs} spectra were measured under clear sky condition with wind speed lower than 5 m/s.

For the SeaBASS database, I only chose the R_{rs} spectra with wavelengths ranging from 400 nm to 850 nm and the corresponding Z_{SD} values. As a result, a total of 167 data pairs were obtained. These data pairs were collected from San Francisco Bay, the northern Gulf of Mexico, Chesapeake Bay, and Lake Erie (Figure 2.1b). The Δ corrections had already been carried out by the providers for some of the selected *in situ* R_{rs} spectra. The Z_{SD} values of the selected data pairs ranged from 0.2 m to 45 m.

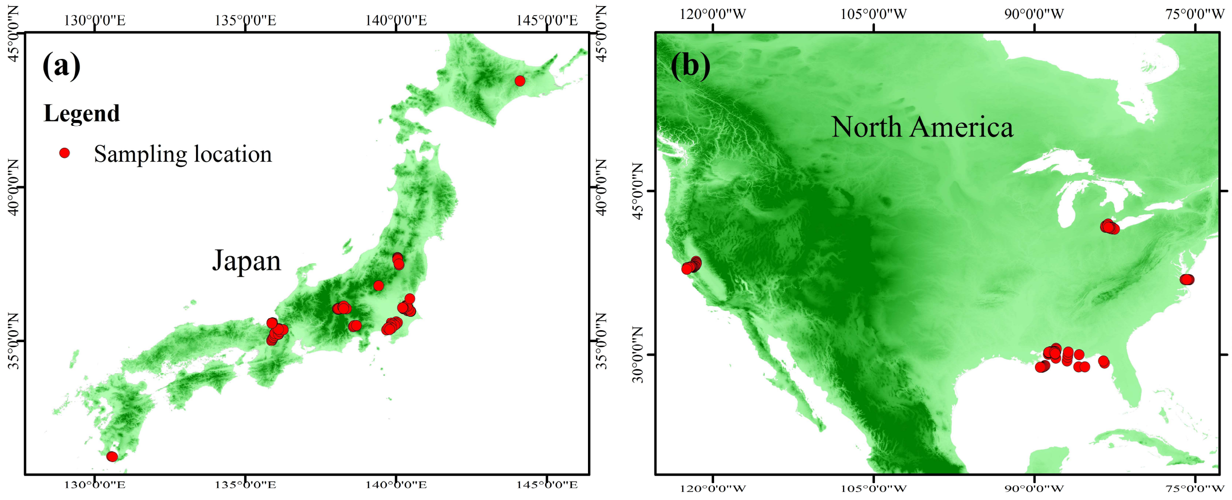

Figure 2.1. Locations of *in situ* data used in this study. (a) Data collected from 21 Japanese inland waters; (b) data collected from SeaBASS.

Table 2.1. Name, area, Z_{SD}, Chl-a, TSS, and number of data of the 21 Japanese inland waters.

Name	Area (km^2)	Z_{SD} (m)	Chl-a (mg/m^3)	TSS (g/m^3)	Number of data	Sampling year
Biwa	670.3	2.3-10.7	0.6-7.0	0.6-3.4	58	2009-2011
Kasumigaura	167.6	0.3-1.2	12.0-187.7	4.1-73.7	181	2009-2019
Inawashino	103.3	9.3-10	0.6-0.7	1.0-1.1	2	2010
Akan	13.0	6.7	0.8	1.5	1	2013

Suwa	12.9	0.9-1.9	9.8-29.4	4.4-9.6	21	2010-2018
Ikeda	10.9	9.3	1.4	0.7	1	2011
Hibara	10.7	6.1-7.3	1.7-2.3	1.0-1.3	4	2018
Motosu	4.7	9.3-16.4	0.6	0.4	2	2014
Suigetsu	4.2	1.0-1.5	3.9	3.6	2	2016
Mikata	3.6	0.8	6.3	8.0	1	2016
Sai	2.1	6.8-7.1	1.8	1.3	2	2014
Kugushi	1.4	1.4	27.4	5.9	1	2016
Unagi	1.2	12.8	0.5	0.4	1	2011
Suga	0.9	0.8	57.0	7.5	1	2016
Shoji	0.5	3.5-4.2	3.2-8.5	1.7-2.4	2	2014
Shirakaba	0.4	1.0-3.5	2.3-26.9	2.8-9.1	3	2010-2018
Senbako	0.33	0.6	98.9	29.2	1	2019
Yunoko	0.32	3.4	4.5	1.9	1	2011
Megami	0.12	2.4	5.7	3.8	1	2018
Tateshina	0.08	2.5	6.5	3.1	1	2018
Tokyo Bay	1500	1.9-5.5	2.9-32.0	2.1-4.3	18	2010-2011
Total	--	0.3-16.4	0.5-187.7	0.4-73.7	305	2009-2019

2.2.1.2. Generating synthetic data

As it is very difficult to measure an error-free R_{rs} spectrum in the field, I used a bio-optical model to obtain error-free R_{rs} spectra. The bio-optical model can be expressed as follows (Gordon et al., 1988; Lee et al., 2002):

$$R_{\mathrm{rs}}(\lambda) = \frac{0.52 r_{\mathrm{rs}}(\lambda)}{1-1.7 r_{\mathrm{rs}}(\lambda)} \tag{2.1}$$

$$r_{\mathrm{rs}}(\lambda) = 0.089\left(\frac{b_{\mathrm{b}}(\lambda)}{a(\lambda)+b_{\mathrm{b}}(\lambda)}\right) + 0.125\left(\frac{b_{\mathrm{b}}(\lambda)}{a(\lambda)+b_{\mathrm{b}}(\lambda)}\right)^2 , \tag{2.2}$$

where $r_{\mathrm{rs}}(\lambda)$ is the remote sensing reflectance just below the water surface, $a(\lambda)$ is the total absorption coefficient of water, and $b_{\mathrm{b}}(\lambda)$ is the total backscattering coefficient of water. The $a(\lambda)$ and $b_{\mathrm{b}}(\lambda)$ can be further separated as follows (Vahtmäe et al., 2006; Yang et al., 2011):

$$a(\lambda) = C_{\mathrm{chl}} \cdot a^*_{\mathrm{ph}}(\lambda) + C_{\mathrm{tr}} \cdot a^*_{\mathrm{tr}}(\lambda) + C_{\mathrm{CDOM}} \cdot a^*_{\mathrm{CDOM}}(\lambda) + a_{\mathrm{w}}(\lambda) \tag{2.3}$$

$$b_{\mathrm{b}}(\lambda) = C_{\mathrm{chl}} \cdot b^{*}_{\mathrm{bph}}(\lambda) + C_{\mathrm{tr}} \cdot b^{*}_{\mathrm{btr}}(\lambda) + b_{\mathrm{bw}}(\lambda) \ , \tag{2.4}$$

where C_{chl} is the concentration of Chl-a, C_{tr} is the concentration of tripton, and C_{CDOM} is the absorption coefficient of CDOM at 440 nm. The parameters $a^{*}_{\mathrm{ph}}(\lambda)$, $a^{*}_{\mathrm{tr}}(\lambda)$, and $a^{*}_{\mathrm{CDOM}}(\lambda)$ are the specific absorption coefficients of phytoplankton, tripton, and CDOM, respectively. $b^{*}_{\mathrm{bph}}(\lambda)$ and $b^{*}_{\mathrm{btr}}(\lambda)$ are the specific backscattering coefficients of phytoplankton and tripton, respectively. $a_{\mathrm{w}}(\lambda)$ is the absorption coefficient of pure water (Kou et al., 1993; Pope and Fry, 1997; Lee et al., 2015b), and $b_{\mathrm{bw}}(\lambda)$ is the backscattering coefficient of pure water (Zhang et al., 2009).

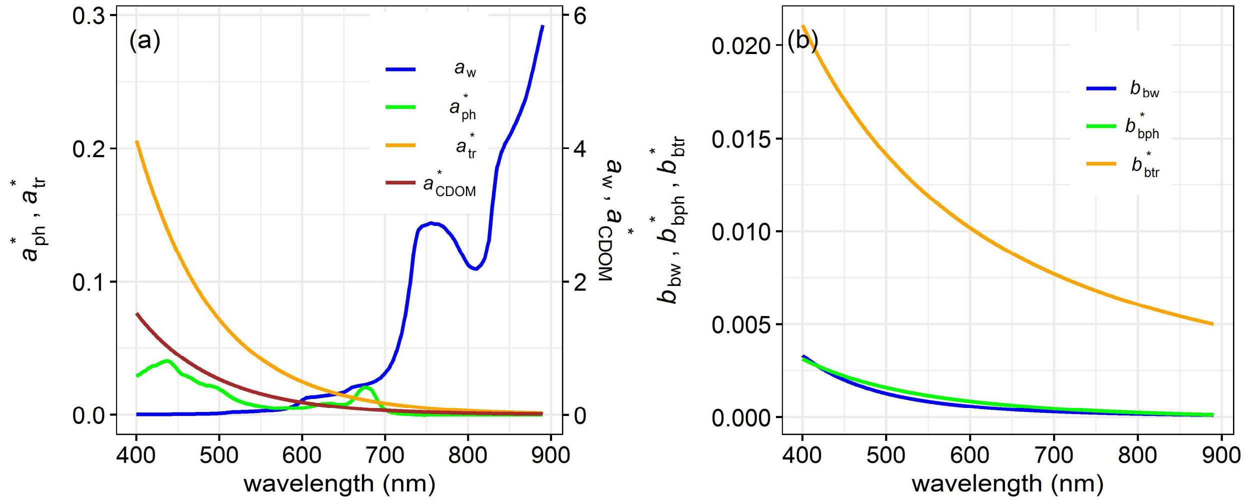

Figure 2.2. Specific inherent optical properties (SIOPs) collected from Lake Kasumigaura, Japan, on May 11, 2018. (a) a_{w} (m^{-1}), a^{*}_{ph} (m^2/mg), a^{*}_{tr} (m^2/g), and a^{*}_{CDOM} (dimensionless); (b) b_{bw} (m^{-1}), b^{*}_{bph} (m^2/mg) and b^{*}_{btr} (m^2/g).

I generated two synthetic datasets using the above bio-optical model (hereafter Synthetic Dataset I and Synthetic Dataset III), and another synthetic dataset using Hydrolight (Mobley, 1994; hereafter Synthetic Dataset II). Dataset I was used to develop a method for Δ correction, and

Dataset II and Dataset III were used to evaluate the performance of the developed method.

Synthetic Dataset I was generated for various water turbidities. The concentrations of Chl-a and tripton were varied between 0.01 mg/m^3 and 300 mg/m^3 and between 0.01 g/m^3 and 300 g/m^3, respectively. The absorption coefficient of CDOM at 440 nm was varied between 0.01 m^{-1} and 10 m^{-1}. The intervals of the Chl-a (tripton) concentration were 0.01 mg/m^3 (g/m^3) for 0.01–0.1 mg/m^3 (g/m^3), 0.1 mg/m^3 (g/m^3) for 0.1–1.0 mg/m^3 (g/m^3), 1.0 mg/m^3 (g/m^3) for 1.0–10 mg/m^3 (g/m^3), 2 mg/m^3 (g/m^3) for 10–20 mg/m^3 (g/m^3), 5 mg/m^3 (g/m^3) for 20–50 mg/m^3 (g/m^3), 10 mg/m^3 (g/m^3) for 50–100 mg/m^3, and 20 mg/m^3(g/m^3) for 100–300 mg/m^3(g/m^3). For CDOM, the intervals were 0.01 m^{-1} for 0.01–0.1 m^{-1}, 0.1 m^{-1} for 0.1–1.0 m^{-1}, 1.0 m^{-1} for 1.0–5 m^{-1}, and 2 m^{-1} for 5–10 m^{-1}. The SIOPs were collected from Lake Kasumigaura on May 11, 2018 (Figure 2. 2). In total, 75816 error-free R_{rs} spectra were generated. Figure 2.3 shows 200 randomly selected examples of simulated R_{rs} spectra.

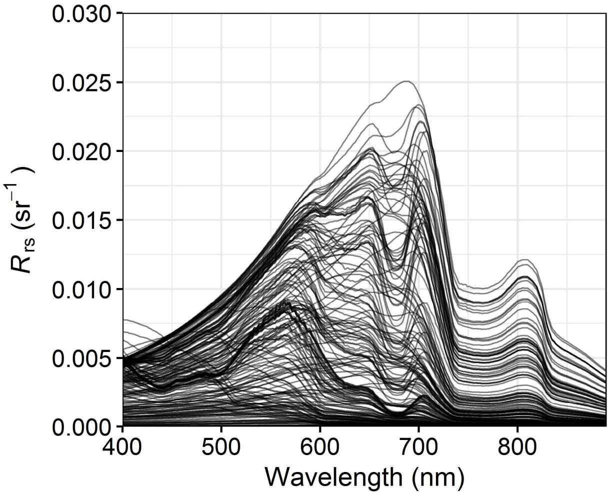

Figure 2.3. 200 randomly selected R_{rs} spectra from Synthetic Dataset I.

Synthetic Dataset II was generated using the Hydrolight radiative transfer model (version 5, Sequoia Scientific), which can solve the radiative transfer equation to compute the radiance distribution within and leaving a water body. The Hydrolight provides default SIOPs for four components (pure water, Chl-a, mineral particles, and CDOM), which were directly used in this study.

The water was assumed to be homogeneous and of infinite depth. Raman scattering was ignored in this simulation. The refraction index was set as 1.34, and the sun zenith angle was kept at 30 degrees. The semi-empirical sky-model based on RADTRAN was used to simulate the solar and sky irradiance incident onto the water surface. The Chl-a concentration was set as 35 mg/m^3, the mineral particles concentration was set as 15 g/m^3, and the CDOM absorption coefficient at 440 nm was set as 0.8 m^{-1}.

To simulate various environmental conditions that people may face in the field, I ran the Hydrolight by combining different wind speeds, cloud cover percentages, and view geometries (Table 2.2). In total, I simulated 12 cases and obtained the corresponding L_t, $L_{s,}$ and E_d spectra between 350–900 nm with a 5 nm interval. The R_{rs} spectrum simulated under the conditions of a clear sky, wind speed=0 m/s, and the recommended view geometry (θ=40°, ϕ=135°) was considered to be Δ-free R_{rs} (i.e., Case 1 in Table 2.2). The other 11 R_{rs} spectra calculated from the simulated L_t, $L_{s,}$ and E_d spectra by Eq. (1.4) were considered to be Δ-contaminated R_{rs} and were used to evaluate the proposed Δ correction method.

Table 2.2. Conditions of radiative transfer simulation for generating Synthetic Dataset II.

Case	Wind speed (m/s)	Cloud cover (%)	View geometry(θ,ϕ)
1 (Δ-free)	0	0 (clear sky)	(40°, 135°)
2 (with Δ effects)	0	50 (scattered clouds)	(40°, 135°)
3 (with Δ effects)	0	100 (overcast)	(40°, 135°)
4 (with Δ effects)	10	0 (clear sky)	(40°, 135°)
5 (with Δ effects)	10	50 (scattered clouds)	(40°, 135°)
6 (with Δ effects)	10	100 (overcast)	(40°, 135°)
7 (with Δ effects)	0	0 (clear sky)	(50°, 90°)
8 (with Δ effects)	0	50 (scattered clouds)	(50°, 90°)
9 (with Δ effects)	0	100 (overcast)	(50°, 90°)
10 (with Δ effects)	10	0 (clear sky)	(50°, 90°)
11 (with Δ effects)	10	50 (scattered clouds)	(50°, 90°)
12 (with Δ effects)	10	100 (overcast)	(50°, 90°)

For Synthetic Dataset III, I first randomly selected 1000 Chl-a concentrations in the range of 0.01–300 mg/m^3, 1000 tripton concentrations in the range of 0.01–300 g/m^3, and 1000 absorption coefficients of CDOM at 440 nm in the range of 0.01–10 m^{-1}, to generate 1000 error-free R_{rs} spectra using the same bio-optical model described above. Secondly, I randomly generated 1000 Δ values in the range of 0 sr^{-1} to 0.01 sr^{-1} (true Δ) and added them to each error-free R_{rs} spectra to generate 1000 Δ-contaminated R_{rs} spectra. Synthetic Dataset III was used to evaluate the performance of the proposed method by comparing the estimated Δ values using the proposed method with the true Δ values.

2.2.2. Model development

2.2.2.1. Find an index without Δ effect

Residual reflected skylight (i.e., Δ), such as an error due to an imperfect atmospheric correction, is a kind of noise from the light environment in addition to the R_{rs} spectrum. Therefore, the Δ effect can be minimized/removed using baseline-based indices such as FLH (Fluorescence Line Height), MCI (Maximum Chlorophyll-a Index), CI (Color Index) and so on, if assuming the Δ is a wavelength-independent variable (e.g., Gower, 1980; Gower et al., 2005; Hu et al., 2012; Matsushita et al., 2016).

On the other hand, to make a baseline-based index that can be applied to various waters, it is desirable that the index be insensitive to the variation of water SIOPs. From Figure 2.2, it can be seen that the SIOPs in the near-infrared domain are only dominated by the absorption coefficient of pure water. Therefore, a baseline-based index using near-infrared wavelengths can meet this requirement.

According to the above considerations, I noticed that the relative height of the water-absorption-dip-induced-reflectance-peak-at-810 nm (hereafter RHW; Figures 2.2 and 2.3) can meet both requirements. The RHW can be calculated using the following equations:

$$\mathrm{RHW} = R_{\mathrm{rs}}(810) - R'_{\mathrm{rs}}(810) \tag{2.5}$$

$$R'_{\mathrm{rs}}(810) = R_{\mathrm{rs}}(780) + \left(R_{\mathrm{rs}}(840) - R_{\mathrm{rs}}(780)\right) \times (810 - 780)/(840 - 780), \tag{2.6}$$

where $R_{\mathrm{rs}}(780)$, $R_{\mathrm{rs}}(810)$, and $R_{\mathrm{rs}}(840)$ are the remote sensing reflectance at 780 nm, 810 nm, and 840 nm measured from above the water surface, respectively.

2.2.2.2. Estimating Δ-free $R_{\mathrm{rs}}(750)$ from RHW

Previous studies have confirmed that there exists a strong correlation between the concentration of TSS and R_{rs} values in the near-infrared domain (e.g., Nechad et al., 2010; Yang et al., 2011). Therefore, TSS can be expressed as follows using R_{rs} values in the near-infrared domain. For example:

$$\mathrm{TSS}=f_1(R_{\mathrm{rs}}(750)) \tag{2.7}$$

$$\mathrm{TSS}=f_2(R_{\mathrm{rs}}(780)) \tag{2.8}$$

$$\mathrm{TSS}=f_3(R_{\mathrm{rs}}(810)) \tag{2.9}$$

$$\mathrm{TSS}=f_4(R_{\mathrm{rs}}(840)), \tag{2.10}$$

where $f_1 - f_4$ represent functions to obtain TSS from R_{rs} values in the near-infrared domain. From Eqs. (2.7) – (2.10), the following relationships can be obtained:

$$R_{\mathrm{rs}}(780)=f_5(R_{\mathrm{rs}}(750)) \tag{2.11}$$

$$R_{\mathrm{rs}}(810)=f_6(R_{\mathrm{rs}}(750)) \tag{2.12}$$

$$R_{\mathrm{rs}}(840)=f_7(R_{\mathrm{rs}}(750)), \tag{2.13}$$

where $f_5 - f_7$ represent functions to obtain $R_{\mathrm{rs}}(780)$, $R_{\mathrm{rs}}(810)$, and $R_{\mathrm{rs}}(840)$ from $R_{\mathrm{rs}}(750)$. By combining Eqs. (2.5) – (2.6) and Eqs. (2.11) – (2.13), thus the following equation can be obtained:

$$R_{\mathrm{rs}}(750)=f_8(\mathrm{RHW}), \tag{2.14}$$

where f_8 represents a function to obtain $R_{\mathrm{rs}}(750)$ from RHW. Eq. (2.14) indicates that $\mathit{\Delta}$-free $R_{\mathrm{rs}}(750)$ can be obtained even when using R_{rs} spectra with $\mathit{\Delta}$ effects if a relationship between $\mathit{\Delta}$-free $R_{\mathrm{rs}}(750)$ and RHW was constructed.

To construct the relationship between $\mathit{\Delta}$-free $R_{\mathrm{rs}}(750)$ and RHW, I used Synthetic Dataset I ($N = 75816$). In addition, by considering larger noise effects on an *in situ*-measured R_{rs} spectrum in the near-infrared domain due to the low signal-to-noise ratio at these wavelengths, especially for *in situ* R_{rs} collected from clear waters, I suggest the use of the median R_{rs} value between $R_{\mathrm{rs}}(750)$ and $R_{\mathrm{rs}}(780)$ instead of the use of a single wavelength of $R_{\mathrm{rs}}(750)$ (hereafter Median[$R_{\mathrm{rs}}(750)$, $R_{\mathrm{rs}}(780)$]). I also used the median R_{rs} values between $R_{\mathrm{rs}}(775)$–$R_{\mathrm{rs}}(785)$, $R_{\mathrm{rs}}(805)$–$R_{\mathrm{rs}}(815)$, and $R_{\mathrm{rs}}(835)$–$R_{\mathrm{rs}}(845)$ instead of the single wavelengths of $R_{\mathrm{rs}}(780)$, $R_{\mathrm{rs}}(810)$, and $R_{\mathrm{rs}}(840)$ for the RHW calculation.

Figure 2.4 shows the relationship between Median[$R_{\mathrm{rs}}(750)$, $R_{\mathrm{rs}}(780)$] and RHW. It can be seen that there exists a very good nonlinear relationship between the two variables, with R^2=1.0. The nonlinear relationship is as follows:

$$\mathrm{Median}[R_{\mathrm{rs}}(750), R_{\mathrm{rs}}(780)] = 20170.853\mathrm{RHW}^3 - 111.611\mathrm{RHW}^2 + 2.967\mathrm{RHW}. \quad (2.15)$$

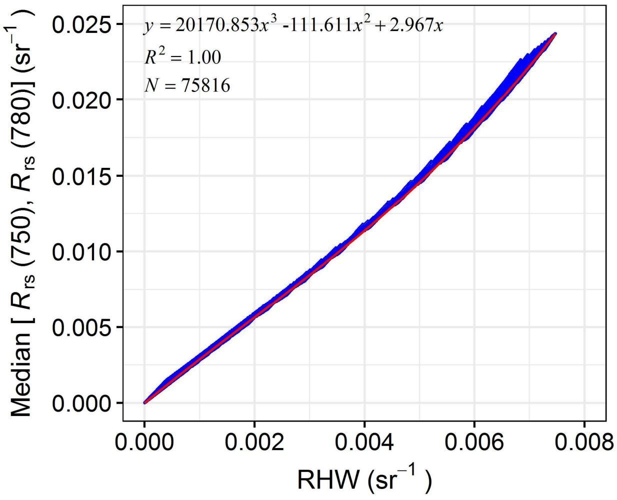

Figure 2.4. Relationship between Median[$R_{\mathrm{rs}}(750)$, $R_{\mathrm{rs}}(780)$] and RHW obtained from Synthetic Dataset I.

2.2.2.3. Estimating $\mathit{\Delta}$

First, the R_{rs} can be calculated from the measured L_{s}, L_{t}, and L_{g} using Eq. (1.4), and obtain the median R_{rs} value between $R_{\mathrm{rs}}(750)$ and $R_{\mathrm{rs}}(780)$ (hereafter referred to as measured-Median[$R_{\mathrm{rs}}(750)$, $R_{\mathrm{rs}}(780)$]). Clearly, the measured-Median[$R_{\mathrm{rs}}(750)$, $R_{\mathrm{rs}}(780)$] value contains an $\mathit{\Delta}$ effect. Then, based on the assumption of a wavelength independent of $\mathit{\Delta}$, it can be considered that one can estimate $\mathit{\Delta}$-free Median[$R_{\mathrm{rs}}(750)$, $R_{\mathrm{rs}}(780)$] using Eq. (2.15) even if an R_{rs} spectrum with an $\mathit{\Delta}$ effect was used (hereafter referred to as estimated-Median[$R_{\mathrm{rs}}(750)$, $R_{\mathrm{rs}}(780)$]). Finally, $\mathit{\Delta}$ can be calculated by taking the difference between measured-Median[$R_{\mathrm{rs}}(750)$, $R_{\mathrm{rs}}(780)$] and estimated-Median[$R_{\mathrm{rs}}(750)$, $R_{\mathrm{rs}}(780)$].

Practically speaking, to further reduce the noise effects on *in situ*-measured R_{rs} spectra, the implementation of a Savitzky–Golay filter with a 21 nm window is recommended after calculating R_{rs} spectra using Eq. (1.4). The flowchart for $\mathit{\Delta}$ correction is shown in Figure 2.5.

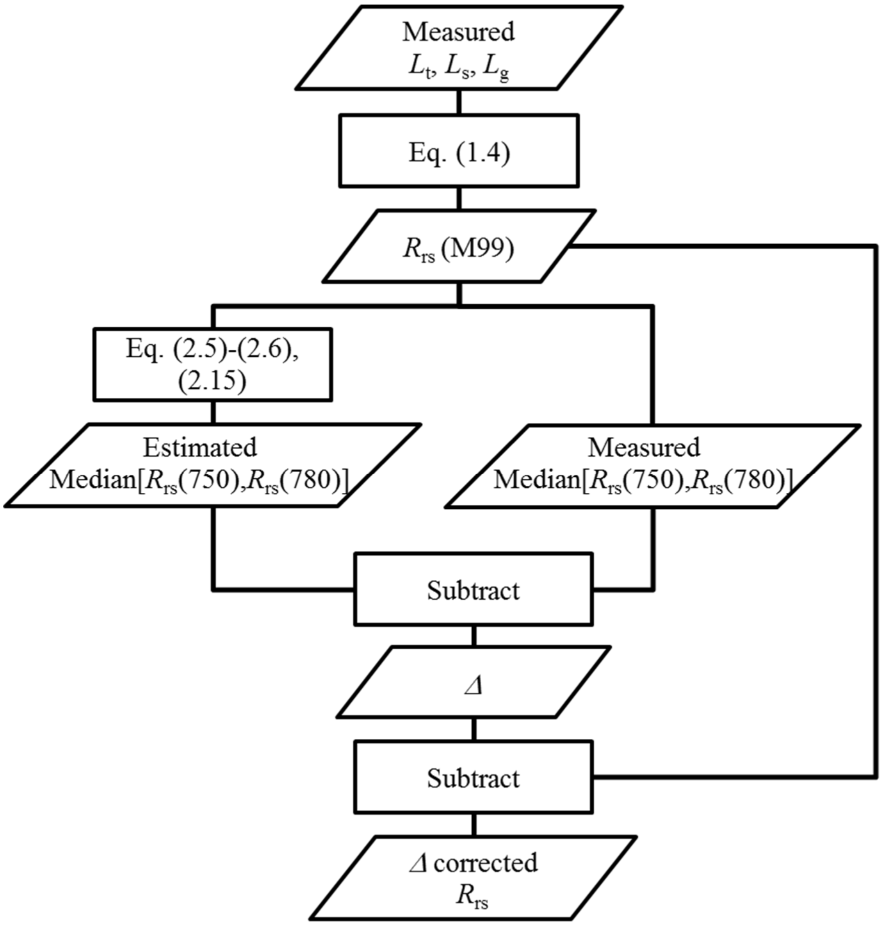

Figure 2.5. Flowchart of the proposed method for Δ correction. R_{rs}(M99) represents the remote sensing reflectance calculated using Eq. (1.4) (Mobley, 1999).

2.2.3. Accuracy assessment

I mainly used the root mean square error (RMSE), the mean absolute percentage error (MAPE), and bias to evaluate the performance of the proposed method. The equations are as follows:

$$\mathrm{RMSE} = \sqrt{\frac{\sum_{i=1}^{N}\left(X_{\mathrm{estimated},i}-X_{\mathrm{measured},i}\right)^2}{N}} \tag{2.16}$$

$$\mathrm{MAPE} = \frac{1}{N}\sum_{i=1}^{N}\left|\frac{X_{\mathrm{estimated},i}-X_{\mathrm{measured},i}}{X_{\mathrm{measured},i}}\right| \cdot 100\% \tag{2.17}$$

$$\mathrm{Bias} = \frac{1}{N}\sum_{i=1}^{N}\left(X_{\mathrm{estimated},i}-X_{\mathrm{measured},i}\right)\ , \tag{2.18}$$

where $X_{\mathrm{estimated}}$ is the estimated parameter (e.g., R_{rs}, Δ), X_{measured} is the corresponding *in situ* measurement (or true value), and N is the number of data pairs. The regression results between estimated and *in situ*-measured parameters were also used for assistance (e.g., slope, intercept, and R^2).

In addition, a spectral quality assessment system proposed by Wei et al. (2016) was also used to calculate quality assurance (QA) scores for the R_{rs} spectra before and after Δ corrections. The QA scores can vary from 0/9 (which means that none of the 9 tested wavelengths can be used, i.e., unusable R_{rs} spectra) to 9/9 (which means that all 9 tested wavelengths are useful, i.e., perfect R_{rs} spectra).

The performances of the four existing methods for Δ correction were also evaluated using the above indices and compared to the new method. The four existing methods were proposed by Ruddick et al. (2005, hereafter R05), Lee et al. (2010, hereafter L10), Kutser et al. (2013, hereafter K13), and Groetsch et al. (2017, hereafter G17), respectively. Note that the K13 method and G17 method were only applied to R_{rs} spectra collected in Japan and Indonesia, as these two methods require L_{s}, L_{t}, and E_{d} as inputs, which are not available from the SeaBASS database. In addition, I refer to the method proposed by Mobley (1999, i.e. Eq. (1.4)) with a fixed ρ value of 0.028 as “M99” in this study.

2.3. Results

2.3.1. Evaluation using *in situ* data

Figure 2.6 shows the comparisons of above-water R_{rs} measurements corrected by different methods (solid lines) and corresponding *in situ*-measured Δ-free R_{rs} spectra (dashed lines) in two Japanese lakes and one Indonesian lake. It can be seen that: (1) overall, the method proposed in this study showed the best performance with the smallest RMSE (0.00047 sr^{-1}), MAPE (57%), and bias (0.00014 sr^{-1}), but also with noticeable inconsistencies at wavelengths shorter than 450 nm in the two Japanese lakes (red and blue lines in Figure 2.6f); (2) the K13 method failed in correcting all above-water R_{rs} measurements with the largest error indices (Figure 2.6b); (3) the G17 method and the L10 method mainly showed worse performance than the proposed method in this study in Lake Kasumigaura (red lines in Figure 2.6c) and Lake Tamblingan (green lines in Figure 2.6d), respectively; and (4) comparing to the method proposed in this study, the R05 method had lower accuracy in Lake Kasumigaura and similar accuracies in the other two lakes (Figure 2.6e).

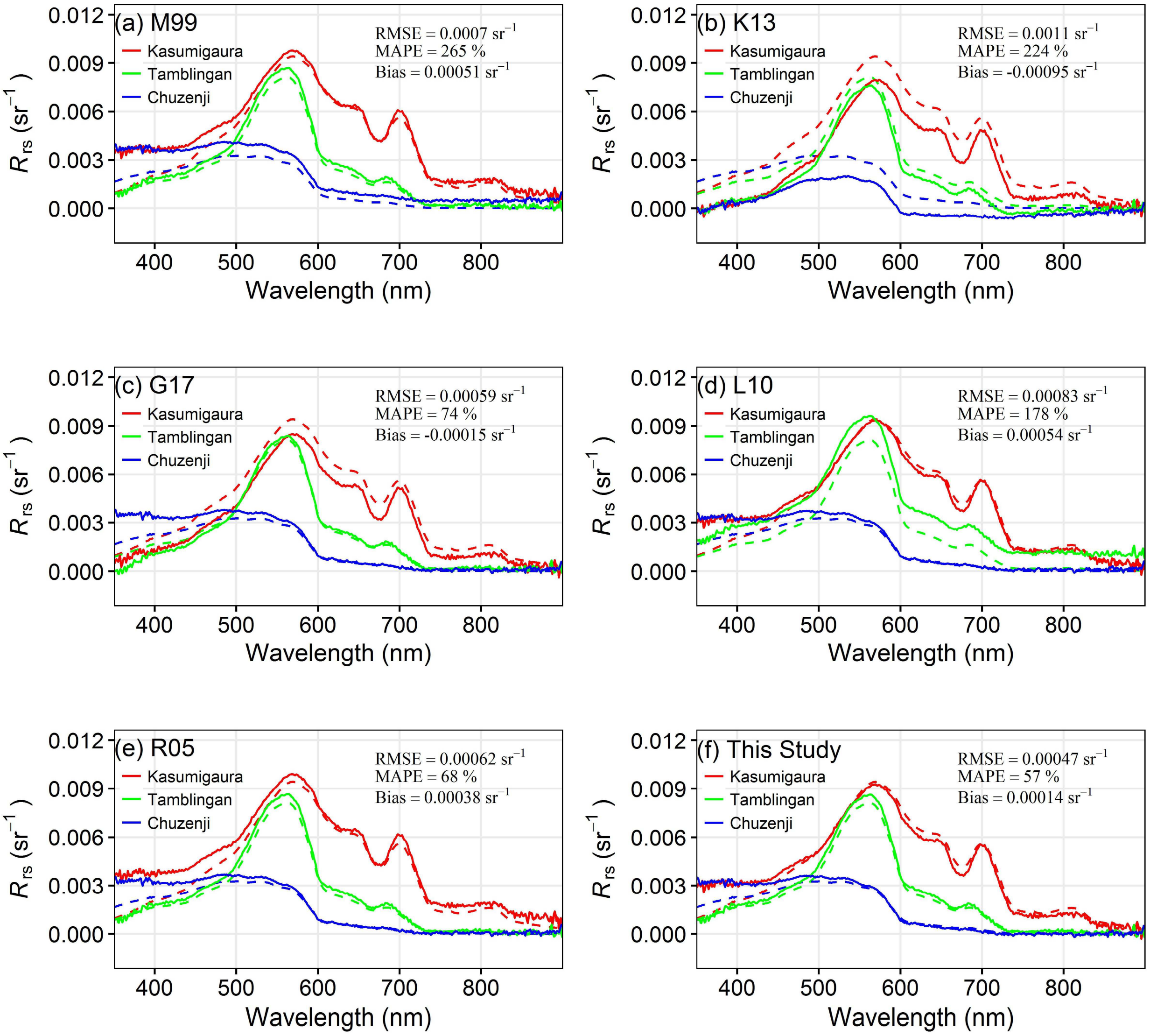

Figure 2.6. Comparison of above-water R_{rs} measurements corrected by different methods (solid lines) and corresponding *in situ*-measured Δ-free R_{rs} spectra (dashed lines) in two Japanese lakes (Lake Kasumigaura with Z_{SD}=0.8 m, and Lake Chuzenji with Z_{SD}=9.7 m) and one Indonesian lake (Lake Tamblingan with Z_{SD}=2.1 m). (a) using the M99 method (without Δ correction); (b) using the K13 method; (c) using the G17 method; (d) using the L10 method; (e) using the R05 method; (f) using the new method proposed in this study.

2.3.2. Evaluation using simulated data

As it is really not easy to obtain a large number of *Δ*-free R_{rs} spectra from the field surveys, I also used synthetic data to further evaluate the performance of the new method. Figure 2.7 shows the comparisons of *Δ*-corrected R_{rs} spectra (blue lines) and the true R_{rs} spectrum (red line) using Synthetic Dataset II. It can be seen that the R_{rs} spectra estimated using the M99 method exhibited substantial variation at all wavelengths, even though they had the same IOPs (Figure 2.7a). This variation was reduced after *Δ* corrections were carried out (Figures 2.7b-7f). The method proposed in this study performed well at all wavelengths with the smallest RMSE (0.00044 sr^{-1}) and MAPE (6%), followed by the G17 method (RMSE=0.00059 sr^{-1}, MAPE=11%, overcorrections at shorter wavelengths), R05 method (RMSE=0.00066 sr^{-1}, MAPE=19%, overcorrections at both shorter and longer wavelengths), and L10 method (RMSE=0.00099 sr^{-1}, MAPE=20%, under corrections at all wavelengths). The K13 method overcorrected the *Δ* effects at all wavelengths with a large RMSE (0.0016 sr^{-1}) and MAPE (39%).

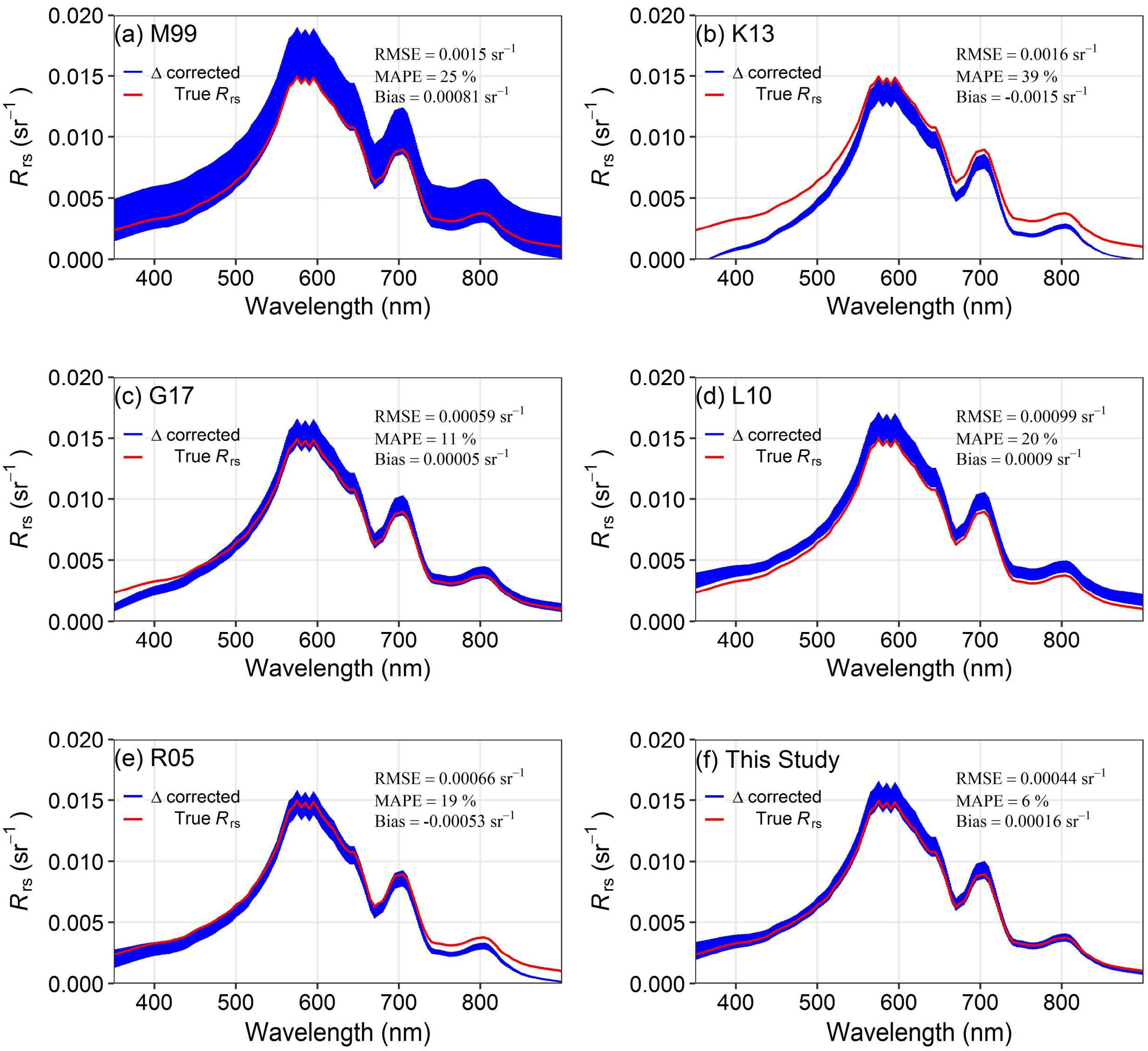

Figure 2.7. Comparison of Δ-corrected R_{rs} spectra (blue lines) and the true R_{rs} spectrum (red line) using Synthetic Dataset II. (a) R_{rs} spectra calculated using the M99 method (without Δ correction); (b) R_{rs} spectra corrected using the K13 method; (c) R_{rs} spectra corrected using the G17 method; (d) R_{rs} spectra corrected using the L10 method; (e) R_{rs} spectra corrected using the R05 method; (f) R_{rs} spectra corrected using the new method proposed in this study.

Figure 2.8 shows the comparisons of the estimated and true Δ values. The estimated Δ values were obtained from Synthetic Dataset III using the method proposed in this study (Eq. (2.15)), the L10 method, and the R05 method, respectively. From the figure, it can be seen that: (1) both the L10 and R05 methods properly estimated *Δ* in clear waters (i.e., waters with $R_{rs}(720) \leq 0.0095$ sr^{-1}), but significantly overestimated *Δ* values in turbid waters (i.e., waters with $R_{rs}(720) > 0.0095$ sr^{-1}), with overall MAPE=161% and MAPE=213%, respectively (Figures 2.8a and 8b); (2) in contrast, the method proposed in this study estimated an accurate *Δ* in all water types with MAPE=5% (Figure 2.8c).

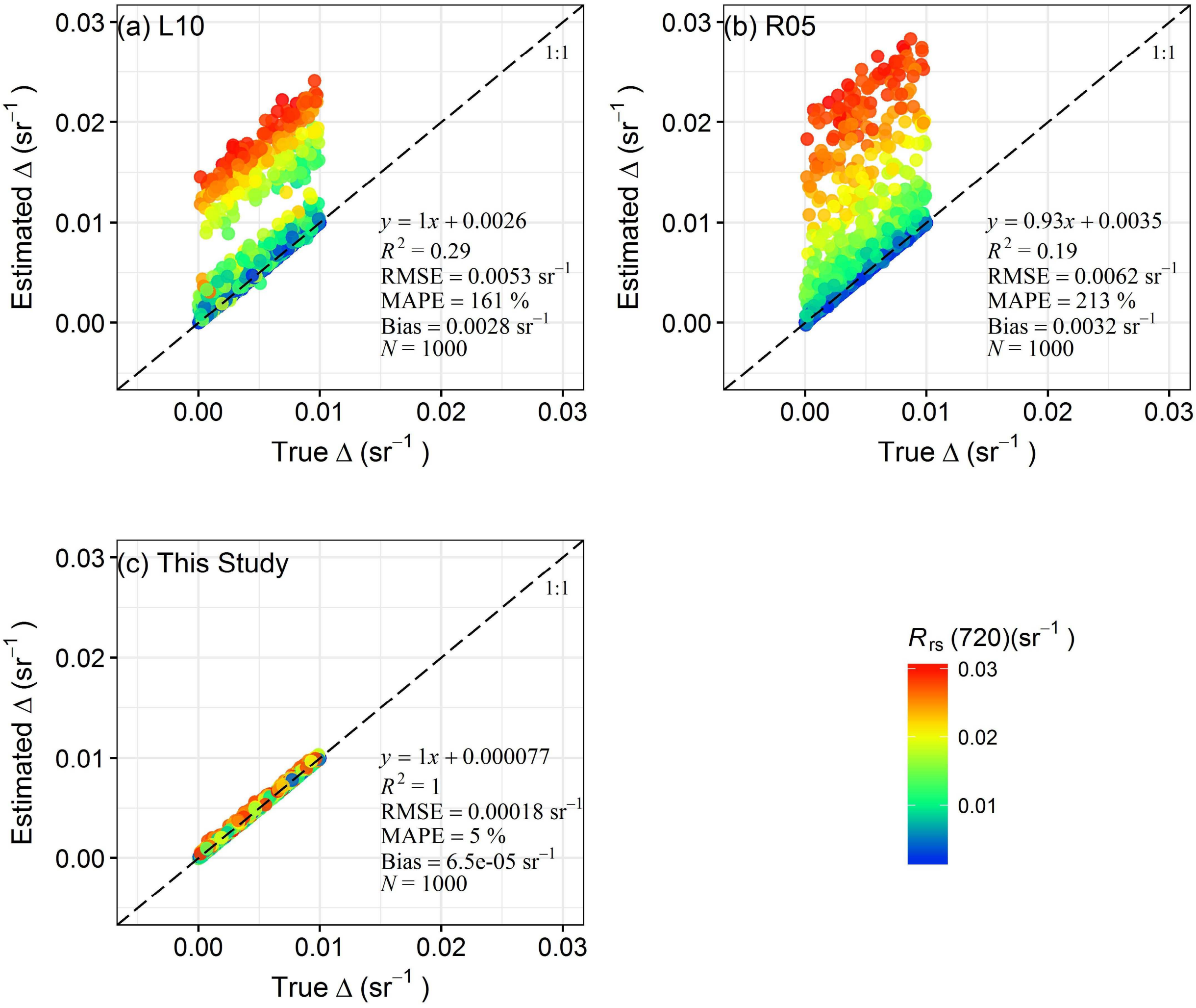

Figure 2.8. Comparison of estimated and true *Δ* values using Synthetic Dataset III. (a) Estimated *Δ* values using the L10 method; (b) estimated *Δ* values using the R05 method; (c) estimated *Δ*

using the method proposed in this study.

2.3.3. Comparison of spectral quality before and after *Δ* correction

I further compared the QA scores of the R_{rs} spectra before and after the *Δ* corrections for the data collected from the SeaBASS database and from Japanese inland waters, respectively (Figure 2.9). For the SeaBASS data, 75% of the R_{rs} spectra had QA scores higher than 8/9 even without *Δ* correction because some R_{rs} spectra had already been corrected by the data providers (M99 in Figure 2.9a). Nevertheless, the proportion of QA scores higher than 8/9 increased to 80% after the *Δ* effects was corrected by the new method (this study in Figure 2.9a). In contrast, the other two methods showed slightly decreased quality of the R_{rs} spectra after the *Δ* corrections (L10 and R05 in Figure 2.9a).

For Japanese inland waters, only 53% of the R_{rs} spectra had QA scores higher than 8/9 before the *Δ* corrections were carried out (M99 in Figure 2.9b). After the *Δ* corrections were carried out using the new method, the proportion of QA scores higher than 8/9 increased to 66%, and the proportion of R_{rs} spectra with lower QA scores decreased greatly (this study in Figure 2.9b). The other *Δ* correction methods (except for K13) also improved the quality of the R_{rs} spectra, but not as much as the new method (G17, L10, and R05 in Figure 2.9b).

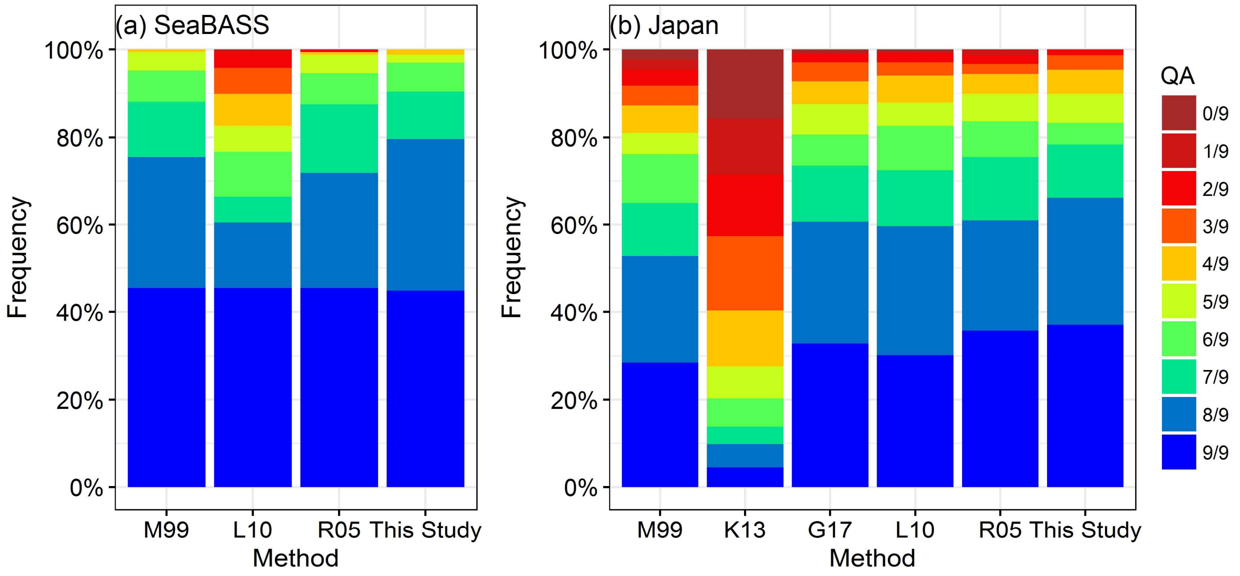

Figure 2.9. Comparisons of QA scores of R_{rs} spectra before (M99) and after (K13, G17, L10, R05, and the new method proposed in this study) $\mathit{\Delta}$ corrections. (a) Using R_{rs} spectra collected from the SeaBASS database (N=167); (b) using R_{rs} spectra collected from 21 Japanese inland waters (N=305).

I also separated the R_{rs} spectra collected from 21 Japanese inland waters into different sky condition groups using the method proposed by Groetsch et al. (2017) and compared their QA scores before and after the $\mathit{\Delta}$ corrections for each group (Figure 2.10). For the clear sky group (241 R_{rs} spectra), 59% of the R_{rs} spectra had QA scores higher than 8/9 before the $\mathit{\Delta}$ corrections were carried out, and the proportion was increased to 67%, 65%, 61%, and 61% by the new method, R05 method, G17 method, and L10 method, respectively. The K13 method reduced the QA scores even compared to the M99 method (i.e., without $\mathit{\Delta}$ corrections) because CDOM-rich samples were lacking in this study (top panel in Figure 2.10).

For the scattered cloud (43 R_{rs} spectra) and overcast (21 R_{rs} spectra) sky groups, the Δ correction methods greatly improved the R_{rs} spectra quality (middle and bottom panels in Figure 2.10). For example, only 35% and 24% of R_{rs} spectra had QA scores higher than 8/9 in the scattered cloud and overcast sky condition groups, respectively, before Δ corrections were carried out, and the proportions increased to 63% and 62% after the Δ corrections were carried out using the new method. In particular, under the overcast sky condition, there were no R_{rs} spectra with QA scores smaller than 4/9 after the Δ corrections were made using the new method (bottom panels in Figure 2.10). Except for the K13 method, the other Δ correction methods also certainly improved the R_{rs} spectra quality, with proportions of R_{rs} spectra with QA scores higher than 8/9 of 56% (scattered cloud) and 57% (overcast) for the L10 method, 56% (scattered cloud) and 62% (overcast) for the G17 method, and 47% (scattered cloud) and 48% (overcast) for the R05 method.

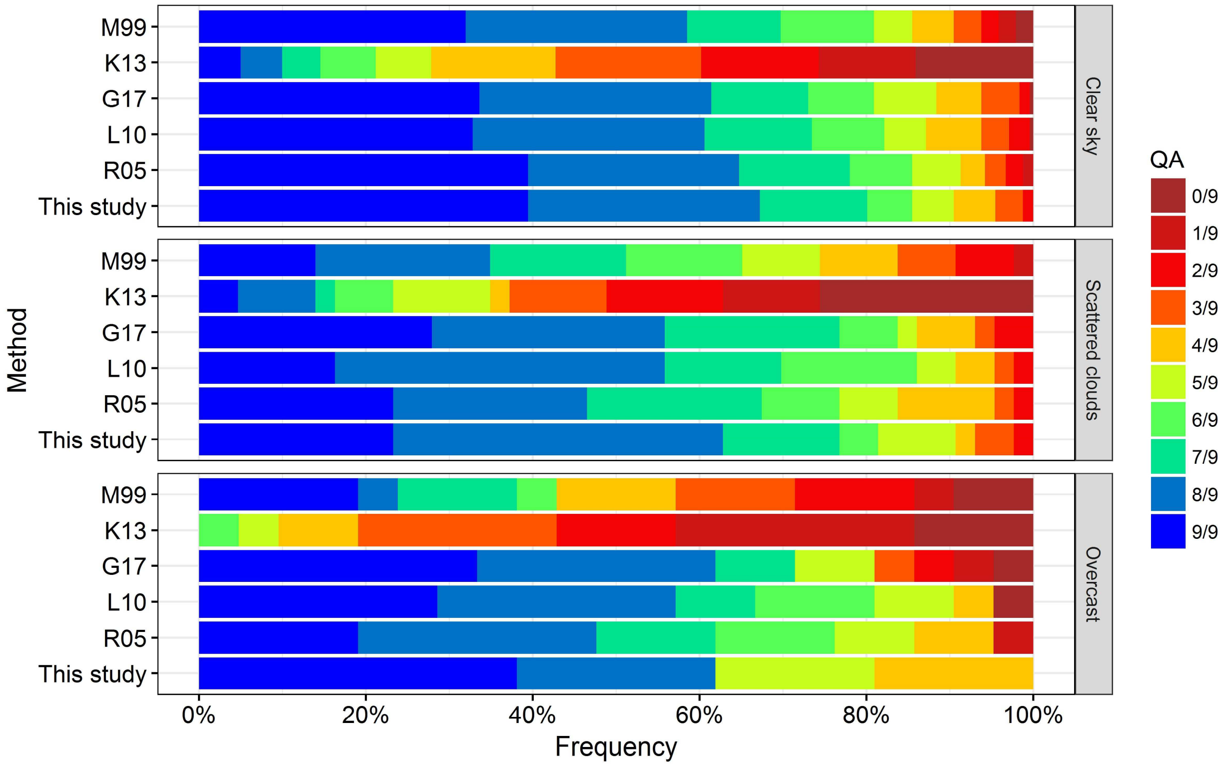

Figure 2.10. Comparison of QA scores of R_{rs} spectra before (M99) and after (K13, G17, L10, R05, and the new method proposed in this study) Δ corrections under different sky conditions. Top: under a clear sky condition; middle: under a scattered clouds condition; bottom: under an overcast sky condition.

2.4. Discussion

2.4.1. Applicability of the proposed method

In this study, I proposed a new method for estimating Δ effects, which are always contained in R_{rs} spectra measured in a field survey using the above-water approach (Ruddick et al., 2005; Lee et al., 2010; Kutser et al., 2013; Groetsch et al., 2017). The key point of the new method is to construct a relationship between RHW and Δ-free Median[$R_{rs}(750)$, $R_{rs}(780)$] using a synthetic dataset. There are two advantages for using this relationship. First, users do not need to consider Δ effects when they apply the relationship. This is because the RHW is used as an independent variable in the relationship. The RHW is a kind of baseline-based index, which can cancel noise coming from the environment such as Δ effects or errors due to imperfect atmospheric correction (Gower, 1980; Gower et al., 2005; Hu, 2009; Hu et al., 2012; Matsushita et al., 2016). Therefore, almost the same RHW values can be obtained even using R_{rs} spectra before Δ corrections (e.g., R_{rs} spectra from Eq. (1.4)). The first advantage can be directly confirmed from the results in Figures 2.6f, 2.7f and 2.8c, which indicate that the new method can retrieve accurate Δ values from contaminated R_{rs} spectra (i.e., R_{rs} spectra with Δ effects).

The second advantage is that the relationship can be applied to various waters without requiring any recalibration. This is mainly because I selected three near-infrared wavelengths to calculate RHW. It has been widely known that SIOPs in the near-infrared domain are dominant only because of the absorption coefficient of pure water (Babin and Stramski, 2002; Ruddick et al., 2006; Babin et al., 2003). Therefore, it can be considered that the constructed relationship can be applied to other waters even though I only used SIOPs of Lake Kasumigaura, Japan to generate the synthetic dataset for calibrating Eq. (2.15). In addition, I set wide ranges of concentrations of Chl-a (0.01-300 mg/m^3) and tripton (0.01-300 g/m^3) and set the CDOM absorption coefficient at 440 nm (0.01-10 m^{-1}). These simulation ranges can cover most of the water types in the world (Moore et al., 2014).

The second advantage can be confirmed from the results shown in Figure 2.7f, as I just used the default SIOPs provided by Hydrolight, which are totally different from the SIOPs used for obtaining Eq. (2.15). In addition, the results shown in Figure 2.6f can also confirmed the proposed method does not depend on the used SIOPs because the SIOPs of Lake Chuzenji and Lake Tamblingan are probably different from those of Lake Kasumigaura. This advantage overcame the shortcomings of L10 and G17, which require SIOPs to model an R_{rs} spectrum for optimization procedure (Figures 2.6c, 2.6d, 2.7c, and 2.7d).

In addition, the use of a non-linear relationship can overcome the shortcomings of R05, which failed in extreme turbid water ($R_{\mathrm{rs}}(720) > 0.0095\ \mathrm{sr}^{-1}$) due to the fact that saturation effects on the R_{rs} spectra induce a ratio of $R_{\mathrm{rs}}(720)/R_{\mathrm{rs}}(780)$ much smaller than the constant ratio of 2.35 used in Ruddick et al. (2005). For example, the ratios of $R_{\mathrm{rs}}(720)/R_{\mathrm{rs}}(780)$ in Synthetic Datasets II and III varied from 1.99 to 2.03 (average of 2.01) and from 1.18 to 3.11 (average of 2.15), respectively.

2.4.2. Assumption of a spectral independent for Δ

In the present study, I assumed that Δ is a spectral independent parameter because its spectral shape is complicated and there is still no clear theory to describe this spectral variation (Lee et al., 2010). In addition, Craig et al. (2006) reported that uncertainties in R_{rs} spectra almost all come from changed amplitudes of the spectra rather than changed spectral shapes. However, Groetsch et al. (2017) reported that the Δ effect should be a spectrally dependent parameter. Nevertheless, their results showed that the spectral shapes of water surface-reflected skylight ($\rho \cdot L_s/E_d$) are almost flat under scattered clouds and overcast sky conditions, but change substantially at shorter wavelengths (350–450 nm) under clear sky conditions (Figure 5 in Groetsch et al., 2017). It should be noted that the wavelength dependence of $\rho \cdot L_s/E_d$ has been partly addressed in Eq. (1.4), and thus the spectral variation of the remaining part (Δ effects) can be considered to be small and negligible. Therefore, assuming a spectrally independent Δ is probably reasonable.

The validity of assuming spectral independence for Δ effects can also be confirmed by our results. For example, the simulation results shown in Figure 2.7f indicate that the assumption is probably reasonable. Nevertheless, care should be taken when using an R_{rs} spectrum at a wavelength shorter than 450 nm because the inconsistencies were sometimes found at these shorter wavelengths (red lines and blue lines in Figure 2.6f).

2.4.3. Significance of Δ correction

In situ R_{rs} spectra are very important for the development of water quality-retrieval algorithms and the evaluation of atmospheric-correction algorithms. Water quality-retrieval algorithms developed based on inaccurate *in situ* R_{rs} spectra (e.g., containing Δ effects) will lead to erroneous model coefficients and will have limited applicability (Kutser et al., 2013; Wei et al., 2016; Zibordi et al., 2012). In addition, atmospheric correction is a key procedure for ocean color remote sensing, and *in situ* R_{rs} spectra are usually used to evaluate the performance of an atmospheric correction algorithm. Using inaccurate *in situ* R_{rs} spectra for the evaluation might influence the judgment and thus lead to an incorrect conclusion.

The results shown in Figure 2.7 and Figure 2.10 indicate another significant advantage of Δ

correction. From the figures, it can be seen that the proposed method can correct R_{rs} spectra collected under all sky conditions and improve their quality. This finding indicates that *in situ* R_{rs} spectra will become usable even if they are collected under scattered clouds or overcast sky conditions. This property will relax the restriction that *in situ* spectrum measurement should be carried out under a clear sky, and thus can increase the number of usable *in situ* R_{rs} spectra in the future. Moreover, wind speed data, which are often not available in field surveys, will not be necessary to estimate a more appropriate ρ value in Eq. (1.4).

2.5. Conclusions

In this chapter, I proposed a new method for removing the residual reflected skylight (i.e., Δ corrections) in above-water remote sensing reflectance measurements. The proposed method is simple, effective, and universally applicable without requiring any recalibration. It can correct an *in situ* R_{rs} spectrum measured under various sky conditions (clear, scattered clouds, or overcast). It is strongly recommend that the Δ corrections be carried out for all R_{rs} spectra measured using the above-water approach before they are applied to the development of water quality algorithms or the evaluation of atmospheric correction algorithms.

Chapter III An Improved Algorithm for Estimating the Water Transparency from Remote Sensing Data Based on the New Underwater Visibility Theory

3.1. Introduction

There are three requirements of applying the Lee15 Z_{SD} algorithm: (1) accurate measurements of R_{rs}; (2) accurate estimations of K_d; and (3) the proper values of K_T/K_d ratios. The problem of R_{rs} has been addressed in chapter II. In this chapter, the objectives are to (1)improve the Lee15 algorithm by integrating different types of QAAs to estimate more accurate K_d and proposing a new algorithm to calculate more accurate K_T/K_d ratios; and (2) evaluate the performance of the improved Z_{SD} algorithm using *in situ* data collected from Japanese waters and SeaBASS dataset.

3.2. Methods

3.2.1. Data collection

The study area of this research included 21 waters in Japan and coastal waters in United States (Figure 2.1). The 21 Japanese inland waters include 20 lakes and 1 bay (Tokyo Bay; Figure 2.1a), with Z_{SD} values ranging from 0.3 m to 16.4 m, chlorophyll-a (Chl-a) concentrations ranging from 0.5 mg/m^3 to 187.7 mg/m^3, and total suspended solids (TSS) concentrations ranging from 0.4 g/m^3 to 73.7 g/m^3 (Table 2.1).

Field surveys were carried out in the 21 above-described Japanese waters during 2009–2019. Data were collected from a total of 305 sampling sites. For each site, the Z_{SD} was measured by vertically lowering down a 30-cm-dia. white disk into the water until the disk was no longer visible (or lower a Secchi disk out of sight and then raise the disk until it becomes visible). At the same time, the radiance of skylight (L_{s}), the radiance from a standard board (L_{g}), and the total upwelling radiance from the water (L_{t}) were measured using a FieldSpec® HandHeld spectroradiometer (ASD Inc., Bloulder, CO, USA) between the local time 9:00 to 16:00 (6 measurements between 8:10 and 9:00), with the sensor zenith angle of 40° and azimuth angle of 135° from the sun.

Remote sensing reflectance (R_{rs}) was then calculated using Eq. (1.5) with the skylight reflectance $\rho = 0.028$ (when the wind speed was < 5 m/s, Mobley, 1999). Δ is the contribution of the residual reflected skylight, which was calculated using the proposed method in chapter II (Figure 3.1a). For the R_{rs} spectra obtained from SeaBASS, I also processed them using the proposed method in chapter II (Figure 3.1b). All R_{rs} spectra were then converted to MERIS bands based on the MERIS Spectral Response Functions.

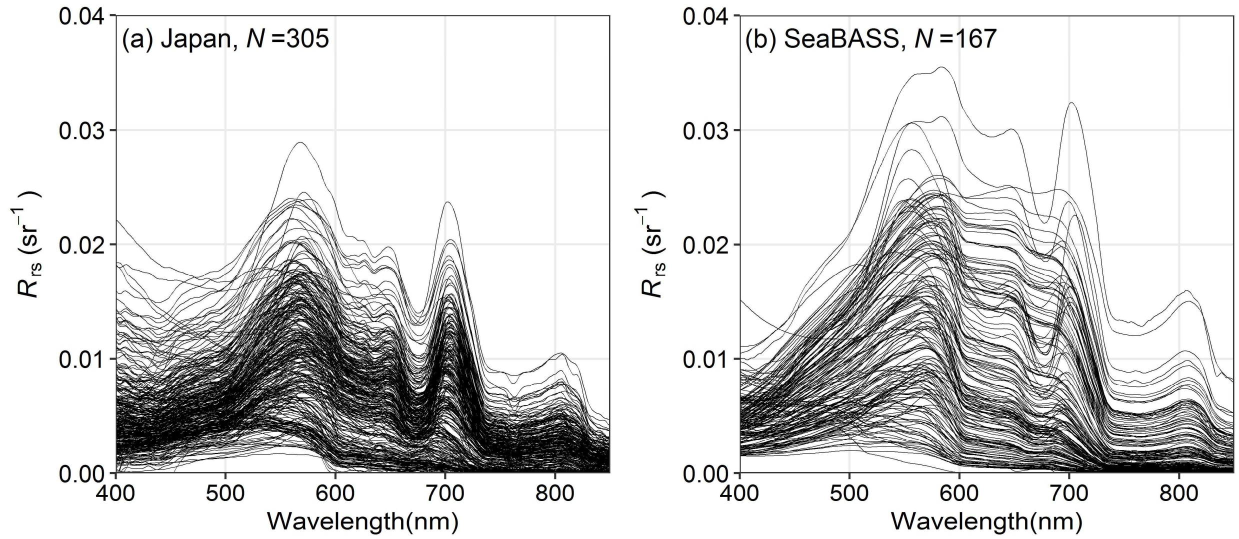

Figure 3.1. R_{rs} spectra used in this study. (a) 305 R_{rs} spectra collected from 21 waters in Japan. (b) 167 R_{rs} spectra collected from SeaBASS.

For 21 Japanese waters, water samples were collected and kept in ice boxes, and taken to the laboratory immediately after finishing the collection. The absorption coefficients of phytoplankton ($a_{\mathrm{ph}}(\lambda)$), tripton ($a_{\mathrm{tr}}(\lambda)$) and CDOM ($a_{\mathrm{CDOM}}(\lambda)$) were measured following the NASA protocols (Mitchell et al., 2002). The total absorption coefficient $a(\lambda)$ was calculated as the sum of $a_{\mathrm{ph}}(\lambda)$, $a_{\mathrm{tr}}(\lambda)$, $a_{\mathrm{CDOM}}(\lambda)$, and the absorption coefficient of pure water, i.e., $a_{\mathrm{w}}(\lambda)$. The values of $a_{\mathrm{w}}(\lambda)$ were taken from Lee et al. (2015b), Pope and Fry (1997), and Kou et al. (1993). In total, $a(\lambda)$ values at 76 sites from Lakes Kasumigaura, Suwa, Hibara, Shirakaba, Kugushi, Suigetsu, Suga, Mikata, Megami, Tateshina and Senbako were collected.

In several Japanese lakes (Lakes Biwa, Kasumigaura, Shirakaba, Suwa, Hibara, Shirakaba, Megami, Tateshina, Senbako, Unagi and Sai), the downward irradiance (E_{d}) at different depths of the water column was also measured (before 2018, a Multispectral Radiometer (Satlantic, Halifax, Canada) with available bands of 443 nm, 555 nm, and 669 nm was used; after 2018, a RAMSES spectroradiometer (TriOS, Rastede, Germany) with available bands of 320-950 nm was used). These data were used to obtain the measured K_d and then compared with R_{rs}-derived K_d at MERIS visible bands. In total, the measured K_d values at 90 sites were collected.

3.2.2. Model development

I carried out two improvements for the original Lee15 algorithm. First, by considering the shortcoming of QAA_v6 in turbid waters, I proposed the use of another QAA, which was specifically developed for turbid inland waters by Yang et al. (2013), to estimate $a(\lambda)$ and $b_b(\lambda)$ in this type of waters (hereafter referred to as the 'QAA_T'). I selected the QAA_T algorithm in this study because all of the equations in the QAA_T are semi-analytical or analytical equations without any *in situ* data used for recalibration (Yang et al., 2013).

For clear waters, I still used QAA_v5 because of its good performance in this type of waters (Lee et al., 2002; Fukushima et al., 2016). I adapted the maximum chlorophyll-a index (MCI) originally developed by Gower et al. (2005) for switching the QAA_v5 and QAA_T. The modified MCI is defined as (Matsushita et al., 2015):

$$\mathrm{MCI} = R_{\mathrm{rs}}(709) - R_{\mathrm{rs}}(665) - \left[\frac{(709-665)}{(754-665)}\left(R_{\mathrm{rs}}(754) - R_{\mathrm{rs}}(665)\right)\right], \tag{3.1}$$

where $R_{\mathrm{rs}}(665)$, $R_{\mathrm{rs}}(709)$ and $R_{\mathrm{rs}}(754)$ are the remote sensing reflectance at 665 nm, 709 nm and 754 nm, respectively. According to Matsushita et al. (2015), MCI = 0.001 sr^{-1} was used to distinguish clear and turbid waters. I named this blended QAA as 'QAA_hybrid', and its main steps are summarized in Table 3.1.

Table 3.1. Main steps of the QAA_hybrid

Step	Property	Derivation	
1	$r_{\mathrm{rs}}(\lambda)$	$r_{\mathrm{rs}}(\lambda)=R_{\mathrm{rs}}(\lambda)/\left(0.52+1.7R_{\mathrm{rs}}(\lambda)\right)$	
2	$u(\lambda)$	$u(\lambda)=\dfrac{-0.089+\sqrt{0.089^2+4\times 0.125r_{\mathrm{rs}}(\lambda)}}{2\times 0.125}$	
3	MCI	$\mathrm{MCI}\leq 0.001\ \mathrm{sr}^{-1}$ (QAA_v5)	$\mathrm{MCI}>0.001\ \mathrm{sr}^{-1}$ (QAA_T)
4	$a(\lambda_0)$	$x=\log\left(\dfrac{r_{\mathrm{rs}}(443)+r_{\mathrm{rs}}(490)}{r_{\mathrm{rs}}(560)+5\frac{r_{\mathrm{rs}}(670)}{r_{\mathrm{rs}}(490)}r_{\mathrm{rs}}(670)}\right)$ $a(560)=a_{\mathrm{w}}(560)+10^{-1.146-1.366x-0.469x^2}$	$a(754)=a_{\mathrm{w}}(754)$
5	$b_{\mathrm{bp}}(\lambda_0)$	$b_{\mathrm{bp}}(560)=\dfrac{u(560)\times a(560)}{1-u(560)}-b_{\mathrm{bw}}(560)$	$b_{bp}(754)=\dfrac{u(754)\times a(754)}{1-u(754)}-b_{\mathrm{bw}}(754)$
6	$b_{\mathrm{bp}}(\lambda)$	$Y=2.0\left(1-1.2\exp\left(-0.9\dfrac{r_{\mathrm{rs}}(443)}{r_{\mathrm{rs}}(560)}\right)\right)$ $b_{\mathrm{bp}}(\lambda)=b_{\mathrm{bp}}(560)\left(\dfrac{560}{\lambda}\right)^{Y}$	$Y=-372.99\beta^2+37.286\beta+0.84$ $\beta=\log[u(754)/u(779)]$ $b_{\mathrm{bp}}(\lambda)=b_{\mathrm{bp}}(754)\left(\dfrac{754}{\lambda}\right)^{Y}$
7	$a(\lambda)$	$a(\lambda)=\left(1-u(\lambda)\right)\left(b_{bw}(\lambda)+b_{bp}(\lambda)\right)/u(\lambda)$	

My second improvement for the Lee15 algorithm was to develop another algorithm for estimating a more realistic ratio of K_{T} and K_{d} in various waters. According to previous studies, the subsurface remote sensing reflectance (r_{rs}) at optically shallow waters can be expressed as follows (Philpot, 1989; Maritorena et al., 1994; Lee et al., 1998):

$$r_{\mathrm{rs}}\approx r_{\mathrm{rs}}^{\mathrm{dp}}\{1-A_0\exp[-(K_{\mathrm{d}}+K_{\mathrm{u}}^{\mathrm{C}})H]\}+A_1\rho_{\mathrm{B}}\exp[-(K_{\mathrm{d}}+K_{\mathrm{u}}^{\mathrm{B}})H], \tag{3.2}$$

where $r_{\mathrm{rs}}^{\mathrm{dp}}$ is the r_{rs} for optically deep waters, A_0 is 1.0, and A_1 is $1/\pi$ for a lambertian bottom, $K_{\mathrm{u}}^{\mathrm{C}}$ is the diffuse attenuation coefficient of upwelling radiance from the water column scattering, $K_{\mathrm{u}}^{\mathrm{B}}$ is the diffuse attenuation coefficient of upwelling radiance from the bottom, ρ_{B} is the bottom reflectance, and H is the bottom depth. The first term on the right side of the equation refers to the reflectance from the water column, and the second term on the right refers to the reflectance from the bottom. According to Lee et al. (1999) and Barnes et al. (2018), K_d and K_u^B can be estimated using the following equations:

$$K_\mathrm{d} = D_\mathrm{d}\alpha \approx [1/\cos(\theta_\mathrm{w})]\alpha \tag{3.3}$$

$$K_\mathrm{u}^\mathrm{B} = D_\mathrm{u}^\mathrm{B}\alpha \approx [1.04(1+5.4u)^{0.5}]\alpha, \tag{3.4}$$

where θ_w is the subsurface solar zenith angle, α is defined as $(a + b_\mathrm{b})$, and u is defined as $b_\mathrm{b}/(a + b_\mathrm{b})$. If the bottom of the water is treated as the Secchi disk, and assume that the disk is a lambertian object, then the second term on the right side of Eq. (3.2) becomes the light that comes from the Secchi disk. Therefore, the K_u^B can be considered to be the K_T in the new Z_SD theory (i.e., $K_\mathrm{T} = K_\mathrm{u}^\mathrm{B}$). By converting the subsurface solar zenith angle θ_w to the above surface solar zenith angle θ, and combining the Eqs. (3.3) and (3.4), the ratio of K_T and K_d can be expressed as:

$$K_\mathrm{T}/K_\mathrm{d} = \frac{1.04(1+5.4u)^{0.5}}{1/\left(1-\frac{\sin(\theta)^2}{n^2}\right)^{0.5}}\ , \tag{3.5}$$

where n is the refractive index value of the water (1.34, Lee et al., 1998). By replacing the fixed value of 2.5 in Eq. (1.3) with $(1+K_\mathrm{T}/K_\mathrm{d})$, the Lee15 algorithm can be modified as:

$$Z_\mathrm{SD} = \frac{1}{(1+K_\mathrm{T}/K_\mathrm{d})\cdot\mathrm{Min}(K_\mathrm{d})}\ln\left(\frac{|0.14-R_\mathrm{rs}^\mathrm{PC}|}{C_\mathrm{t}^\mathrm{r}}\right), \tag{3.6}$$

It should be noted that the wavelength with minimum K_d value at visible bands should be used to calculate the $K_\mathrm{T}/K_\mathrm{d}$ ratio in Eq. (3.5).

3.2.3. Accuracy assessment

I used the root mean square error (RMSE), the mean absolute percentage error (MAPE), and bias to evaluate the performance of the improved Z_{SD} algorithm. The equations are as follows:

$$\mathrm{RMSE} = \sqrt{\frac{\sum_{i=1}^{N}\left(X_{\mathrm{estimated},i}-X_{\mathrm{measured},i}\right)^2}{N}} \tag{3.7}$$

$$\mathrm{MAPE} = \frac{1}{N}\sum_{i=1}^{N}\left|\frac{X_{\mathrm{estimated},i}-X_{\mathrm{measured},i}}{X_{\mathrm{measured},i}}\right| \cdot 100\% \tag{3.8}$$

$$\mathrm{Bias} = \frac{1}{N}\sum_{i=1}^{N}\left(X_{\mathrm{estimated},i} - X_{\mathrm{measured},i}\right), \tag{3.9}$$

where $X_{\mathrm{estimated}}$ is the estimated parameter (e.g., a, K_{d} or Z_{SD}), X_{measured} is the corresponding *in situ* measurement, and N is the number of data. The determination coefficient (R^2) was also calculated for reference.

3.3. Results

3.3.1. Validation of *a*

Figure 3.2 shows the results of comparisons of the derived $a(\lambda)$ and *in situ* $a(\lambda)$ at all MERIS visible bands. It can be seen that the QAA_v6 gave larger underestimations of $a(\lambda)$ at all visible bands, with RMSE =1.5 m^{-1}, MAPE = 55% and Bias = −1.0 m^{-1} (Figure 3.2a). In contrast, the QAA_hybrid showed better retrievals of $a(\lambda)$ at all visible bands with RMSE = 0.78 m^{-1}, MAPE =24% and Bias = −0.35 m^{-1} (Figure 3.2b). The determination coefficient was also increased from 0.61 to 0.74. However, some retrieved absorption coefficients at 443 nm still showed slight underestimations.

I checked the bands corresponding to the minimum K_{d} and found that 443 nm was not selected for Z_{SD} estimations. If I compare only the retrieved $a(\lambda)$ and the *in situ* $a(\lambda)$ at the selected bands (i.e., the band with minimum K_{d} in visible domain and finally used for Z_{SD} estimations), no obvious underestimations or overestimations from the use of QAA_hybrid were observed (Figure 3.2d), whereas the QAA_v6 still showed larger underestimated $a(\lambda)$ at the selected bands (Figure 3.2c). The values of RMSE, MAPE, Bias, and R^2 were calculated as 0.23 m^{-1}, 22%, −0.11 m^{-1}, and 0.71, respectively, with the use of the QAA_hybrid at the selected bands.

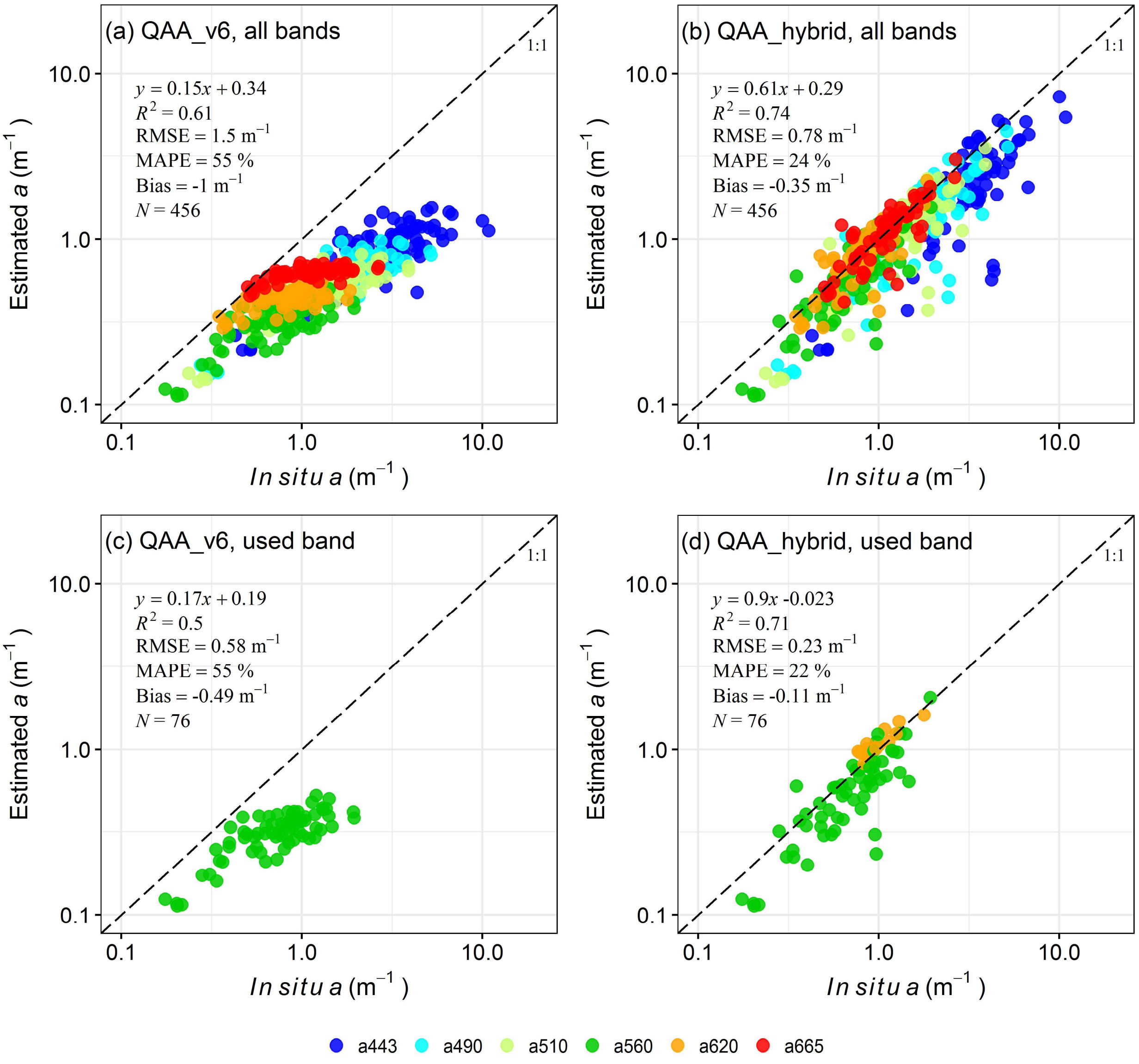

Figure 3.2. Comparison between *in situ* absorption coefficients and estimated absorption coefficients, estimated using (a) QAA_v6 at all MERIS visible bands, (b) QAA_hybrid at all MERIS visible bands, (c) QAA_v6 only at the bands corresponding to the minimum K_d values,

and (d) the QAA_hybrid only at the bands corresponding to the minimum K_d values.

3.3.2. Validation of K_d

Figure 3.3 illustrates the results of comparisons of the retrieved K_d and the *in situ*-measured K_d at all MERIS visible bands. It can be seen that using $a(\lambda)$ and $b_b(\lambda)$ estimated from the QAA_v6 resulted in large underestimations of K_d (RMSE = 2.1 m^{-1}, MAPE = 52% and Bias = −1.5 m^{-1}, Figure 3.3a), and these underestimations were largely improved by using the QAA_hybrid instead of QAA_v6 (RMSE = 0.76 m^{-1}, MAPE = 23% and Bias = −0.4 m^{-1}, Figure 3.3b). I also compared only the K_d at the bands finally used for the Z_{SD} estimations (i.e., the minimum K_d) and the corresponding *in situ*-measured K_d, similar improvements were found by comparing the use of $a(\lambda)$ and $b_b(\lambda)$ obtained from QAA_v6 with those obtained using the QAA_hybrid (Figure 3.3c, d). It should be noted that the smaller numbers of data in Figure 3.3c and Figure 3.3d are because the estimated minimum K_d values were found at wavelengths without *in situ* measurements for some sampling sites.

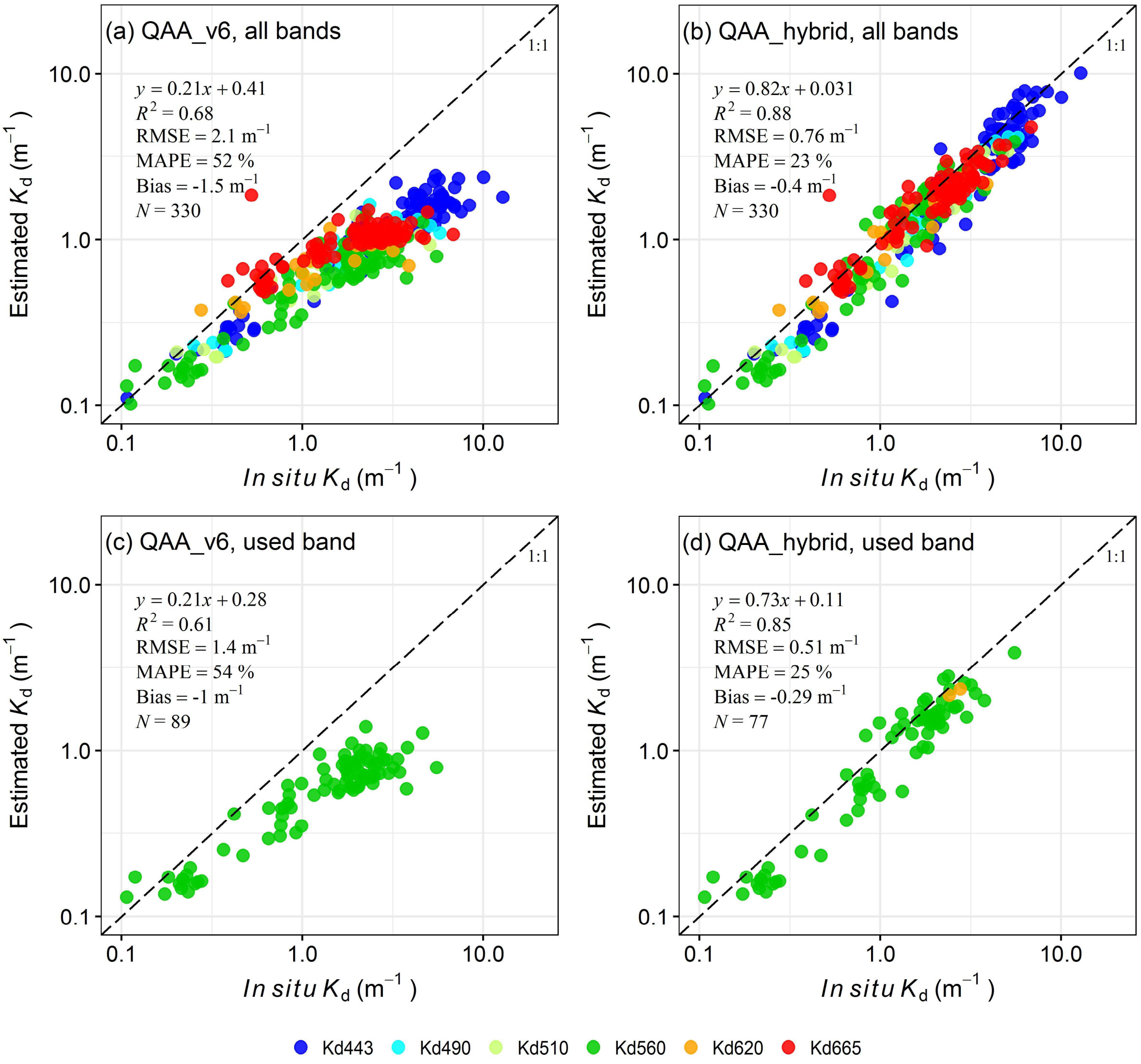

Figure 3.3. Comparison between *in situ*-measured K_d and estimated K_d at visible bands. (a) Estimated $K_d(\lambda)$ using $a(\lambda)$ and $b_b(\lambda)$ from QAA_v6. (b) Estimated $K_d(\lambda)$ using $a(\lambda)$ and $b_b(\lambda)$ from the QAA_hybrid. (c) Only the estimated K_d at the minimum K_d bands using $a(\lambda)$ and $b_b(\lambda)$ from QAA_v6. (d) Only the estimated K_d at the minimum K_d bands using $a(\lambda)$ and $b_b(\lambda)$ from the QAA_hybrid.

3.3.3. Estimated K_T/K_d

Figure 3.4 shows the estimated K_T/K_d ratios obtained using Eq. (3.5) for all available data (*N*=472). The results showed that the K_T/K_d ratios ranged from 0.85 to 1.70 with an average value of 1.28. These ratios were different from the fixed value of 1.5 used in the original Lee15 algorithm. In addition, the K_T/K_d ratios of clear waters (i.e., Z_{SD} values ≥ 2 m) were significantly lower than those of turbid waters (i.e., Z_{SD} values < 2 m), with a mean K_T/K_d ratio of 1.14 in clear waters and 1.35 in turbid waters ($p < 0.001$).

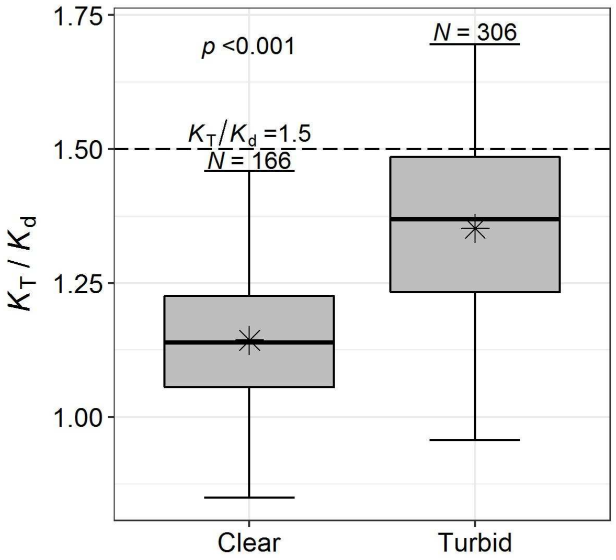

Figure 3.4. Comparison of estimated K_T/K_d values between clear (Z_{SD} values ≥2 m) and turbid (Z_{SD} values <2 m) waters. *Black star:* The mean K_T/K_d ratio. *Dashed line:* K_T/K_d=1.5, which was used in the original Lee15 algorithm.

3.3.4. Validation of Z_{SD}

Figure 3.5 shows the results of comparisons of the estimated and *in situ*-measured Z_{SD} values. The results showed that: (1) the original Lee15 algorithm clearly underestimated the Z_{SD} in clear waters (blue points) and overestimated the Z_{SD} in turbid waters (red points), with the RMSE of 2 m and MAPE of 54% (Figure 3.5a); (2) the overestimations in turbid waters were improved by using the QAA_hybrid instead of QAA_v6, with a reduced MAPE of 36% (Figure 3.5b; red points); (3) the underestimations in clear waters were much improved by using dynamic $K_{\mathrm{T}}/K_{\mathrm{d}}$ ratios instead of the constant ratio of 1.5, with decreased RMSE of 1.7 m (Figure 3.5c; blue points); and (4) both overestimations and underestimations were improved by combining the QAA_hybrid and dynamic $K_{\mathrm{T}}/K_{\mathrm{d}}$ ratios, with a reduced RMSE of 1.7 m and MAPE of 35% (Figure 3.5d). The slope and intercept values of the regression lines were also changed from 0.59 to 0.76 and from 0.89 to 0.51, respectively.

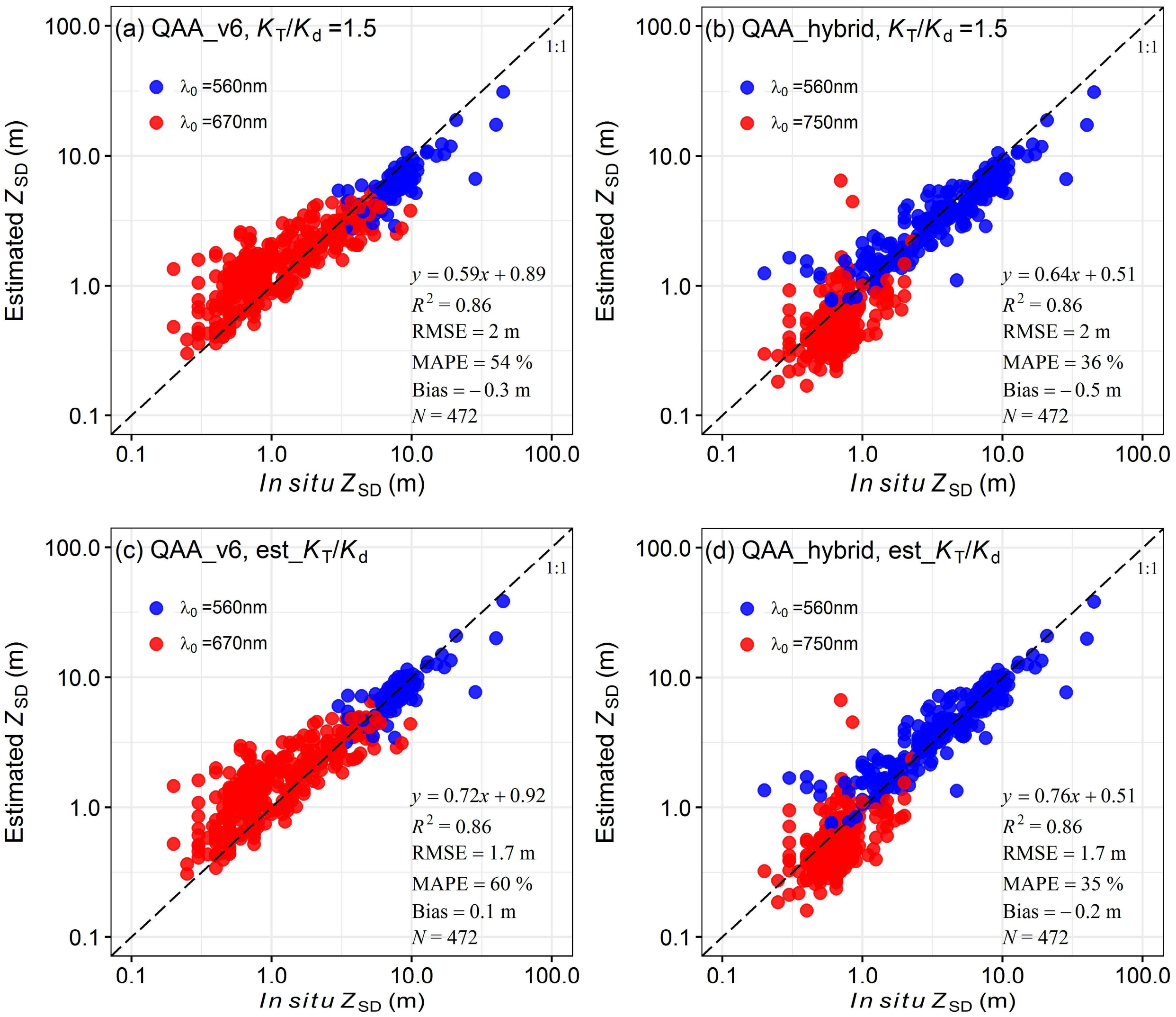

Figure 3.5. Comparisons between *in situ* measured Z_{SD} values and estimated Z_{SD} values from *in situ* R_{rs}. (a) Estimated Z_{SD} based on QAA_v6 with K_T/K_d=1.5 (i.e., original Lee15 algorithm). (b) Estimated Z_{SD} based on the QAA_hybrid but still with K_T/K_d=1.5. (c) Estimated Z_{SD} based on QAA_v6 but with dynamic K_T/K_d ratios (est_K_T/K_d). (d) Estimated Z_{SD} based on the QAA_hybrid with dynamic K_T/K_d ratios (i.e., the improved Lee15 algorithm). Blue points represent the Z_{SD} estimated using 560 nm as reference band in both QAA_v6 and QAA_hybrid (i.e., QAA_v5), and red points represent the Z_{SD} estimated using 670 nm as reference band in QAA_v6 and using 754 nm as reference band in QAA_hybrid (i.e., QAA_T).

3.4. Discussion

3.4.1. Necessity of the QAA_hybrid

The estimations of $a(\lambda)$ and $b_b(\lambda)$ using QAA_v6 is the first step in the original Lee15 algorithm (Lee et al., 2015a). Both previous studies and the results of this study have confirmed that the estimation errors that occur in this step will be propagated to the $K_d(\lambda)$ estimations in the second step and then the Z_{SD} estimations in the final step (Yang et al., 2014, 2015; Figures 3.2a, 3.3a, and 3.5a in this study). Failures of QAA_v6 applications usually occurred in turbid waters (Yang et al., 2014; Wang et al., 2017; Rodrigues et al., 2017). It is thus necessary to use an alternative to QAA_v6 for turbid waters.

Although several modified QAAs have been proposed for retrieving $a(\lambda)$ and $b_b(\lambda)$ values in turbid waters, two empirical relationships for estimating the absorption coefficient at a reference band ($a(\lambda_0)$, step 4 in Table 3.1) and the spectral slope of the backscattering coefficient of suspended particles (Y, step 6 in Table 3.1) must be recalibrated by using *in situ* data in most of these modified QAAs (Le et al., 2009; Huang et al., 2014; Mishra et al., 2014; Wang et al., 2017). The constant requirement of *in situ* data for model recalibration will make the two empirical relationships the first important equations in these modified QAAs, and thus will limit their applicability in various waters. In contrast, QAA_T proposed by Yang et al. (2013) does not include empirical equations for $a(\lambda)$ and $b_b(\lambda)$ retrievals, and thus it is the most proper algorithm to replace QAA_v6 for retrieving $a(\lambda)$ and $b_b(\lambda)$ in turbid waters (Yang et al., 2014, 2015; Fukushima et al., 2016).

However, QAA_T did not work well in clear waters. For example, if I used QAA_T to retrieve $a(\lambda)$ and $b_b(\lambda)$ for waters with an *in situ* $Z_{SD} \geq 2$ m (there are 158 such points in Figure 3.5), larger errors occurred in the estimated Z_{SD} values with the RMSE of 156.4 m, the MAPE of 627%, and the very low determination coefficient of <0.01 (data not shown). In contrast, QAA_v5 performed very well for these points with the RMSE of 2.8 m, the MAPE of 20%, and the determination coefficient of 0.78.

In QAA_hybrid, I selected QAA_v5 for clear waters rather than QAA_v6. This is because that I found QAA_v5 outperformed QAA_v6 in my dataset. Figure 3.6 shows the comparison of the estimated Z_{SD} values using QAA_v5 and using QAA_v6 for 130 R_{rs} spectra. The 130 R_{rs} spectra were selected by using the criteria of MCI ≤ 0.001 sr^{-1} and $R_{rs}(670) > 0.0015$ sr^{-1}. In other words, the 130 R_{rs} spectra would select 670 nm as reference band if I used QAA_v6 instead of QAA_v5 for clear waters. In contrast, all R_{rs} spectra with MCI ≤ 0.001 sr^{-1} (225 R_{rs} spectra in total) only used 560 nm as reference band in QAA_hybrid. From Figure 3.6, it can be seen that QAA_v5 (Figure 3.6a) performed better than QAA_v6 (Figure 3.6b) with the RMSE reduced from 1.2 m to 1.0 m, the MAPE reduced from 52% to 43%, and the R^2 increased from 0.45 to 0.68. The above findings indicate that it is necessary to select the appropriate QAA according to water turbidities. In other words, it is necessary to use a hybrid QAA to address various waters.

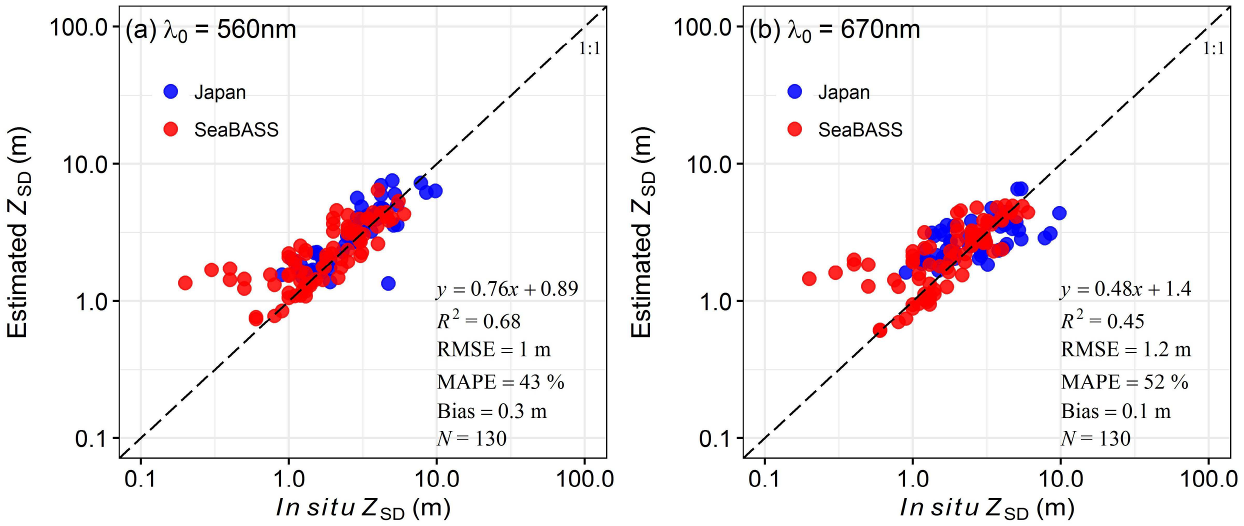

Figure 3.6. Comparisons between *in situ*-measured Z_{SD} values and corresponding estimated Z_{SD} values from 130 selected *in situ* R_{rs} (see text for details). (a) using 560 nm as reference band; (b) using 670 nm as reference band.

In this study, I used MCI = 0.001 sr^{-1} to switch QAA_v5 and QAA_T. This MCI threshold was determined based on Matsushita et al. (2015) based on the data collected from five Asian lakes (Lake Erhai and Lake Dianchi in China; Lake Biwa, Lake Suwa, and Lake Kasumigaura in Japan). My present findings also demonstrated that this threshold is reasonable. Other information can also be used to select the appropriate QAA. For example, Moore et al. (2014) proposed a method to classify waters into seven optical water types (OWTs); Spyrakos et al. (2018) identified 13 OWTs for inland waters based on comprehensive data from more than 250 aquatic systems. Further study is needed to compare the performances of different water classification algorithms for selecting the most appropriate QAAs.

3.4.2. The importance of the estimation of the K_T/K_d ratio

The reported K_T/K_d ratios range from 0.5 to 2.0 (Philpot, 1989; Maritorena et al., 1994; Lee et al., 1994). In the present study, the K_T/K_d ratios were estimated in the range of 0.85–1.70 with an average of 1.28 (Figure 3.4). This range is similar to that reported by Maritorena et al. (1994) with K_T/K_d ratios between 1.02 and 1.66. My results also showed that the K_T/K_d ratios in clear waters are significantly smaller than those in turbid waters (Figure 3.4, $p<0.001$). This finding agrees with Philpot (1989), who reported that the K_T/K_d ratios tended to be higher in strongly absorbing waters.

Compared to the K_T/K_d ratios in turbid waters (with a mean ratio of 1.35), the K_T/K_d ratios in clear waters (with a mean ratio of 1.14) are far smaller than the constant K_T/K_d ratio of 1.5 used in the original Lee15 algorithm. The above findings indicate that the use of the constant K_T/K_d ratio of 1.5 will lead to larger underestimations of the Z_{SD} in clear waters. For example, in Lake Motosu, a clear Japanese lake with the *in situ*-measured Z_{SD} of 16.4 m, the K_T/K_d ratio was estimated to be 1.06 by using Eq. (3.5); the estimated Z_{SD} using the original Lee15 algorithm was 12.34 m with a relative error of 24.8% (Figure 3.5a), and this error was reduced to 8.5% by using the improved Z_{SD} algorithm (the estimated Z_{SD} = 15.01 m, Figure 3.5d). Even in a turbid Japanese lake, i.e., Lake Kasumigaura, the use of dynamic K_T/K_d ratios also improved the Z_{SD} estimations (Figure 3.5b vs. Figure 3.5d).

Although my results have confirmed that the use of the dynamic K_T/K_d ratios can improve Z_{SD} estimations in both clear and turbid waters, further study is still needed to evaluate the relationship between K_T and K_d in various waters due to the Eq. (3.5) is based on an assumption of treating a Secchi disk as a lambertian bottom.

3.4.3. Applicability of the improved Z_{SD} algorithm

Similar to the original Lee15 algorithm, the improved Z_{SD} algorithm does not require any *in situ* data for recalibration. This is because both the QAA_hybrid (the combination of QAA_v5 and QAA_T) and the equation for estimating K_T/K_d ratios (i.e., Eq. (3.5)) are designed as only using semi-analytical equations, which indicates that the assumptions and empirical equations are all of secondary importance for Z_{SD} retrievals (Lee et al., 1998, 2002, 2015a; Yang et al., 2013). Therefore, although I validated the improved Z_{SD} algorithm by using only the data collected from 21 Japanese waters and SeaBASS dataset, it is apparent that the algorithm can also be applied for Z_{SD} estimations in other waters worldwide.

Since both the original and improved Lee15 algorithms used only a single band for Z_{SD} retrieval (i.e., the band with the minimum K_d), an accurate algorithm for atmospheric correction is crucial when actual satellite data are used. For clear ocean waters, the atmospheric correction algorithm proposed by Gordon and Wang (1994) will be the best choice, whereas for turbid inland waters, although there are several algorithms (e.g., Ruddick et al., 2000; Wang and Shi, 2007; Guanter et al., 2007; Doerffer and Schiller, 2008; Bailey et al., 2010; Jaelani et al., 2015), it is still not clear which is the most appropriate algorithm for atmospheric correction. Further studies should be carried out in the future to address the problem of atmospheric correction.

3.5. Conclusions

The original Lee15 algorithm showed overestimations of Z_{SD} values in turbid waters and underestimations of Z_{SD} values in clear waters. In the present study, the use of QAA_hybrid instead of QAA_v6 mainly overcame the former shortcoming through blending QAA_T and QAA_v5 for estimating more accurate absorption and backscattering coefficients in both turbid (QAA_T) and clear waters (QAA_v5); and the use of the dynamic $K_{\mathrm{T}}/K_{\mathrm{d}}$ ratios instead of using the fixed $K_{\mathrm{T}}/K_{\mathrm{d}}$ ratio (i.e., 1.5) mainly overcame the latter shortcoming in the original Lee15 algorithm. The results of this study show that the improved Z_{SD} algorithm gave more accurate Z_{SD} estimations, with RMSE reduced from 2 m to 1.7 m and MAPE reduced from 54% to 35% for using the *in situ* R_{rs} values from 21 Japanese waters (Z_{SD} values ranged from 0.3 m to 16.4 m, N=305) and SeaBASS dataset (Z_{SD} values ranged from 0.2 m to 45 m, N=167). The improved Z_{SD} algorithm is expected to estimate more accurate Z_{SD} values in various types of waters.

Chapter IV Long-term Change of Water Transparency from Time-series Satellite Images in Six Japanese Lakes

4.1. Introduction

The problems of estimating Z_{SD} from remote sensing have been addressed in chapter II and chapter III, and an improved Z_{SD} algorithm has been proposed. The accuracy of the improved Z_{SD} algorithm has been validated using 472 *in situ* R_{rs} and corresponding Z_{SD} values collected from a wide range of water qualities (Z_{SD} ranges from 0.2 to 45 m). As water quality of lakes is tightly related to public health and ecosystem services (Keeler et al., 2012; Ho et al., 2019), routinely monitoring the water quality of lakes is critical in environment management. Therefore, the objective of this chapter is to apply the improved Z_{SD} algorithm to MERIS satellite images over six Japanese lakes to obtain the time-series Z_{SD} and analyze their changing trends.

4.2. Methods

4.2.1. Study area

The study areas include six lakes with different water qualities (Z_{SD} from 0.7 m to 22 m) in Japan. They are Lake Mashu, Lake Kussharo, Lake Inawashiro, Lake Kasumigaura, Lake Suwa and Lake Biwa (Figure 4.1). Lake Mashu is the clearest lake in Japan, with a surface area of 19 km^2. The maximum Z_{SD} was observed as 41.6 m in 1931 (Tsunogai et al., 2011), but decreased to 22 m in 2017. Lake Kussharo is a volcanic lake with a surface area of 79.5 km^2, the Z_{SD} is around 10 m in 2002 (Ban and Suzuki, 2003). Lake Inawashiro is a clear lake located in the Fukushima Prefecture, its surface area is 104.8 km^2, and the Z_{SD} was observed around 13 m in 2019. Lake Kasushimigaura is the second biggest lake in Japan (167.6 km^2, west part), it is a shallow turbid lake with the Z_{SD} of 0.7 m in 2018. Lake Suwa is a small shallow lake in Nagano Prefecture, its surface area is 13.3 km^2, and the Z_{SD} was observed around 1.5 m in 2018. Lake Biwa is the biggest lake in Japan, with a surface area of 670.3 km^2. It is compromised by the deep northern part and the shallow southern part, with the Z_{SD} of 5.2 m and 2.5 m respectively in 2016.

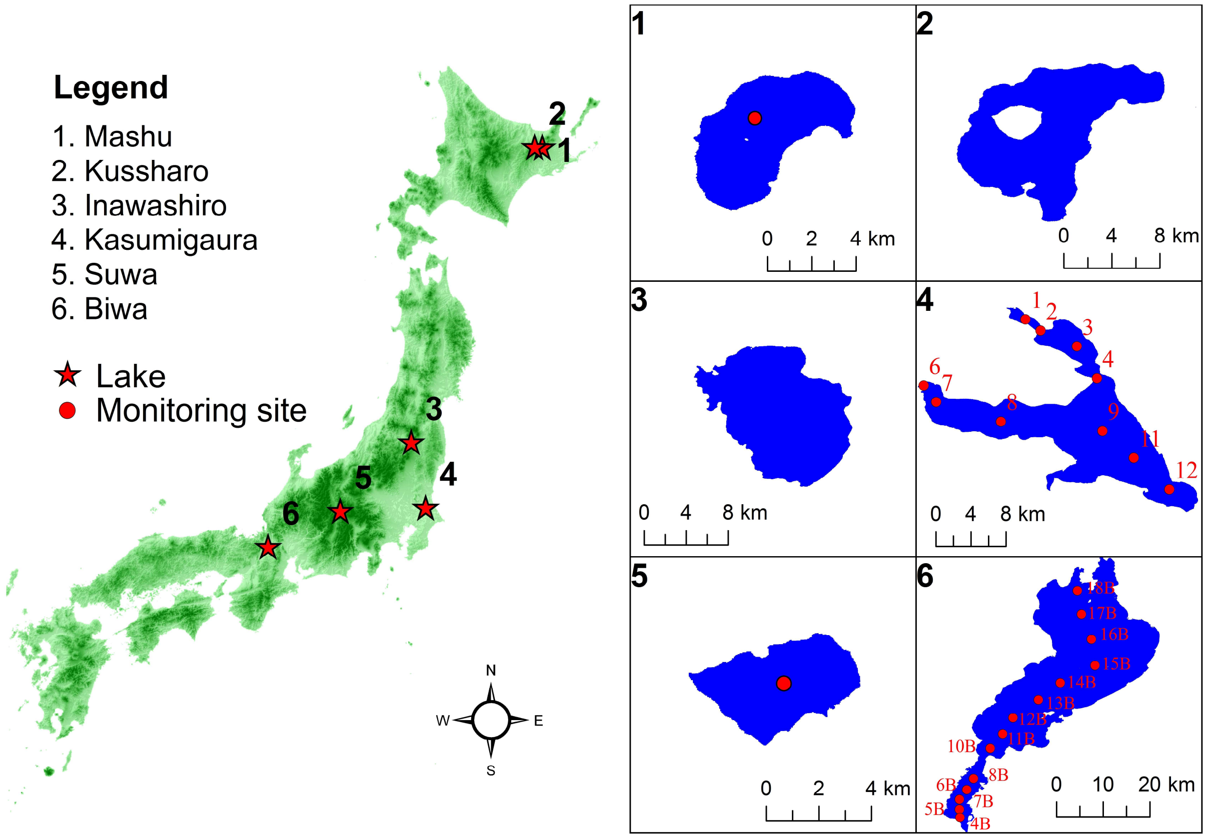

Figure 4.1. Study areas. Red points represent the sampling sites.

4.2.2. *In situ* data collection

In situ Z_{SD} data were collected from Lake Biwa, Lake Kasumigaura, Lake Suwa and Lake Mashu. For Lake Biwa, the *in situ* Z_{SD} data at 14 sites (Figure 4.1) during 2008 and 2012 were collected from Lake Biwa Environmental Research Institute, Shiga prefecture, Japan. The Z_{SD} values ranged from 0.9 m to 11 m. For Lake Kasumigaura, the *in situ* Z_{SD} data at 10 monitoring sites (Figure 4.1) between 2003 and 2012 were obtained from the Lake Kasumigaura Database, which was published by the National Institute for Environmental Studies, Japan (NIES, 2016). The Z_{SD} values ranged from 0.2 m to 1.3 m. For Lake Suwa, the *in situ* Z_{SD} at the center (Figure 4.1) of the lake were obtained from Shinshu University, Japan, this data covers from 2003 to 2012 with a Z_{SD} values of 0.4 - 3.6 m. For Lake Mashu, the in situ Z_{SD} data at the deepest point of the lake (Figure 4.1) were obtained from the National Institute for Environmental Studies, Japan (NIES, 2016), this data covers from 2003 to 2012 with a Z_{SD} values of 14 - 28 m. The above collected *in situ* Z_{SD} data will be used for validation of the satellite-estimated Z_{SD} by comparing the matchups (data acquired at the same day) in each lake, and also comparing the long-term changing trends with the satellite-estimated results.

4.2.3. Satellite image processing

The MEdium Resolution Imaging Spectrometer (MERIS) data was used in this study because of its higher spatial (300 m) and temporal (3 days') resolutions. All available MERIS images covering the six studied lakes from 2003 to 2012 were downloaded from the European Space

Agency (ESA, https://www.esa.int/ESA). There are totally 3448 MERIS images were downloaded for all the six lakes (Table 4.1), the downloaded images were first clipped to the lake area, and then radiometric correction was performed to remove the smile-effect.

The Case-2 Regional Processor in the BEAM 5.0 Earth Observation Toolbox and Development Platform (Brockmann Consult, Geesthacht, Germany) was used to perform atmospheric correction. Clouds, cloud shadows, cloud buffers and coastal lines were then detected using the Idepix algorithm in the Sentinel Application Platform 6.0 (SNAP). Finally, the pixels with failed atmospheric correction, clouds, cloud shadows, cloud buffers, or land and coastal lines were masked out. A total of 781 images were remained for the Z_{SD} estimation (Table 4.1), and the improved Z_{SD} algorithm in chapter III was applied to the remained MERIS images to retrieve Z_{SD} for the six studied lakes.

Table 4.1. Number of satellite images used for the six lakes in this study

Lake	Downloaded image (scene)	Used image (scene)
Mashu	698	135
Kussharo	698	142
Inawashiro	538	79
Kasumigaura	507	138
Suwa	495	173
Biwa	512	114
In total	3448	781

Matchups were generated to compare MERIS-derived Z_{SD} values and the *in situ*-measured Z_{SD} values (acquired on the same day). A 3×3 window was used to extract the estimated Z_{SD} values from the MERIS images, and the averaged Z_{SD} estimations of the 3×3 pixels were used for the comparison to mitigate effects due to imperfect geometric corrections. In addition, a temporal trend analysis was carried out for both measured and estimated Z_{SD} values during the study period using a linear regression method, which has been widely used in previous studies (e.g., Shang et al., 2016).

4.2.4. Accuracy assessment

The root mean square error (RMSE), the mean absolute percentage error (MAPE), and bias were used to evaluate the accuracy of satellite-estimated Z_{SD} values. The equations are as follows:

$$\mathrm{RMSE} = \sqrt{\frac{\sum_{i=1}^{N}\left(X_{\mathrm{estimated},i}-X_{\mathrm{measured},i}\right)^2}{N}} \tag{4.1}$$

$$\mathrm{MAPE} = \frac{1}{N}\sum_{i=1}^{N}\left|\frac{X_{\mathrm{estimated},i}-X_{\mathrm{measured},i}}{X_{\mathrm{measured},i}}\right| \cdot 100\% \tag{4.2}$$

$$\mathrm{Bias} = \frac{1}{N}\sum_{i=1}^{N}\left(X_{\mathrm{estimated},i} - X_{\mathrm{measured},i}\right), \tag{4.3}$$

where $X_{\mathrm{estimated}}$ is the estimated Z_{SD}, X_{measured} is the corresponding *in situ* measurement, and N is the number of data. The determination coefficient (R^2) was also calculated for reference.

4.3. Results

4.3.1. Validation using Z_{SD} matchups

Figure 4.2 shows the comparisons of the estimated Z_{SD} values from actual MERIS data and the *in situ*-measured Z_{SD} values in Lake Mashu, Lake Kasumigaura, Lake Suwa and Lake Biwa (Z_{SD} values are acquired at the same day). Good performance in Lake Mashu and Lake Kasumigaura were obtained, with MAPE=11% in Lake Mashu from 6 matchups (Figure 4.2a) and

MAPE=15% in Lake Kasumigaura from 19 matchups (Figure 4.2b), respectively. Except for several overestimated Z_{SD}, most of the Z_{SD} were properly estimated in Lake Suwa, with the RMSE=0.9 m and MAPE=52% from 27 matchups (Figure 4.2c). However, in Lake Biwa, the Z_{SD} were overestimated with RMSE=3.4 m and MAPE=53% from 14 matchups, although the R^2 is as high as 0.7 (Figure 4.2d).

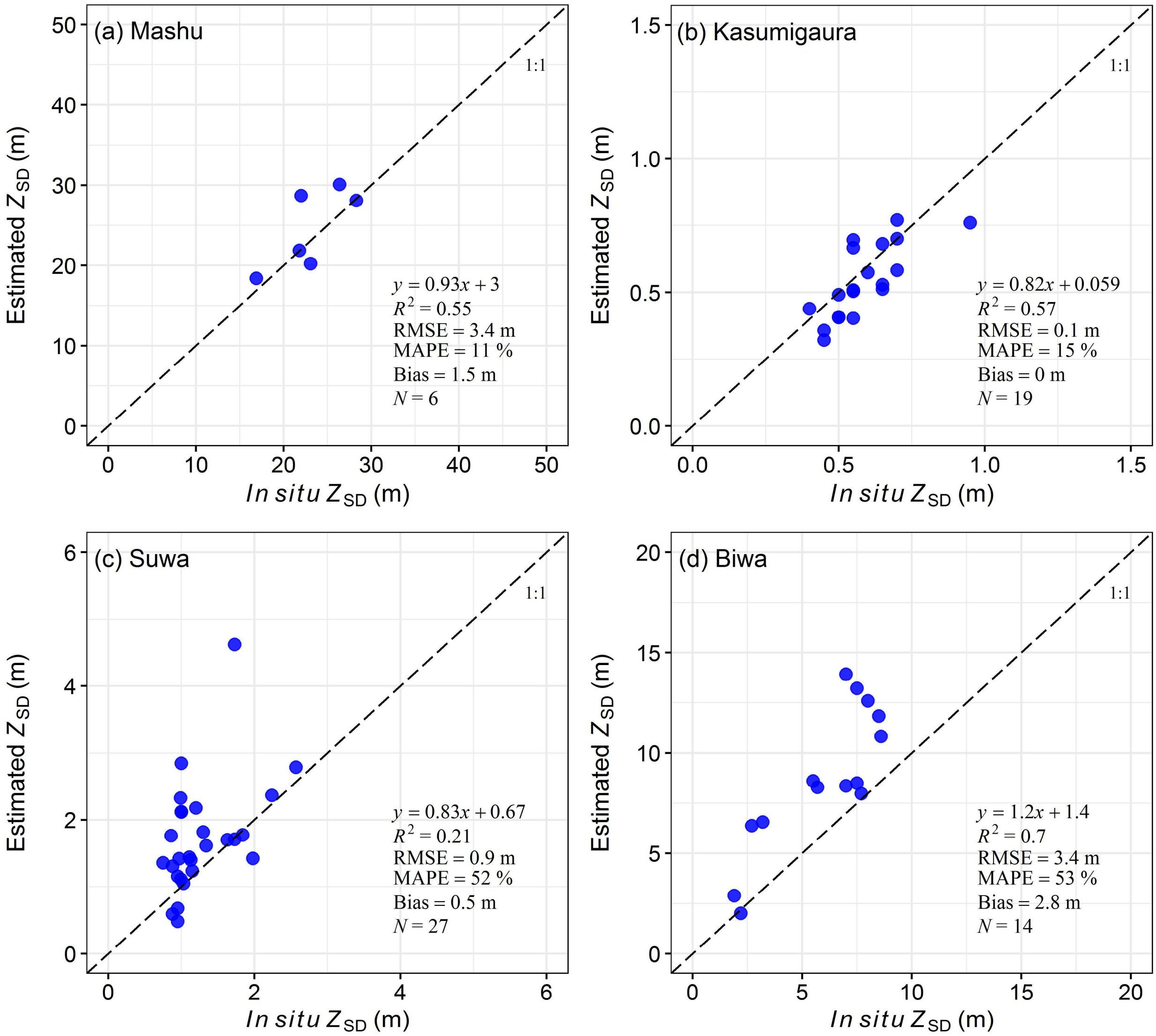

Figure 4.2. Comparisons of the *in situ* Z_{SD} and estimated Z_{SD} values from MERIS data using the improved Z_{SD} algorithm in Chapter III. (a) Lake Mashu. (b) Lake Kasumigaura. (c) Lake Suwa. (d) Lake Biwa.

4.3.2. Long-term Z_{SD} variation

Figure 4.3-Figure 4.6 show the comparison of the *in situ* and estimated Z_{SD} values in Lake Mashu, Lake Suwa, Lake Kasumigaura and Lake Biwa during the study period of 2003-2012. After excluding the images with clouds, there are 135 images remained to estimate Z_{SD} for Lake Mashu, and there are 173 images remained for estimating Z_{SD} for Lake Suwa. For Lake Kasumigaura, there are 138 MERIS images were remained. However, because a few sites were covered by clouds, cloud shadows, or not covered by MERIS images (Lake Kasumigaura was partly covered by one MERIS image), there were the following numbers of available MERIS images for the sites: 122 images for site 3; 72 images for site 4; 114 images for site 7; 135 images for site 8; 138 images for site 9; 133 images for site 11; and 124 images for site 12. Sites 1, 2 and 6 of Lake Kasumigaura were excluded from the comparison because they are too close to the shoreline and strongly influenced by the land (i.e. no any available estimated Z_{SD} values within the 3×3 windows after one pixel buffer from shoreline was removed). For Lake Biwa, there are the following available data for each site: 87 images for site 18B, 93 images for site17B, 109 images for site 16B, 114 images for site 15B, 102 images for site 14B, 100 images for site 13B, 93 images for site 12B,101 images for site 11B, 96 images for site 10B, 101 images for site 8B, 99 images for site 7B, 93 images for site 6B,98 images for site 5B, and 92 images for site 4B.

As it can be seen from Figure 4.3-Figure 4.5, the estimated Z_{SD} values from satellite images (red dashed line with solid circles) matched well with the *in situ* measured Z_{SD} values (blue dashed line with solid circles) in Lake Mashu (Figure 4.3), Lake Suwa (Figure 4.4), and Lake

Kasumigaura (Figure 4.5). The temporal trends of Z_{SD} values obtained from satellite images (red solid line) agreed well with those obtained from *in situ* data (blue solid line) in Lake Suwa and Lake Kasumigaura, both of them showed a significant increase trend with slope>0 and $p<0.05$ (Figure 4.4 and 4.5), even though several outliers were still observed in Lake Suwa. However, the satellite-estimated Z_{SD} shows a significant increase trend during 2003-2012 (red solid line, slope>0, $p<0.05$) in Lake Mashu, the *in situ* Z_{SD} shows that there is no significant change of the Z_{SD} during the study period (blue solid line, $p=0.3$).

For Lake Biwa, from site 17B to site 11B (Figure 4.6b-h), the satellite-estimated Z_{SD} value (red dashed line with solid circles) match the *in situ* Z_{SD} value (blue dashed line with solid circles). For other sites (Figure 4.6a, i-n), the satellite-estimated Z_{SD} value is apparently higher than *in situ* Z_{SD} value. Except for site 5B and site 7B, both the satellite-estimated Z_{SD} and *in situ* Z_{SD} show there is no significant change of the Z_{SD} trend during 2003 and 2012, with p values >0.05.

Figure 4.7 illustrates the Z_{SD} trends in Lake Kussharo and Lake Inawashiro during 2003-2012. Because there is no *in situ* data for comparison, the lake averaged Z_{SD} were plot for both lakes. From the figure, it can be seen that there is no significant change of the Z_{SD} for Lake Kussharo during 2003-2012, and the Z_{SD} is keep at around 15 m (Figure 4.7a). The Z_{SD} in Lake Inawashiro shows a significant increased trend from 2003 to 2012 with slope>0 and p value<0.05 (Figure 4.7b).

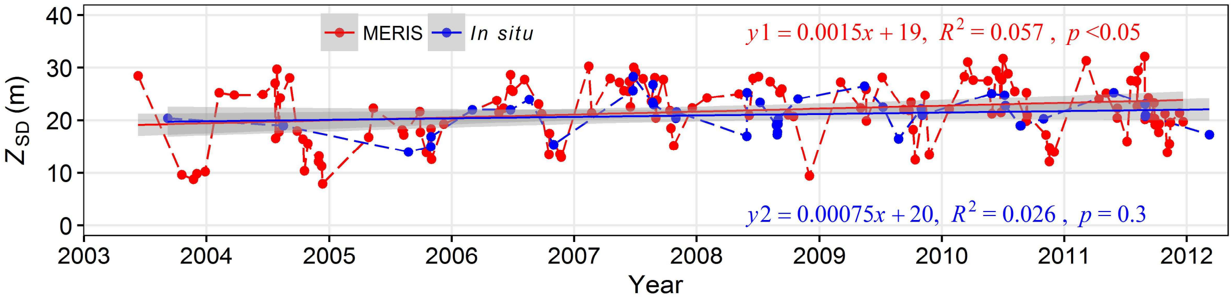

Figure 4.3. Long-term Z_{SD} trend from 2003 to 2012 in Lake Mashu. Red dashed line with solid circles represents MERIS-derived Z_{SD} values using the improved Z_{SD} algorithm developed in Chapter III, and red solid line represents temporal trend obtained from the MERIS-derived Z_{SD} values (y1); blue dashed line with solid circles represents *in situ*-measured Z_{SD} values, and blue solid line represents temporal trend obtained from the *in situ*-measured Z_{SD} values (y2).

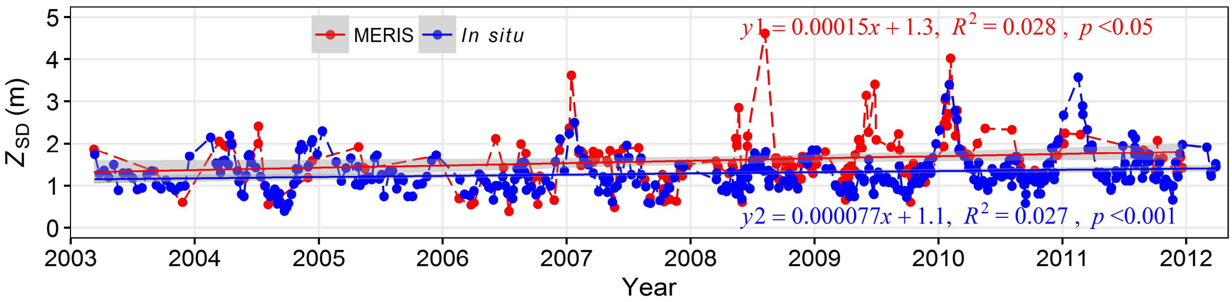

Figure 4.4. Z_{SD} changes from 2003 to 2012 at the center of Lake Suwa. Red dashed line with solid circles represents MERIS-derived Z_{SD} values using the improved Z_{SD} algorithm developed in Chapter III, and red solid line represents temporal trend obtained from the MERIS-derived Z_{SD} values (y1); blue dashed line with solid circles represents *in situ*-measured Z_{SD} values, and blue solid line represents temporal trend obtained from the *in situ*-measured Z_{SD} values (y2).

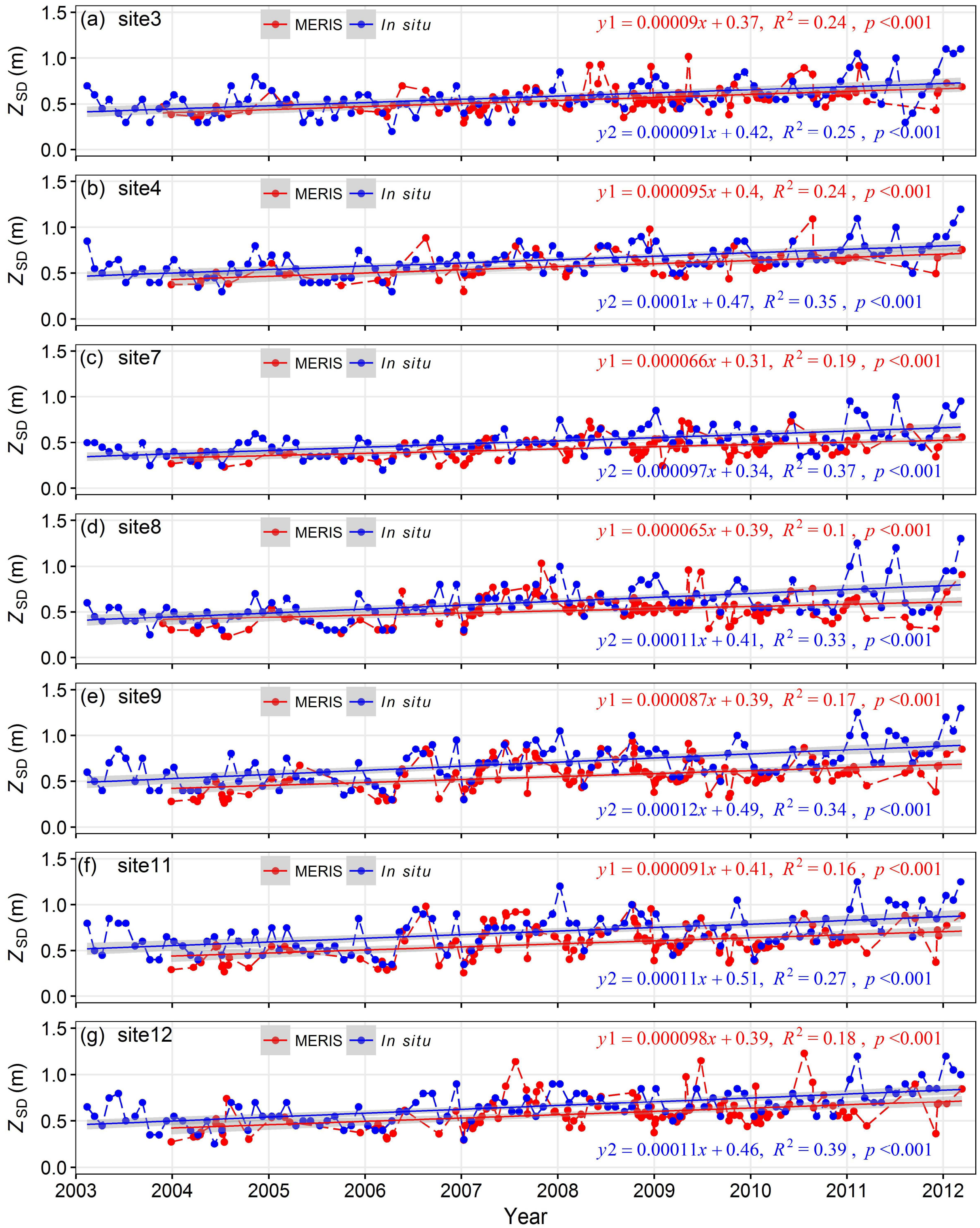

Figure 4.5. Z_{SD} changes from 2003 to 2012 at seven sites in Lake Kasumigaura. Red dashed line with solid circles represents MERIS-derived Z_{SD} values using the improved Z_{SD} algorithm developed in Chapter III, and red solid line represents temporal trend obtained from the MERIS-

derived Z_{SD} values (y1); blue dashed line with solid circles represents *in situ*-measured Z_{SD} values, and blue solid line represents temporal trend obtained from the *in situ*-measured Z_{SD} values (y2).

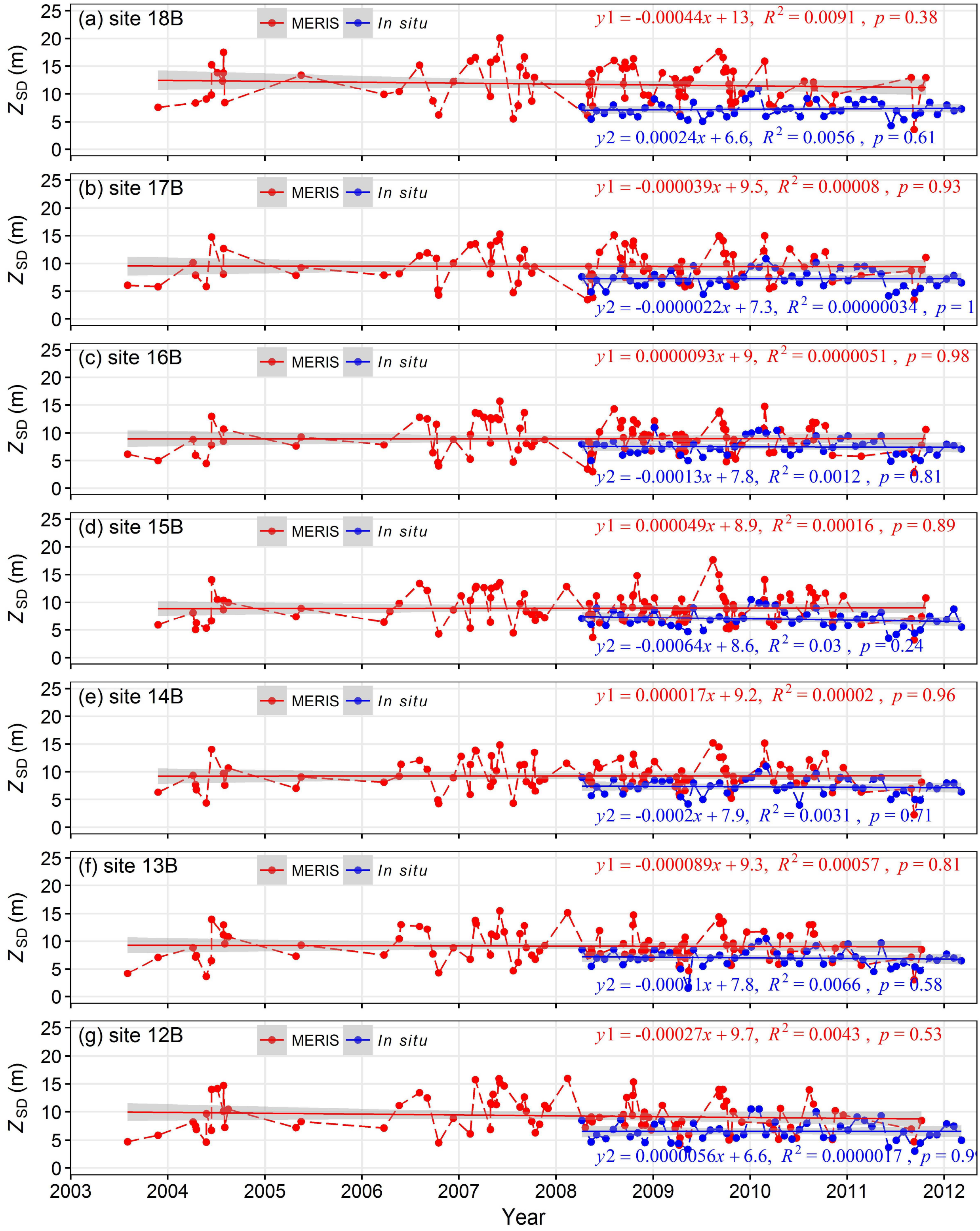

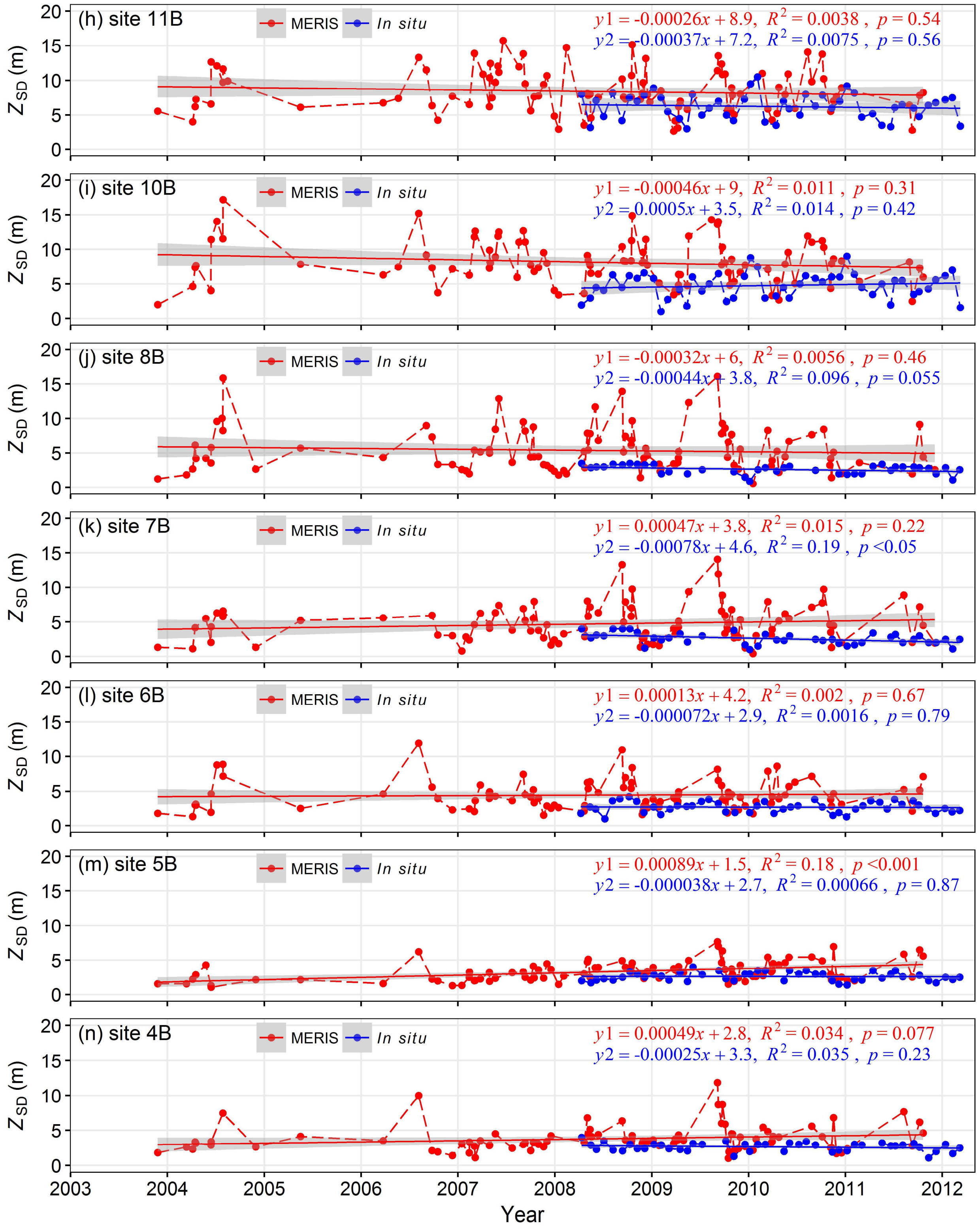

Figure 4.6. Z_{SD} changes from 2003 to 2012 at the 14 sites in Lake Biwa. Red dashed line with solid circles represents MERIS-derived Z_{SD} values using the improved Z_{SD} algorithm developed in Chapter III, and red solid line represents temporal trend obtained from the MERIS-derived Z_{SD}

values (y1); blue dashed line with solid circles represents *in situ*-measured Z_{SD} values, and blue solid line represents temporal trend obtained from the *in situ*-measured Z_{SD} values (y2).

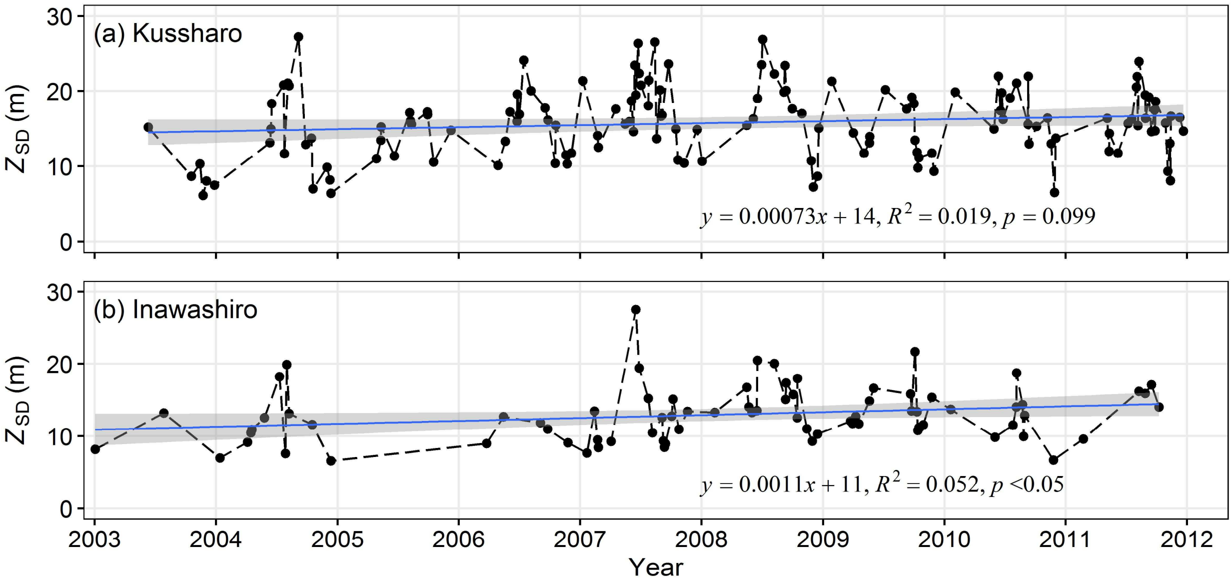

Figure 4.7. Changes of lake averaged Z_{SD} from 2003 to 2012 for Lake Kussharo and Lake Inawashiro. Black dashed line with solid circles represents lake averaged Z_{SD} values from MERIS images using the improved Z_{SD} algorithm developed in Chapter III, blue solid line represents the temporal trend obtained from MERIS-derived Z_{SD}.

4.3.3. Spatial distribution of Z_{SD}

Figure 4.8-Figure 4.13 illustrate the spatial distribution of annual averaged Z_{SD} estimated from satellite images during 2003-2011 in the six studied lakes. Overall, the Z_{SD} in 2003 is lower than that in other years for all the six lakes.

There is no apparent spatial difference of Z_{SD} within the Lake Mashu (Figure 4.8) and Lake Suwa (Figure 4.12). For the rest of the studied lakes, some spatial differences were observed. For example, the Z_{SD} in the northeast part of Lake Kussharo is lower than that in other parts (Figure 4.9). The Z_{SD} in the northern part of Lake Inawashiro is lower than that in the southern part (Figure 4.10). For Lake Kasumigaura, the Z_{SD} in the western part of the lake is lower than that in the central and eastern parts (Figure 4.11). It can also be clearly seen that the Z_{SD} in the southern and eastern parts of Lake Biwa is lower than that in the western and northern parts (Figure 4.13).

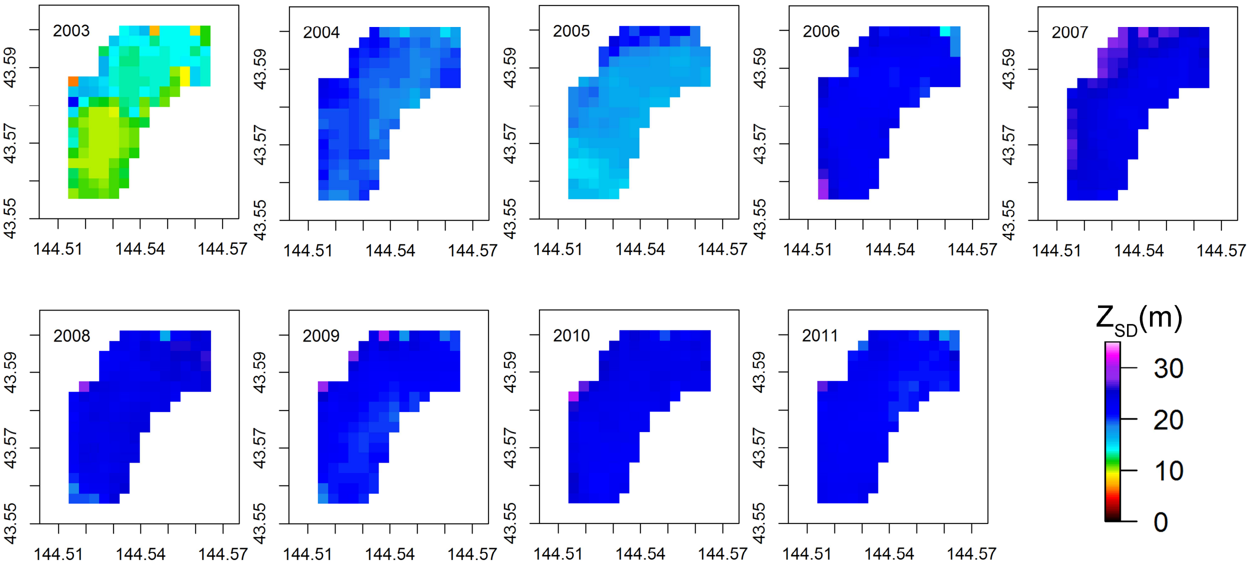

Figure 4.8. Spatial distribution of annual averaged Z_{SD} from 2003 to 2011 in Lake Mashu.

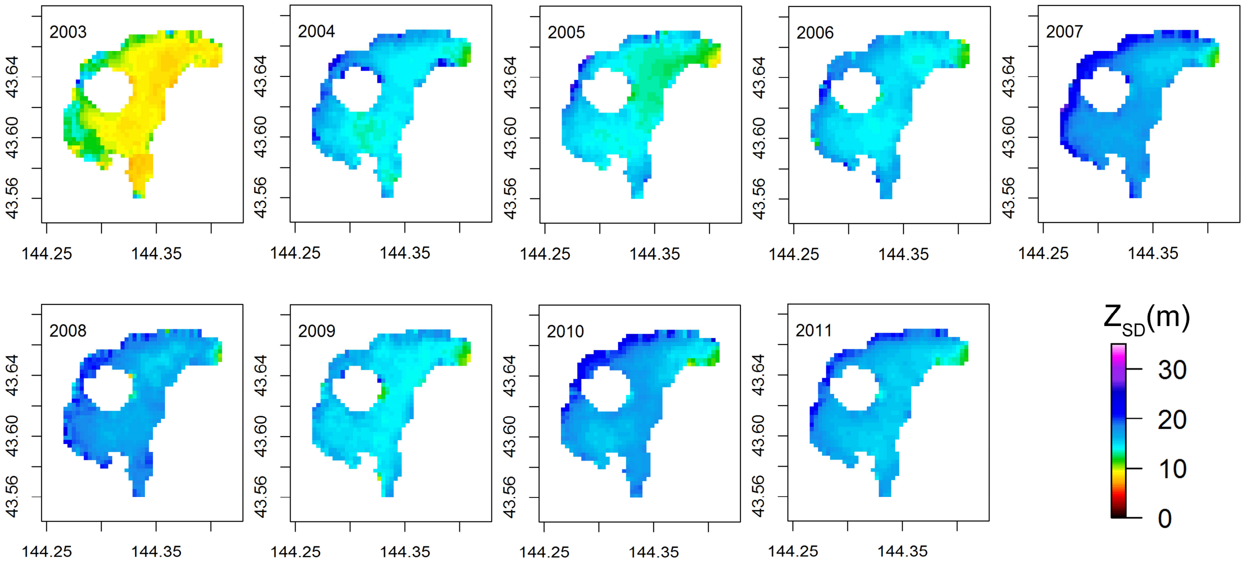

Figure 4.9. Spatial distribution of annual averaged Z_{SD} from 2003 to 2011 in Lake Kussharo.

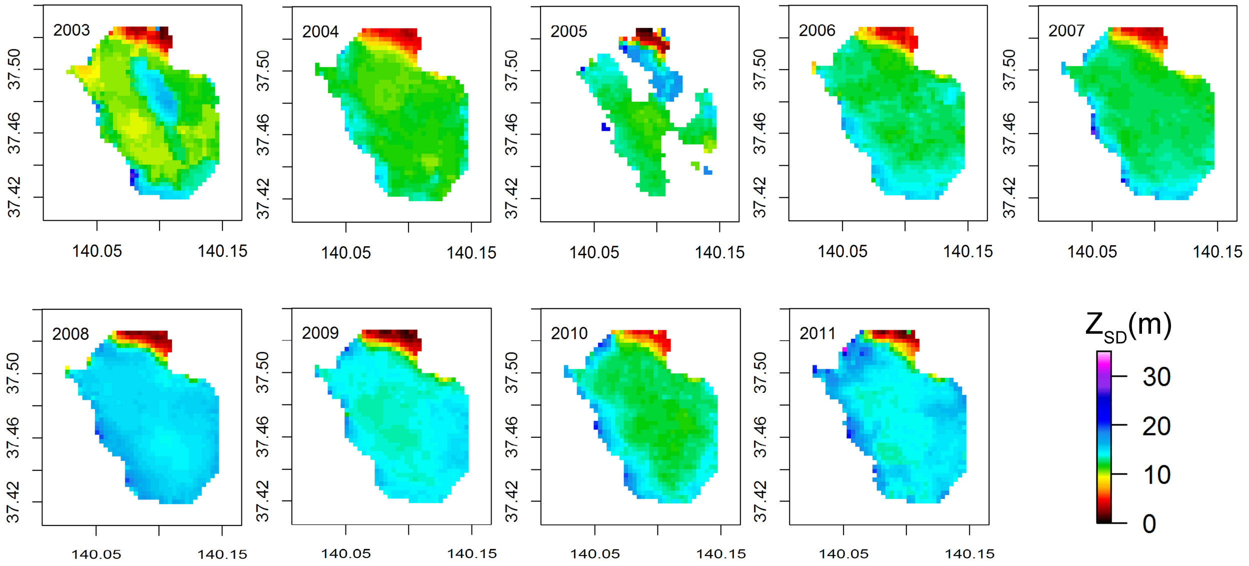

Figure 4.10. Spatial distribution of annual averaged Z_{SD} from 2003 to 2011 in Lake Inawashiro.

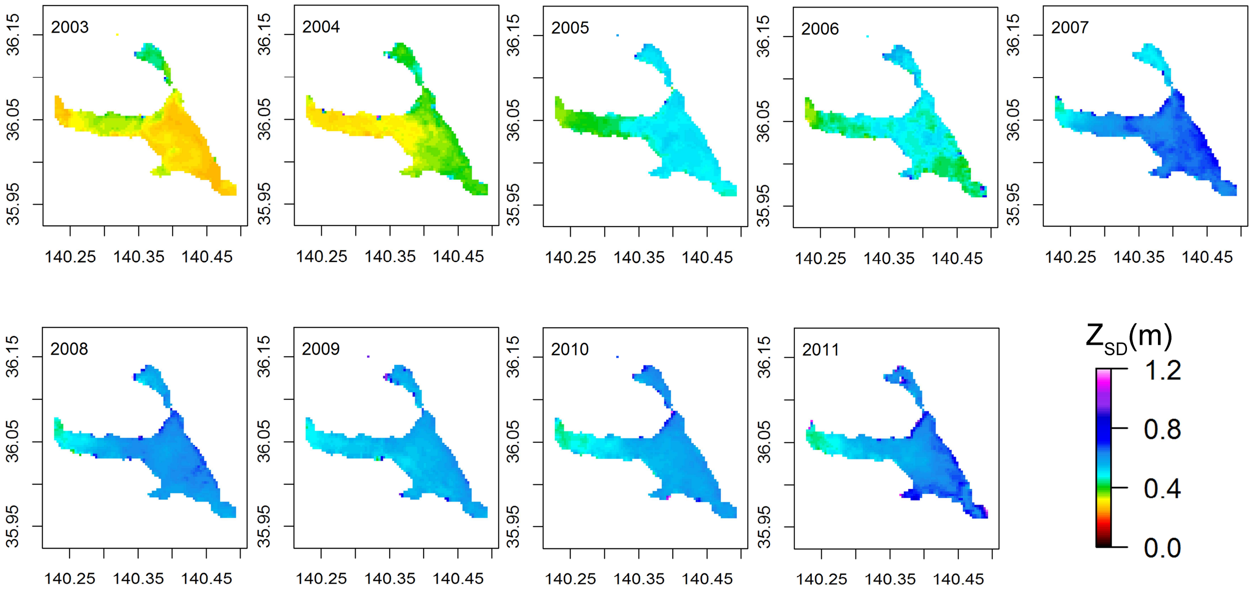

Figure 4.11. Spatial distribution of annual averaged Z_{SD} from 2003 to 2011 in Lake Kasumigaura.

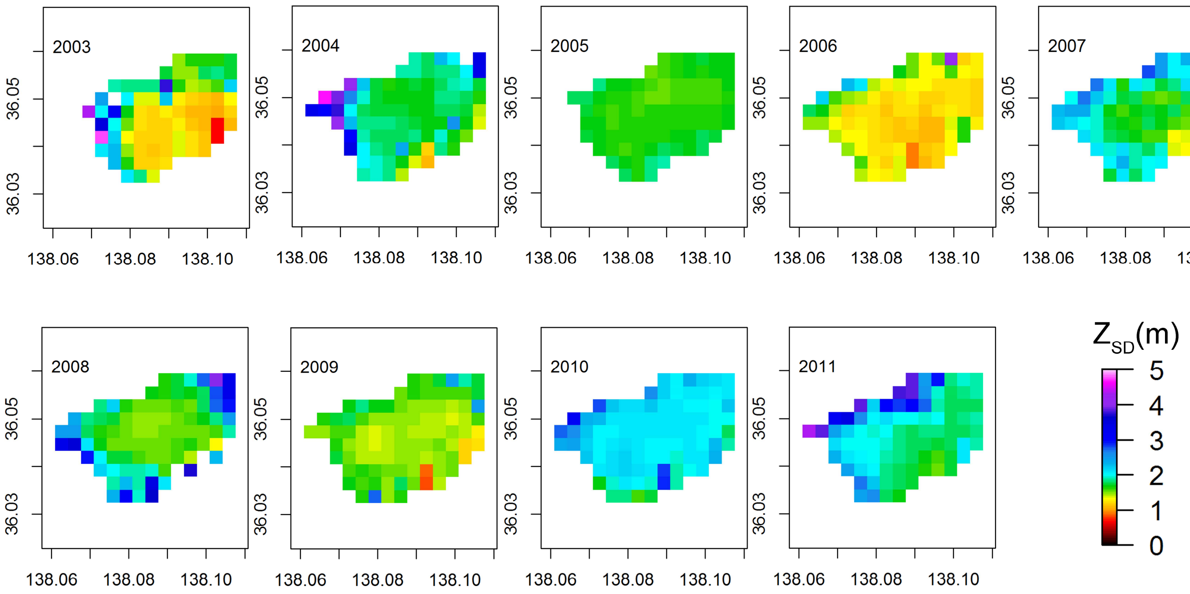

Figure 4.12. Spatial distribution of annual averaged Z_{SD} from 2003 to 2011 in Lake Suwa.

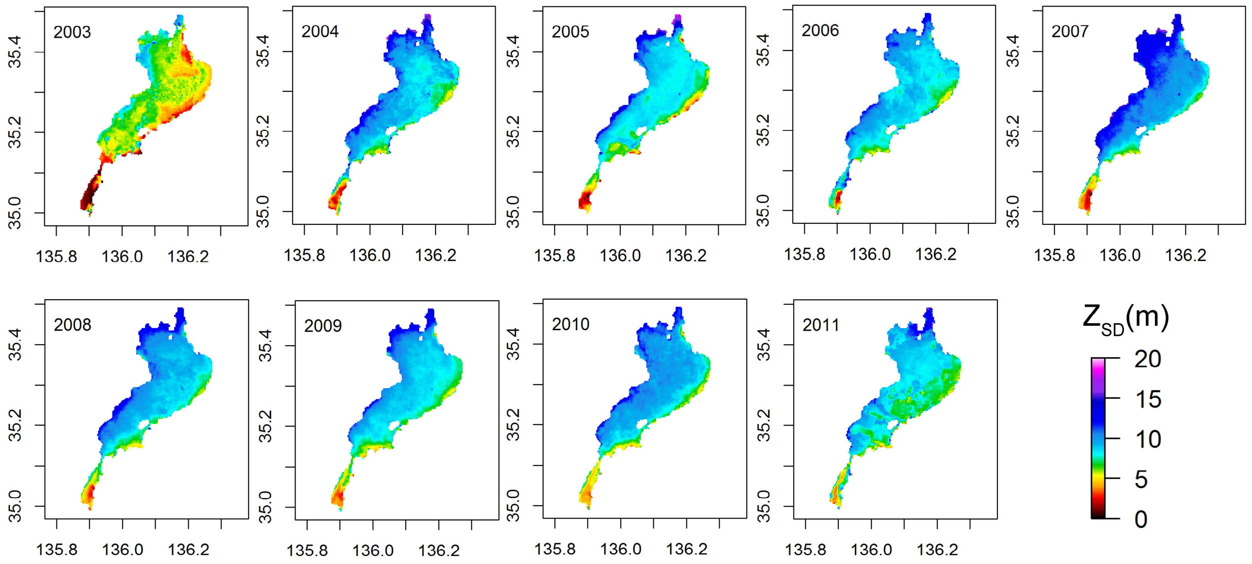

Figure 4.13. Spatial distribution of annual averaged Z_{SD} from 2003 to 2011 in Lake Biwa.

4.4. Discussion

4.4.1. Influence of atmospheric correction on Z_{SD} estimation

Different from the Z_{SD} values estimated from *in situ* measured R_{rs}, the accuracy of Z_{SD} values estimated from the satellite images were also strongly influenced by the atmospheric correction procedure. In this chapter, the Case2 processor in BEAM 5.0 was used to do atmospheric correction for MERIS images. The Z_{SD} were accurately estimated in Lake Mashu, Kasumigaura and most of the points in Lake Suwa (Figure 4.2a-c). However, the Z_{SD} in Lake Biwa and several points in Lake Suwa were overestimated (Figure 4.2c-d).

Estimating Z_{SD} from accurate *in situ* R_{rs} using the improved Z_{SD} algorithm has shown good results (chapter III). Because there is no available concurrent *in situ* R_{rs} to validate the atmospheric correction results in Lake Biwa and Suwa in this study, another method called MUMM in SeaDAS 7.5.3 was applied to do atmospheric correction (Ruddick et al., 2000), to test how different atmospheric correction algorithm influence the Z_{SD} estimations. As Figure 4.14 shows, the Z_{SD} estimations in Lake Biwa and several points in Lake Suwa become more accurate (MAPE decreased from 53% to 26%, and RMSE decreased from 3.4 m to 1.8 m for Lake Biwa) comparing to the use of Case2 processor (Figure 4.2c-d). However, the Z_{SD} estimations in Lake Mashu and Lake Kasumigaura become worse, for example, there is only one data remained after applying MUMM for images in Lake Masu, and the Z_{SD} estimation errors increased from MAPE=15% to MAPE=55% in Lake Kasumigaura (compare Figure 4.2b to Figure 4.14b).

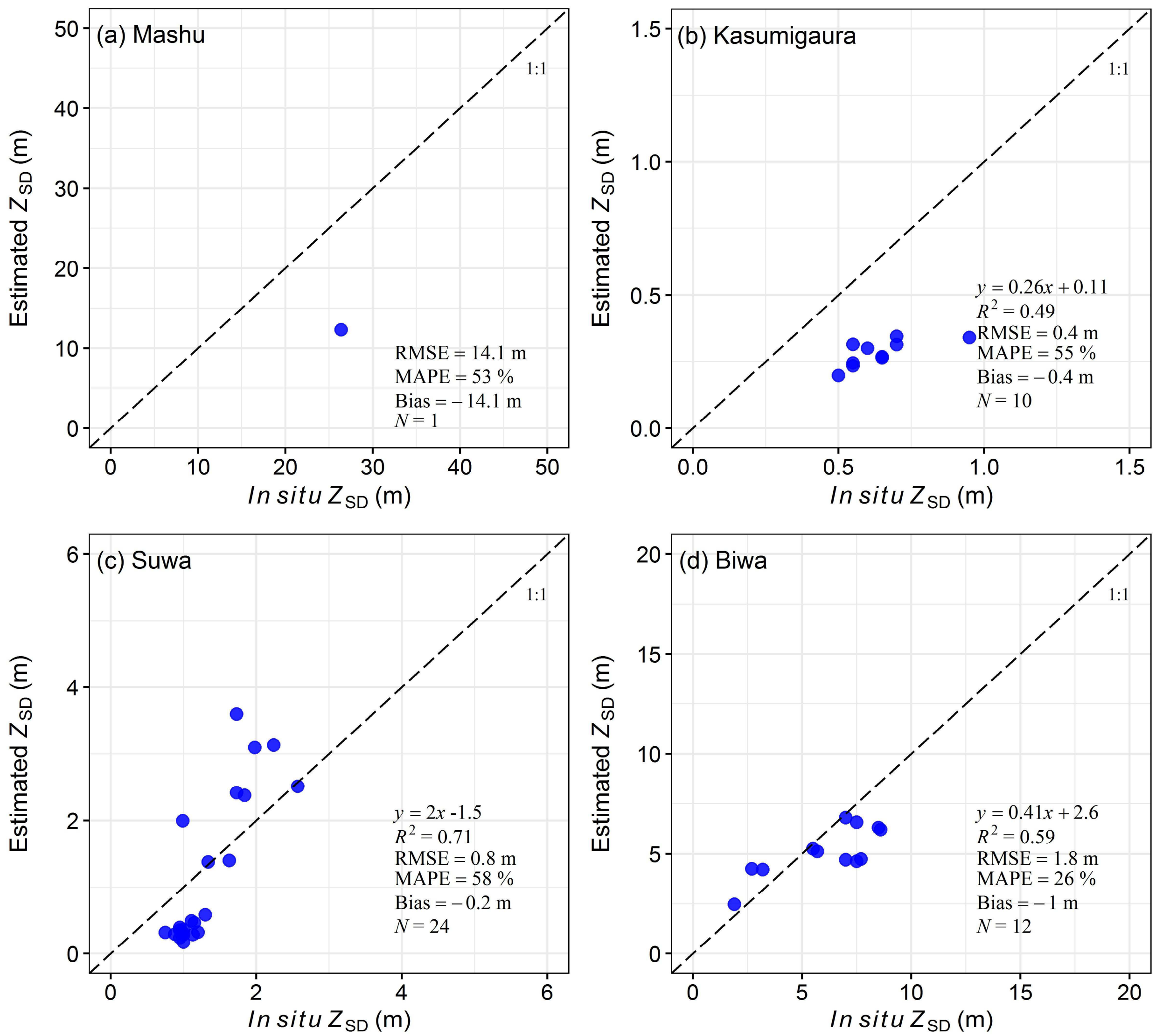

Figure 4.14. Comparison of *in situ* Z_{SD} and estimated Z_{SD} from MERIS images. Different from Figure 4.2, MUMM algorithm was used for atmospheric correction.

Since the improved Z_{SD} algorithms used only a single band for Z_{SD} retrieval (i.e., the band with the minimum K_{d}), an accurate algorithm for atmospheric correction is crucial when actual satellite data are used. For open oceans, the atmospheric correction algorithm proposed by Gordon and Wang (1994) will be the best choice, whereas for turbid inland waters, although there are several algorithms (e.g., Ruddick et al., 2000; Wang and Shi, 2007; Guanter et al., 2007; Doerffer and Schiller, 2008; Bailey et al., 2010; Jaelani et al., 2015), it is still no any algorithm can work in various water types. Therefore, further studies on atmospheric correction is still needed to obtain accurate R_{rs} from satellite images, and then contribute to better water quality monitoring applications.

4.4.2. Z_{SD} changing trend from satellite image

One of the goals in water quality monitoring is to analyze the changing trend of water quality. In this chapter, the long-term changes of Z_{SD} in six Japanese lakes were monitored by applying the improved Z_{SD} algorithm in chapter III to the MERIS satellite images during 2003-2012. The obtained Z_{SD} changing trends in Lake Kasumigaura and Lake Suwa agreed well with the trends of *in situ* data, both of them shows that the Z_{SD} is significant increased from 2003 to 2012 (Figure 4.4 and Figure 4.5).

For lake Mashu, the satellite-estimated Z_{SD} shows a significant increased trend, but the *in situ* data shows that there is no significant change of Z_{SD} during the study period (Figure 4.2). This different trend is probably because of the distribution of the *in situ* data, of witch, 23% *in situ* data were collected in 2008, and 60% of these data in 2008 were collected in August. Thus, the unequal distribution of *in situ* data may influenced the trend analysis in Lake Mashu.

The value of Z_{SD} in Lake Biwa is overestimated, however, the trends obtained from satellite-estimated Z_{SD} agreed well with these obtained from *in situ* Z_{SD} for 12 sites out of the 14 sites (i.e., except for site 7B and site 5B, Figure 4.6). There is no long-term *in situ* data in Lake Inawashiro to validate the changing trend of Z_{SD} obtained from satellite images, but it is reported that the Z_{SD} in Lake Inawashiro is increased (Fukushima Prefecture, 2013), which shows the same results in the present study (Figure 4.7b).

Therefore, the results in this study indicate that by using the improved Z_{SD} algorithm, the Z_{SD} changing trend can be properly monitored from satellite images. It is of great significance for environment management, especially for waters without historical *in situ* data, the long-term change of water transparency can be directly derived from historical satellite images.

4.5. Conclusions

The improved Z_{SD} algorithm was applied to MERIS satellite images to obtain the long-term Z_{SD} for six Japanese lakes. Validation results showed that the improved Z_{SD} algorithm has good performance in Lake Mashu, Lake Kasumigaura and most points of that in Lake Suwa, but overestimated the Z_{SD} values in Lake Biwa and several points in Lake Suwa because of inaccurate atmospheric correction. Although the absolute Z_{SD} value is inaccurate in Lake Biwa, the obtained Z_{SD} trends agreed well with *in situ* Z_{SD} trends. Therefore, combing the improved Z_{SD} algorithm with satellite images could provide proper Z_{SD} changing trend, which would be helpful for the water environment monitoring. To retrieve more accurate Z_{SD} values from satellite images using the improved Z_{SD} algorithm, the big challenge of atmospheric correction should be addressed in the future study.

Chapter V General Conclusions

There are three requirements to use the Lee15 Z_{SD} algorithm: (1) accurate measurements of remote sensing reflectance (R_{rs}); (2) accurate estimations of diffuse attenuation coefficient of downwelling irradiance (K_d); and (3) the proper values of K_T/K_d ratios. In the present study, the above three requirements were all addressed to estimate accurate Z_{SD} in various waters from remote sensing data.

To ensure the accuracy of *in situ* measured R_{rs}, I proposed a new method to remove the residual reflected skylight effects (Δ effects) remained in above-water measured R_{rs}. The new method is simple, effective, and universally applicable without requiring any recalibration. The new proposed method outperformed other existing methods, and can be used for various water types. In addition, the new method can correct *in situ* R_{rs} spectra measured under various sky conditions (clear, scattered clouds, or overcast), and improve the quality of the spectra. The Δ corrections should be carried out for all R_{rs} spectra measured using the above-water approach before they are applied to the development of water quality algorithms or the evaluation of atmospheric correction algorithms.

The accuracy of IOPs (a and b_b) determines the accuracy of K_d estimation. In the present study, a QAA_hybrid was proposed to retrieve more accurate IOPs from R_{rs}. Compared to QAA_v6, QAA_hybrid can retrieve IOPs more accurately in various waters (MAPE decreased from 55% to 24%), and the retrieved IOPs can be then used to estimate more accurate K_d in various waters (MAPE decreased from 52% to 23%).

A new algorithm was proposed to estimate more realistic value of K_T/K_d. The estimated K_T/K_d ratio was used in the Z_{SD} algorithm instead of using the fixed K_T/K_d ratio (i.e., 1.5). The values of estimated K_T/K_d in the present study range from 0.85 to 1.70 with an average of 1.28, which is lower than the 1.5 used in the original Lee15 Z_{SD} algorithm. Compared to using a fixed K_T/K_d of 1.5, the use of a dynamic K_T/K_d can improve Z_{SD} estimation, especially in clear waters.

By combing the QAA_hybrid and the K_T/K_d algorithm, an improved Z_{SD} algorithm was proposed. The improved Z_{SD} algorithm was validated using *in situ* R_{rs} collected from 21 waters in Japan and 4 waters in United States with a wide range of water qualities (Z_{SD} ranges from 0.2 m to 45 m), results showed that the improved Z_{SD} algorithm can be universally applied to various water types with more accurate Z_{SD} estimations (MAPE decreased from 54% to 35%).

The improved Z_{SD} algorithm was also applied to MERIS satellite images to obtain the Z_{SD} for six Japanese lakes during 2003 and 2012. Validation results using matchups showed that the improved Z_{SD} algorithm can retrieve accurate Z_{SD} values in Lake Mashu, Lake Kasumigaura and most points of that in Lake Suwa, but overestimate the Z_{SD} values in Lake Biwa and several points in Lake Suwa because of inaccurate atmospheric correction. The changing trends of Z_{SD} obtained from satellite images in Lake Kasumigaura and Lake Suwa agreed well with the corresponding trends obtained from *in situ* Z_{SD} data during the study period. Although the absolute Z_{SD} value was overestimated in Lake Biwa, the obtained Z_{SD} trends agreed well with *in situ* Z_{SD} trends for 12 out of 14 sites during the study period. Therefore, the improved Z_{SD} algorithm can be used to monitor proper Z_{SD} changing trend from satellite images, which would be helpful in water environment management. However, to retrieve more accurate Z_{SD} from satellite images using the improved Z_{SD} algorithm, the big challenge of atmospheric correction should be addressed in the future study.

References

Alikas, K., & Kratzer, S. (2017). Improved retrieval of Secchi depth for optically-complex waters using remote sensing data. *Ecological Indicators*, *77*, 218-227.

Babin, M., & Stramski, D. (2002). Light absorption by aquatic particles in the near-infrared spectral region. *Limnology and Oceanography*, *47*(3), 911-915.

Babin, M., Morel, A., Fournier-Sicre, V., Fell, F., & Stramski, D. (2003). Light scattering properties of marine particles in coastal and open ocean waters as related to the particle mass concentration. *Limnology and Oceanography*, *48*(2), 843-859.

Bailey, S. W., Franz, B. A., & Werdell, P. J. (2010). Estimation of near-infrared water-leaving reflectance for satellite ocean color data processing. *Optics express*, *18*(7), 7521-7527.

Ban, M., Suzuki, T. (2003). Artificial growth of sockeye salmon in Lake Kussharo. *Salmon ・Mass Resource Management Center Technical Information*, *169*: 13-23.

Barnes, B. B., Garcia, R., Hu, C., & Lee, Z. (2018). Multi-band spectral matching inversion algorithm to derive water column properties in optically shallow waters: An optimization of parameterization. *Remote Sensing of Environment*, *204*, 424-438.

Bernardo, N., Alcântara, E., Watanabe, F., Rodrigues, T., Carmo, A., Gomes, A., & Andrade, C. (2018). Glint removal assessment to estimate the remote sensing reflectance in inland waters with widely differing optical properties. *Remote Sensing*, *10*(10), 1655.

Binding, C. E., Greenberg, T. A., Watson, S. B., Rastin, S., & Gould, J. (2015). Long term water clarity changes in North America's Great Lakes from multi-sensor satellite observations. *Limnology and Oceanography*, *60*(6), 1976-1995.

Brewin, R. J., Dall'Olmo, G., Pardo, S., van Dongen-Vogels, V., & Boss, E. S. (2016). Underway spectrophotometry along the Atlantic Meridional Transect reveals high performance in satellite chlorophyll retrievals. *Remote sensing of environment*, *183*, 82-97.

Cai, L., Tang, D., & Li, C. (2015). An investigation of spatial variation of suspended sediment concentration induced by a bay bridge based on Landsat TM and OLI data. *Advances in Space Research*, *56*(2), 293-303.

Cao, F., Tzortziou, M., Hu, C., Mannino, A., Fichot, C. G., Del Vecchio, R., ... & Novak, M. (2018). Remote sensing retrievals of colored dissolved organic matter and dissolved organic carbon dynamics in North American estuaries and their margins. *Remote sensing of environment*, *205*, 151-165.

Chen, Z., Muller-Karger, F. E., & Hu, C. (2007). Remote sensing of water clarity in Tampa Bay. *Remote Sensing of Environment*, *109*(2), 249-259.

Choi, J. K., Park, Y. J., Ahn, J. H., Lim, H. S., Eom, J., & Ryu, J. H. (2012). GOCI, the world's first geostationary ocean color observation satellite, for the monitoring of temporal variability in coastal water turbidity. *Journal of Geophysical Research: Oceans*, *117*(C9).

Choi, J. K., Park, Y. J., Lee, B. R., Eom, J., Moon, J. E., & Ryu, J. H. (2014). Application of the Geostationary Ocean Color Imager (GOCI) to mapping the temporal dynamics of coastal water turbidity. *Remote Sensing of Environment*, *146*, 24-35.

Craig, S. E., Lohrenz, S. E., Lee, Z., Mahoney, K. L., Kirkpatrick, G. J., Schofield, O. M., & Steward, R. G. (2006). Use of hyperspectral remote sensing reflectance for detection and assessment of the harmful alga, Karenia brevis. *Applied Optics*, *45*(21), 5414-5425.

Dev, P. J., & Shanmugam, P. (2014). A new theory and its application to remove the effect of surface-reflected light in above-surface radiance data from clear and turbid waters. *Journal of Quantitative Spectroscopy and Radiative Transfer*, *142*, 75-92.

Dierssen, H. M., Kudela, R. M., Ryan, J. P., & Zimmerman, R. C. (2006). Red and black tides: Quantitative analysis of water−leaving radiance and perceived color for phytoplankton, colored dissolved organic matter, and suspended sediments. *Limnology and Oceanography*, *51*(6), 2646-2659.

Doerffer, R., and Schiller, H., 2008. MERIS Regional Coastal and Lake Case 2 Water Project - Atmospheric Correction ATBD. GKSS Research Center 21502 Geesthacht Version 1.0 18. May 2008.

Doron, M., Babin, M., Hembise, O., Mangin, A., & Garnesson, P. (2011). Ocean transparency from space: Validation of algorithms estimating Secchi depth using MERIS, MODIS and SeaWiFS data. *Remote Sensing of Environment*, *115*(12), 2986-3001.

Duntley, S. Q. (1952). The visibility of submerged objects. *Visibility Lab., Mass. Inst. Tech* (pp. 74). San Diego: Scripps Institution of Oceanography.

Froidefond, J. M., Gardel, L., Guiral, D., Parra, M., & Ternon, J. F. (2002). Spectral remote sensing reflectances of coastal waters in French Guiana under the Amazon influence. *Remote Sensing* *of Environment*, *80*(2), 225-232.

Fukushima Prefecture. (2013). Inawashiro Lake and Urabandai Lake Aquatic Environment Conservation Promotion Project.

Fukushima, T., Matsushita, B., Oyama, Y., Yoshimura, K., Yang, W., Terrel, M., ... & Takegahara, A. (2016). Semi-analytical prediction of Secchi depth using remote-sensing reflectance for lakes with a wide range of turbidity. *Hydrobiologia*, *780*(1), 5-20.

Fukushima, T., Matsushita, B., Yang, W., & Jaelani, L. M. (2018). Semi-analytical prediction of Secchi depth transparency in Lake Kasumigaura using MERIS data. *Limnology*, *19*(1), 89-100.

Giardino, C., Pepe, M., Brivio, P. A., Ghezzi, P., & Zilioli, E. (2001). Detecting chlorophyll, Secchi disk depth and surface temperature in a sub-alpine lake using Landsat imagery. *Science of the Total Environment*, *268*(1-3), 19-29.

Gordon, H. R., & Wang, M. (1994). Retrieval of water-leaving radiance and aerosol optical thickness over the oceans with SeaWiFS: a preliminary algorithm. *Applied optics*, *33*(3), 443-452.

Gordon, H. R., Brown, O. B., Evans, R. H., Brown, J. W., Smith, R. C., Baker, K. S., & Clark, D. K. (1988). A semianalytic radiance model of ocean color. *Journal of Geophysical Research: Atmospheres*, *93*(D9), 10909-10924.

Gower, J. F. R. (1980). Observations of in situ fluorescence of chlorophyll-a in Saanich Inlet. *Boundary-Layer Meteorology*, *18*(3), 235-245.

Gower, J., King, S., Borstad, G., & Brown, L. (2005). Detection of intense plankton blooms using the 709 nm band of the MERIS imaging spectrometer. *International Journal of Remote Sensing*, *26*(9), 2005-2012.

Goyens, C., Jamet, C., & Schroeder, T. (2013). Evaluation of four atmospheric correction algorithms for MODIS-Aqua images over contrasted coastal waters. *Remote Sensing of Environment*, *131*, 63-75.

Groetsch, P. M., Gege, P., Simis, S. G., Eleveld, M. A., & Peters, S. W. (2017). Validation of a spectral correction procedure for sun and sky reflections in above-water reflectance measurements. *Optics express*, *25*(16), A742-A761.

Guanter, L., Del Carmen González-Sanpedro, M., & Moreno, J. (2007). A method for the atmospheric correction of ENVISAT/MERIS data over land targets. *International Journal of Remote Sensing*, *28*(3-4), 709-728.

Guanter, L., Ruiz-Verdú, A., Odermatt, D., Giardino, C., Simis, S., Estellés, V., ... & Moreno, J. (2010). Atmospheric correction of ENVISAT/MERIS data over inland waters: Validation for European lakes. *Remote Sensing of Environment*, *114*(3), 467-480.

Ho, J. C., Michalak, A. M., & Pahlevan, N. (2019). Widespread global increase in intense lake phytoplankton blooms since the 1980s. *Nature*, *574*(7780), 667-670.

Hu, C. (2009). A novel ocean color index to detect floating algae in the global oceans. *Remote Sensing of Environment*, *113*(10), 2118-2129.

Hu, C., Lee, Z., & Franz, B. (2012). Chlorophyll a algorithms for oligotrophic oceans: A novel approach based on three–band reflectance difference. *Journal of Geophysical Research: Oceans*, *117*(C1).

Huang, J., Chen, L., Chen, X., Tian, L., Feng, L., Yesou, H., & Li, F. (2014). Modification and validation of a quasi-analytical algorithm for inherent optical properties in the turbid waters of Poyang Lake, China. *Journal of Applied Remote Sensing*, *8*(1), 083643.

IOCCG. 2014. Update of the Quasi-Analytical Algorithm (QAA_v6). Available online: http://www.ioccg.org/groups/Software_OCA/QAA_v6_2014209.pdf.

Jaelani, L. M., Matsushita, B., Yang, W., & Fukushima, T. (2013). Evaluation of four MERIS atmospheric correction algorithms in Lake Kasumigaura, Japan. *International Journal of Remote Sensing*, *34*(24), 8967-8985.

Jaelani, L. M., Matsushita, B., Yang, W., & Fukushima, T. (2015). An improved atmospheric correction algorithm for applying MERIS data to very turbid inland waters. *International Journal of Applied Earth Observation and Geoinformation*, *39*, 128-141.

Jiang, D., Matsushita, B., Setiawan, F., & Vundo, A. (2019). An improved algorithm for estimating the Secchi disk depth from remote sensing data based on the new underwater visibility theory. *ISPRS Journal of Photogrammetry and Remote Sensing*, *152*, 13-23.

Kabbara, N., Benkhelil, J., Awad, M., & Barale, V. (2008). Monitoring water quality in the coastal area of Tripoli (Lebanon) using high-resolution satellite data. *ISPRS Journal of Photogrammetry and Remote Sensing*, *63*(5), 488-495.

Keeler, B. L., Polasky, S., Brauman, K. A., Johnson, K. A., Finlay, J. C., O'Neill, A., ... & Dalzell,

B. (2012). Linking water quality and well-being for improved assessment and valuation of ecosystem services. *Proceedings of the National Academy of Sciences*, *109*(45), 18619-18624.

Kim, S. H., Yang, C. S., & Ouchi, K. (2015). Spatio-temporal patterns of Secchi depth in the waters around the Korean Peninsula using MODIS data. *Estuarine, Coastal and Shelf Science*, *164*, 172-182.

Kirk, J. T. (2011). Light and photosynthesis in aquatic ecosystems. Cambridge University Press.

Kloiber, S. M., Brezonik, P. L., Olmanson, L. G., & Bauer, M. E. (2002). A procedure for regional lake water clarity assessment using Landsat multispectral data. *Remote sensing of Environment*, *82*(1), 38-47.

Knaeps, E., Dogliotti, A. I., Raymaekers, D., Ruddick, K., & Sterckx, S. (2012). In situ evidence of non-zero reflectance in the OLCI 1020 nm band for a turbid estuary. *Remote Sensing of Environment*, *120*, 133-144.

Kou, L., Labrie, D., & Chylek, P. (1993). Refractive indices of water and ice in the 0.65-to 2.5-µm spectral range. *Applied optics*, *32*(19), 3531-3540.

Kratzer, S., Brockmann, C., & Moore, G. (2008). Using MERIS full resolution data to monitor coastal waters—A case study from Himmerfjärden, a fjord-like bay in the northwestern Baltic Sea. *Remote Sensing of Environment*, *112*(5), 2284-2300.

Kratzer, S., Håkansson, B., & Sahlin, C. (2003). Assessing Secchi and photic zone depth in the Baltic Sea from satellite data. *AMBIO: A Journal of the Human Environment*, *32*(8), 577-585.

Kutser, T., Vahtmäe, E., Paavel, B., & Kauer, T. (2013). Removing glint effects from field radiometry data measured in optically complex coastal and inland waters. *Remote Sensing of Environment*, *133*, 85-89.

Le, C. F., Li, Y. M., Zha, Y., Sun, D., & Yin, B. (2009). Validation of a quasi-analytical algorithm for highly turbid eutrophic water of Meiliang Bay in Taihu Lake, China. *IEEE Transactions on Geoscience and Remote Sensing*, *47*(8), 2492-2500.

Lee, Z. P., Du, K. P., & Arnone, R. (2005). A model for the diffuse attenuation coefficient of downwelling irradiance. *Journal of Geophysical Research: Oceans*, *110*(C2).

Lee, Z., Ahn, Y. H., Mobley, C., & Arnone, R. (2010). Removal of surface-reflected light for the measurement of remote-sensing reflectance from an above-surface platform. *Optics Express*, *18*(25), 26313-26324.

Lee, Z., Carder, K. L., & Arnone, R. A. (2002). Deriving inherent optical properties from water color: a multiband quasi-analytical algorithm for optically deep waters. *Applied optics*, *41*(27), 5755-5772.

Lee, Z., Carder, K. L., Hawes, S. K., Steward, R. G., Peacock, T. G., & Davis, C. O. (1994). Model for the interpretation of hyperspectral remote-sensing reflectance. *Applied Optics*, *33*(24), 5721-5732.

Lee, Z., Carder, K. L., Mobley, C. D., Steward, R. G., & Patch, J. S. (1998). Hyperspectral remote sensing for shallow waters. I. A semianalytical model. *Applied optics*, *37*(27), 6329-6338.

Lee, Z., Carder, K. L., Mobley, C. D., Steward, R. G., & Patch, J. S. (1999). Hyperspectral remote sensing for shallow waters: 2. Deriving bottom depths and water properties by optimization. *Applied optics*, *38*(18), 3831-3843.

Lee, Z., Hu, C., Shang, S., Du, K., Lewis, M., Arnone, R., & Brewin, R. (2013). Penetration of UV-visible solar radiation in the global oceans: Insights from ocean color remote sensing. *Journal of Geophysical Research: Oceans*, *118*(9), 4241-4255.

Lee, Z., Shang, S., Du, K., & Wei, J. (2018). Resolving the long‐standing puzzles about the observed Secchi depth relationships. *Limnology and Oceanography*, *63*(6), 2321-2336.

Lee, Z., Shang, S., Hu, C., Du, K., Weidemann, A., Hou, W., & Lin, G. (2015a). Secchi disk depth: A new theory and mechanistic model for underwater visibility. *Remote sensing of environment*, *169*, 139-149.

Lee, Z., Wei, J., Voss, K., Lewis, M., Bricaud, A., & Huot, Y. (2015b). Hyperspectral absorption coefficient of “pure” seawater in the range of 350–550 nm inverted from remote sensing reflectance. *Applied Optics*, *54*(3), 546-558.

Luis, K. M., Rheuban, J. E., Kavanaugh, M. T., Glover, D. M., Wei, J., Lee, Z., & Doney, S. C. (2019). Capturing coastal water clarity variability with Landsat 8. *Marine Pollution Bulletin*, *145*, 96-104.

Maritorena, S., Morel, A., & Gentili, B. (1994). Diffuse reflectance of oceanic shallow waters: Influence of water depth and bottom albedo. *Limnology and oceanography*, *39*(7), 1689-1703.

Matsushita, B., Yang, W., Jaelani, L. M., Setiawan, F., & Fukushima, T. (2016). Monitoring Water Quality with Remote Sensing Image Data. Remote Sensing for Sustainability; CRC Press: Boca Raton, FL, USA, 163-189.

Matsushita, B., Yang, W., Yu, G., Oyama, Y., Yoshimura, K., & Fukushima, T. (2015). A hybrid algorithm for estimating the chlorophyll-a concentration across different trophic states in Asian inland waters. *ISPRS journal of photogrammetry and remote sensing*, *102*, 28-37.

Mishra, S., Mishra, D. R., & Lee, Z. (2014). Bio-optical inversion in highly turbid and cyanobacteria-dominated waters. *IEEE Transactions on Geoscience and Remote Sensing*, *52*(1), 375-388.

Mitchell, B. G., Kahru, M., Wieland, J., Stramska, M., & Mueller, J. L. (2002). Determination of spectral absorption coefficients of particles, dissolved material and phytoplankton for discrete water samples. *Ocean optics protocols for satellite ocean color sensor validation, Revision*, *3*(2), 231.

Mobley, C. D. (1994). Light and water: radiative transfer in natural waters. Academic press.

Mobley, C. D. (1999). Estimation of the remote-sensing reflectance from above-surface measurements. *Applied optics*, *38*(36), 7442-7455.

Moore, T. S., Dowell, M. D., Bradt, S., & Verdu, A. R. (2014). An optical water type framework for selecting and blending retrievals from bio-optical algorithms in lakes and coastal waters. *Remote sensing of environment*, *143*, 97-111.

Morel, A. (1974). Optical properties of pure water and pure sea water. *Optical aspects of oceanography*, *1*, 22.

National Institute for Environmental Studies (2016) Lake Kasumigaura Database, National Institute for Environmental Studies, Japan. Accessed via http://db.cger.nies.go.jp/gem/monie/inter/GEMS/database/kasumi/index.html on 29-05-2018.

Nechad, B., Ruddick, K. G., & Park, Y. (2010). Calibration and validation of a generic multisensor algorithm for mapping of total suspended matter in turbid waters. *Remote Sensing of Environment*, *114*(4), 854-866.

Olmanson, L. G., Bauer, M. E., & Brezonik, P. L. (2008). A 20-year Landsat water clarity census of Minnesota's 10,000 lakes. *Remote Sensing of Environment*, *112*(11), 4086-4097.

Olmanson, L. G., Brezonik, P. L., Finlay, J. C., & Bauer, M. E. (2016). Comparison of Landsat 8 and Landsat 7 for regional measurements of CDOM and water clarity in lakes. *Remote Sensing of Environment*, *185*, 119-128.

Philpot, W. D. (1989). Bathymetric mapping with passive multispectral imagery. *Applied optics*, *28*(8), 1569-1578.

Pope, R. M., & Fry, E. S. (1997). Absorption spectrum (380–700 nm) of pure water. II. Integrating cavity measurements. *Applied optics*, *36*(33), 8710-8723.

Preisendorfer, R. W. (1986). Secchi disk science: Visual optics of natural waters. *Limnology and oceanography*, *31*(5), 909-926.

Qiu, Z. (2013). A simple optical model to estimate suspended particulate matter in Yellow River Estuary. *Optics Express*, *21*(23), 27891-27904.

Rodrigues, T., Alcântara, E., Watanabe, F., & Imai, N. (2017). Retrieval of Secchi disk depth from a reservoir using a semi-analytical scheme. *Remote Sensing of Environment*, *198*, 213-228.

Ruddick, K. G., De Cauwer, V., Park, Y. J., & Moore, G. (2006). Seaborne measurements of near infrared water-leaving reflectance: The similarity spectrum for turbid waters. *Limnology and Oceanography*, *51*(2), 1167-1179.

Ruddick, K. G., Ovidio, F., & Rijkeboer, M. (2000). Atmospheric correction of SeaWiFS imagery for turbid coastal and inland waters. *Applied optics*, *39*(6), 897-912.

Ruddick, K., De Cauwer, V., & Van Mol, B. (2005). Use of the near infrared similarity reflectance spectrum for the quality control of remote sensing data. Remote Sensing of the Coastal Oceanic Environment. International Society for Optics and Photonics.

Secchi, P. A. (1864). Relazione delle esperienze fatte a bordo della pontificia pirocorvetta Imacolata Concezione per determinare la trasparenza del mare. *Memoria del PA Secchi. Il Nuovo Cimento Giornale de Fisica, Chimica e Storia Naturale, Ottobre 1864*, Published 1865, 20, 205-237.

Setiawan, F., Matsushita, B., Hamzah, R., Jiang, D., & Fukushima, T. (2019). Long-term change of the Secchi disk depth in Lake Maninjau, Indonesia shown by Landsat TM and ETM+ data. *Remote Sensing*, *11*(23), 2875.

Shang, S., Lee, Z., Shi, L., Lin, G., Wei, G., & Li, X. (2016). Changes in water clarity of the Bohai Sea: Observations from MODIS. *Remote Sensing of Environment*, *186*, 22-31.

Song, K., Li, L., Tedesco, L. P., Li, S., Clercin, N. A., Hall, B. E., ... & Shi, K. (2012). Hyperspectral determination of eutrophication for a water supply source via genetic algorithm-partial least squares (GA-PLS) modeling. *Science of the Total Environment*, *426*, 220-232.

Spyrakos, E., O'Donnell, R., Hunter, P. D., Miller, C., Scott, M., Simis, S. G., ... & Bresciani, M. (2018). Optical types of inland and coastal waters. *Limnology and Oceanography*, *63*(2), 846-870.

Stock, A. (2015). Satellite mapping of Baltic Sea Secchi depth with multiple regression models. *International Journal of Applied Earth Observation and Geoinformation*, *40*, 55-64.

Tsunogai, U., Daita, S., Komatsu, D. D., Nakagawa, F., & Tanaka, A. (2011). Quantifying nitrate dynamics in an oligotrophic lake using Δ^{17}O. *Biogeosciences*, *8*(3), 687-702.

Tyler, J. E. (1968). The secchi disc. *Limnology and oceanography*, *13*(1), 1-6.

Vahtmäe, E., Kutser, T., Martin, G., & Kotta, J. (2006). Feasibility of hyperspectral remote sensing for mapping benthic macroalgal cover in turbid coastal waters—a Baltic Sea case study. *Remote Sensing of Environment*, *101*(3), 342-351.

Wang, M., & Shi, W. (2007). The NIR-SWIR combined atmospheric correction approach for MODIS ocean color data processing. *Optics Express*, *15*(24), 15722-15733.

Wang, M., Son, S., & Shi, W. (2009). Evaluation of MODIS SWIR and NIR-SWIR atmospheric correction algorithms using SeaBASS data. *Remote Sensing of Environment*, *113*(3), 635-644.

Wang, Y., Shen, F., Sokoletsky, L., & Sun, X. (2017). Validation and Calibration of QAA Algorithm for CDOM Absorption Retrieval in the Changjiang (Yangtze) Estuarine and Coastal Waters. *Remote Sensing*, *9*(11), 1192.

Watanabe, F., Mishra, D. R., Astuti, I., Rodrigues, T., Alcântara, E., Imai, N. N., & Barbosa, C. (2016). Parametrization and calibration of a quasi-analytical algorithm for tropical eutrophic waters. *ISPRS Journal of Photogrammetry and Remote Sensing*, *121*, 28-47.

Wei, J., Lee, Z., & Shang, S. (2016). A system to measure the data quality of spectral remote-sensing reflectance of aquatic environments. *Journal of Geophysical Research: Oceans*, *121*(11), 8189-8207.

Wernand, M. R. (2010). On the history of the Secchi disc. *Journal of the European Optical Society-Rapid publications*, 5.

Yang, W., Matsushita, B., Chen, J., & Fukushima, T. (2011). Estimating constituent concentrations in case II waters from MERIS satellite data by semi-analytical model optimizing and look-up tables. *Remote sensing of environment*, *115*(5), 1247-1259.

Yang, W., Matsushita, B., Chen, J., Yoshimura, K., & Fukushima, T. (2013). Retrieval of inherent optical properties for turbid inland waters from remote-sensing reflectance. *IEEE Transactions on Geoscience and Remote Sensing*, *51*(6), 3761-3773.

Yang, W., Matsushita, B., Chen, J., Yoshimura, K., & Fukushima, T. (2014). Application of a semianalytical algorithm to remotely estimate diffuse attenuation coefficient in turbid inland waters. *IEEE Geoscience and Remote Sensing Letters*, *11*(6), 1046-1050.

Yang, W., Matsushita, B., Yoshimura, K., Chen, J., & Fukushima, T. (2015). A Modified Semianalytical Algorithm for Remotely Estimating Euphotic Zone Depth in Turbid Inland Waters. *IEEE Journal of Selected Topics in Applied Earth Observations and Remote Sensing*, *8*(4), 1545-1554.

Yarger H.L. & McCauley J.R. (1975) Quantitative water quality with Landsat and Skylab. In Proc., *NASA Earth Resources Survey Symposium, Houston*, pp.347–369.

Zhang, M., Tang, J., Dong, Q., Song, Q., & Ding, J. (2010). Retrieval of total suspended matter concentration in the Yellow and East China Seas from MODIS imagery. *Remote Sensing of Environment*, *114*(2), 392-403.

Zhang, X., Hu, L., & He, M. X. (2009). Scattering by pure seawater: effect of salinity. *Optics Express*, *17*(7), 5698-5710.

Zhao, D., Cai, Y., Jiang, H., Xu, D., Zhang, W., & An, S. (2011). Estimation of water clarity in Taihu Lake and surrounding rivers using Landsat imagery. *Advances in Water Resources*, *34*(2), 165-173.

Zibordi, G., Holben, B., Hooker, S. B., Mélin, F., Berthon, J. F., Slutsker, I., ... & Schuster, G. (2006). A network for standardized ocean color validation measurements. *Eos*, *Transactions American Geophysical Union*, *87*(30), 293-297.

Zibordi, G., Ruddick, K., Ansko, I., Moore, G., Kratzer, S., Icely, J., & Reinart, A. (2012). In situ determination of the remote sensing reflectance: an inter-comparison. *Ocean Science*, *8*(4), 567-586.